On Transonic Wing Shock Unsteadiness

Thesis submitted in accordance with the requirements of
the University of Liverpool for the degree of Doctor in Philosophy
by

Luke Masini (B.Eng (Hons)(Melit.), MSc (Cranfield))

April 2021

Abstract

Aircraft wings in high-speed flight experience detrimental flow unsteadiness. Its interaction with the flexible wing structure and resulting dynamic loads are addressed in the certification specifications which stipulate a cruise design point free from any structural vibration and buffeting. One such flow unsteadiness is shock buffet and its inherent dynamics near the onset of unsteadiness are addressed herein. Specifically, an extensive experimental dataset of a large aircraft wing geometry and complementary scale-resolving simulations are scrutinised. Whilst the experimental dataset comprises a wide range of flow conditions from pre-onset to established buffet for Mach numbers between 0.70 and 0.84 and four configurations, the primary focus is on the clean wing at the design Mach number of 0.80 and Reynolds number of approximately 3.6×10^6 (based on mean aerodynamic chord). Key to this study are highly-resolved unsteady surface pressure data acquired by dynamic pressure-sensitive paint, in addition to conventional data from pressure transducers and a wing-root strain gauge. To match the experiment and thereby aiding a richer elucidation of the flow physics, detached-eddy simulations are performed using two subgrid length-scale definitions, motivated by the challenge of simulating separating and reattaching shallow shear layers. Modal decomposition techniques are instrumental in pursuing a thorough data analysis. Experimentally, two distinct phenomena in shock-buffet conditions are identified. First, low-frequency shock unsteadiness with characteristic Strouhal numbers between 0.05 and 0.15 (where Strouhal number is based on mean aerodynamic chord and reference freestream velocity) propagates pressure disturbances predominantly inboard. Importantly, this coherent unsteadiness is exclusive to the experiment and even occurs before the strain gauge detects structural buffeting. Second, a broadband higher-frequency behaviour for Strouhal numbers between 0.2 and 0.5 is characterised by three-dimensional cellular patterns describing localised pockets of shear-layer pulsation synchronised with an outboard-propagating shock oscillation. Dominant modal features capturing this characteristic signature show striking similarity between experiment and simulation, detailing the pertinent attributes of shock-buffet unsteadiness whilst contrasting it with the first phenomenon. These findings will help clarify these edge-of-the-envelope flow phenomena and ultimately inform future wing design.

Dedication

To Maria
For her friendship, her patience, and her unconditional love.

And to my parents
Thank you for always being there.

Acknowledgements

I would like to express my sincere gratitude to anyone who directly or indirectly has supported me throughout this research.

I wish to acknowledge my supervisors Dr. Sebastian Timme and Dr. Andrew J. Peace who provided me with this research opportunity and continuously mentored me. Their guidance, ideas and knowledge were of utmost help to this work and are greatly appreciated. I particularly wish to thank Dr. Sebastian Timme for encouraging me to keep on pushing and strive for excellence.

I would like to take this opportunity to thank my Viva examiners Prof. Holger Babinsky and Prof. Robert Poole for their fruitful discussions, helpful comments and suggestions for improvement.

My sincere thanks go to all at the Aircraft Research Association Ltd for insightful discussions and for creating a stimulating working environment during my first year experience at their premises in Bedford. I would like to also thank all fellow PhD students and good friends at the University of Liverpool for the great experiences we shared during my two years and three months in Liverpool.

On a personal level, I would like to thank my wonderful parents, Victoria and Mario Victor, for raising me and supporting me. I am forever indebted to their hard work and sacrifice. Thank you for always believing in me.

A word of appreciation goes to my partner Maria, my two elder siblings, Samuel and Maria, and to all friends, near and far, for their support and patience throughout my personal life.

This research was jointly funded by the Aircraft Research Association Ltd and the University of Liverpool.

Declaration

I confirm that the thesis is my own work, that I have not presented anyone else's work as my own and that full and appropriate acknowledgement has been given where reference has been made to the work of others.

Luke Masini
April 2021

List of Publications

Peer-Reviewed Journal Articles

Masini, L., Timme, S. & Peace, A. J. 2020 Scale-resolving simulations of a civil aircraft wing transonic shock buffet experiment. *AIAA Journal* **58** (10), 4322–4338. https://doi.org/10.2514/1.J059219

Masini, L., Timme, S. & Peace, A. J. 2020 Analysis of a civil aircraft wing transonic shock buffet experiment. *Journal of Fluid Mechanics* **884** (A1), 1–42. https://doi.org/10.1017/jfm.2019.906

Conference Papers

Masini, L., Timme, S. & Peace, A. J. 2019 Reynolds number effects on wing shock buffet unsteadiness. In *AIAA Aviation 2019 Forum*. AIAA 2019-2820. https://doi.org/10.2514/6.2019-2820

Masini, L., Timme, S. & Peace, A. J. 2018 Scale-resolving simulation of shock buffet onset physics on a civil aircraft wing. In *Royal Aeronautical Society 2018 Applied Aerodynamics Conference*.

Masini, L., Timme, S., Ciarella A. & Peace, A. J. 2017 Influence of vane vortex generators on transonic wing buffet: Further analysis of the BUCOLIC experimental dataset. In *52nd 3AF International Conference on Applied Aerodynamics*. FP14-AERO2017-masini.

Table of Contents

List of Figures

List of Tables

List of Symbols

$a_{i,j}$	=	expansion coefficients at each time instant and spatial mode
A	=	linear mapping
b	=	reference semi-span
B	=	number of blocks for signal processing
c	=	local chord length
c_p	=	specific heat coefficient at constant pressure
c_v	=	specific heat coefficient at constant volume
C_B	=	buffeting coefficient
C''_B	=	corrected buffeting coefficient
C_L	=	lift coefficient
C_P	=	pressure coefficient
$C_{xy}(f)$	=	magnitude-squared coherence
d	=	minimum distance to a wall
$d_{i,j}$	=	scalar coefficients at each time instant and spatial mode
e	=	specific internal energy
E	=	expectation operator
E	=	total energy
f	=	frequency
f_{d}	=	delay function in delayed detached-eddy simulation
f_s	=	sampling frequency
f_{v1}	=	near-wall damping function in Spalart–Allmaras turbulence model
h	=	specific enthalpy
H	=	total enthalpy
i	=	time index
$\Im$	=	imaginary part
k	=	turbulent kinetic energy
K	=	overlapping samples
l	=	length scale
$\mathbf{l}$	=	set of cross-product points

M	=	observations in subsample
M	=	freestream Mach number
n	=	dimension of dataset or number of computational points
$\mathbf{n}_\omega$	=	unit vector aligned with the vorticity vector
N	=	samples
m	=	number of snapshots
P	=	freestream static pressure
P	=	power of the temporal window in a windowed periodogram
Pr	=	Prandtl number
q	=	freestream dynamic pressure
r	=	index used for truncation
$\mathbf{r}$	=	centre vector
$\Re$	=	real part
Re	=	Reynolds number
s	=	physical distance
$S_{i,j}$	=	strain-rate tensor
$S(f)$	=	power spectral density function
$\hat{S}_p(f)$	=	periodogram
$\hat{S}_w(f)$	=	windowed periodogram
$\hat{S}_W(f)$	=	power spectral density estimate using Welch method
$S_{xy}(f)$	=	cross-spectrum of signals $x(t)$ and $y(t)$
St	=	Strouhal number
T	=	freestream static temperature
t	=	physical time
$U_{i,j}$	=	velocity gradients
U_p	=	propagation speed
U_∞	=	freestream velocity
v_i	=	velocity component in Cartesian coordinate system
$v(t)$	=	temporal window
$V_\epsilon(t)$	=	strain-gauge signal
x	=	local chordwise coordinate
$\mathbf{x}$	=	data vector (snapshot)
$x(t)$	=	discrete-time signal
X	=	chordwise coordinate
$\mathbf{X}$	=	data matrix
y^+	=	wall-normal mesh spacing in wall units
Y	=	spanwise coordinate

Greek Symbols

α	=	angle of attack
α_b	=	buffet-onset angle of attack
β	=	spanwise wavenumber
γ	=	heat capacity ratio
δ_{ij}	=	Kronecker delta
Δ	=	subgrid length scale
Δ_0	=	mesh target spacing
$\Delta_{\max}$	=	maximum-edge subgrid length scale
Δ_{vol}	=	volume-based subgrid length scale
Δ_ω	=	vorticity-sensitive subgrid length scale
$\tilde{\Delta}_\omega$	=	vorticity-sensitive length scale that reduces to a maximum-edge formulation
η	=	non-dimensional spanwise position
κ	=	thermal conductivity coefficient
κ	=	von Kármán constant
λ	=	eigenvalue
Λ	=	sweep angle
$\boldsymbol{\Lambda}$	=	eigenvalue matrix
μ	=	freestream dynamic viscosity
μ	=	DMD eigenvalues
μ_t	=	eddy viscosity
ν	=	kinematic viscosity
$\hat{\nu}$	=	intermediate eddy viscosity
ϕ	=	phase angle
φ	=	arbitrary variable
$\boldsymbol{\varphi}$	=	spatial mode
$\boldsymbol{\Phi}$	=	spatial mode matrix
$\boldsymbol{\psi}$	=	eigenvectors
$\boldsymbol{\Psi}$	=	eigenvector matrix
ρ	=	freestream density
σ	=	standard deviation
σ	=	growth/decay rate
τ_{ij}	=	viscous stress tensor
ω	=	angular frequency

Subscripts

$c/4$	=	quarter chord
l	=	laminar
LE	=	leading edge
t	=	turbulent
TE	=	trailing edge

Acronyms

ARA	=	Aircraft Research Association Limited
BUCOLIC	=	Buffet Control of Transonic Wings
CAD	=	computer aided design
CFL	=	Courant-Friedrichs-Lewy
CSD	=	cross spectral density
DDAS	=	dynamic data acquisition system
DDES	=	delayed detached-eddy simulation
DES	=	detached-eddy simulation
DMD	=	dynamic mode decomposition
DPSP	=	dynamic pressure-sensitive paint
DLR	=	German Aerospace Center (Deutsches Zentrum für Luft- und Raumfahrt)
fps	=	frames-per-second
FS	=	full scale
K–H	=	Kelvin–Helmholtz
LD	=	low dissipation
LD2	=	low dissipation and low dispersion
LES	=	large-eddy simulation
MAC	=	mean aerodynamic chord
POD	=	proper orthogonal decomposition
PSD	=	power spectral density
PSP	=	pressure-sensitive paint
RANS	=	Reynolds-averaged Navier–Stokes
RMS	=	root mean square
S–A	=	Spalart–Allmaras
SWBLI	=	shock-wave/boundary-layer interaction
TWT	=	transonic wind tunnel
VG	=	vortex generator

Chapter 1

Introduction

This chapter reviews the state-of-the-art in transonic shock-buffet understanding. Shock buffet on both aerofoils and wings is introduced to set the picture for the work herein which focuses on the flow physics governing shock-buffet onset on swept wings.

1.1 Background

In the transonic flight regime, the flow over the suction side of aircraft wings accelerates to form an embedded supersonic region, which terminates with a shock wave as the flow compresses towards the trailing edge. The presence of a shock wave close to a surface results in a shock-wave/boundary-layer interaction (SWBLI) which is crucial in determining the performance of transonic aircraft. The strong adverse pressure gradient of the shock wave thickens the boundary layer, potentially causing flow separation. Inevitably, this causes drag penalties in the form of skin friction and pressure drag contributions depending on the strength of the shock wave. First, the state of the boundary layer affects the skin-friction drag contribution. Second, the shock wave introduces a stagnation pressure drop that reduces surface pressures over the rear of the wing, creating wave drag via a pressure drag contribution. Furthermore, separations also contribute to pressure drag as they alter the pressure distribution over the wing. Moreover, strong interactions may also lead to flow unsteadiness with severe adverse effects (Babinsky & Harvey, 2011). Such detrimental consequences increase rapidly with Mach number and thus pose a major constraint to transonic aircraft design.

Within a narrow set of transonic flight conditions beyond critical parameter combinations such as Mach number and angle of attack, SWBLI induces self-sustained shock oscillation and intermittent boundary-layer separation, a phenomenon termed as *shock buffet*. This leads to unsteady aerodynamic loads and a consequent structural response, referred to as *buffeting*, mutually interacting with the flow. The net effect includes a drag penalty together with an associated increased environmental footprint, a deterioration of aircraft performance, handling qualities and structural fatigue life, and a

degradation of passenger comfort. Furthermore, certification requirements stipulate a cruise design point free from any structural vibration and buffeting, such that buffet onset may limit the flight envelope at high Mach number and load factor, depending on the wing design philosophy.

Despite over half a century of research, the underlying flow mechanisms governing the onset of transonic shock buffet on swept wings still present a key challenge for aerodynamicists with an unequivocal explanation yet to be proposed (Giannelis *et al.*, 2017). The complex nature of such edge-of-the-envelope flow physics combined with recent developments in wing design, such as high aspect-ratio and flexible wings, motivate continued scrutiny from both industry and academia. Extensive research on this aerodynamic instability has reported distinct characteristics on nominally two-dimensional aerofoils and swept three-dimensional wings. The primary focus herein is to elucidate the flow physics in the vicinity of buffet onset on a civil aircraft wing. This study combining state-of-the-art experimental data from an industrial transonic facility and numerical scale-resolving simulations fills a gap in swept-wing shock-buffet literature which mostly focuses on conditions well beyond onset.

1.2 Aerofoil Shock Buffet

The first photos reporting shock-wave movement were taken in 1944 but published three years later by Hilton & Fowler (1947). Along the years, several investigations concentrating on transonic shock buffet on aerofoils resulted in a number of classifications for its different aspects based for instance on the location where flow separation first occurs, the type of aerofoil, and the nature of the shock oscillation itself.

Comprehensive research by Pearcey (1961) and Pearcey *et al.* (1968) classified different forms of upper surface flow-separation mechanisms on transonic aerofoils based on where this first emanates. Their early work on conventional aerofoils in transonic conditions identified a bubble-type separation as the flow first separates underneath the shock but reattaches before reaching the trailing edge (Pearcey, 1955; Pearcey & Holder, 1962). Further work on thick or supercritical aerofoils found a distinct form of separation which starts near the trailing edge and spreads upstream. To distinguish between these types of flow separation, Pearcey *et al.* (1968) referred to the shock-induced bubble separation type as *Model A* and the second type also involving trailing-edge separation as *Model B*. This classification is illustrated in Fig. 1.1. Three variants of the latter were identified, depending on whether rear separation is already present, or if it is primarily provoked by the bubble or the shock, with complex interactions between the separation bubble and trailing-edge separation. Their work provided an early buffeting onset indication based on trailing-edge pressure divergence as recorded from steady-state wind-tunnel measurements, enabling the determination of a buffet boundary for aerofoils that are characterised by bubble-type separation (Pearcey & Holder, 1962).

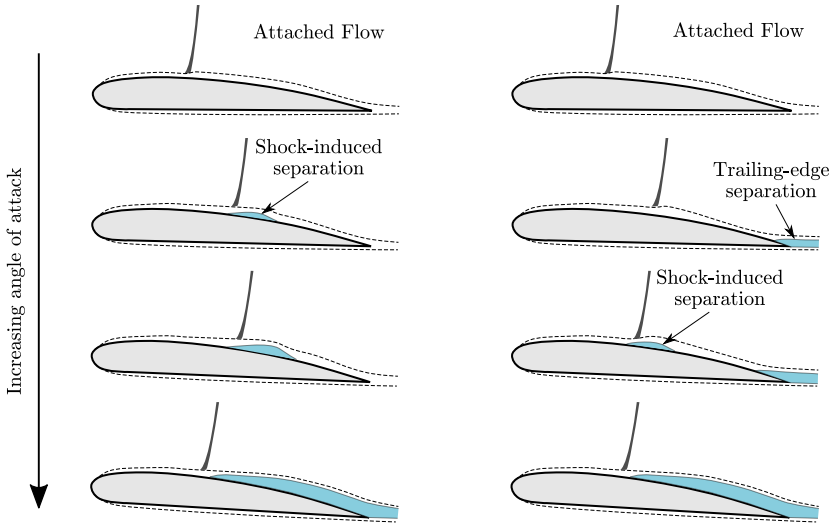

Figure 1.1: Flow separation types as classified by Pearcey *et al.* (1968); *Model A* (left) and *Model B* (right). Figure adapted from Pearcey *et al.* (1968) and Babinsky & Harvey (2011).

The seminal work by Tijdeman (1977) classified periodic shock motions on aerofoils into three main types, by studying the effect of trailing-edge flap deflections on a symmetric aerofoil. *Type A* shock motion was observed at the highest Mach number tested, whereby the shock is present throughout the buffet cycle and undergoes almost sinusoidal motion, with a phase shift relative to the flap deflection and the shock-wave motion, such that the shock wave reaches its maximum strength when it is moving upstream and is weakest during its downstream excursion. At a slightly decreased Mach number, *Type B* shock motion takes place, closely resembling *Type A* motion. However, in this case, the shock becomes very weak during a portion of the cycle and degenerates into a series of pressure waves when moving downstream. Tijdeman (1977) stated that *Type-B* separation is very sensitive to the Reynolds number and the location where laminar-to-turbulent transition occurs. *Type C* shock motion differs completely. This results when the shock wave moves upstream and initially increases in strength. It then weakens, but continues to move upstream, eventually leaving the aerofoil from the leading edge and propagates upstream as a free shock wave. This sequence repeats periodically and alternates between the upper and lower surfaces.

In the case of biconvex aerofoils at zero degree angle of attack, shock oscillations take place on both the pressure and suction surfaces in what is termed as *Type I* shock buffet. This requires the shock to be strong enough to induce fully separated flow; hence, the local Mach number just ahead of the shock is a reliable buffet onset indicator (Mabey, 1981; Mabey *et al.*, 1981). In contrast, a reconciled viewpoint on the causes of *Type II* shock buffet, involving shock oscillation on supercritical aerofoils, is yet to be proposed. The interested reader is referred to the reviews by Lee (2001), detailing early work in the field of aerofoil shock buffet, and Giannelis *et al.* (2017), focusing on *Type II* buffet and highlighting more recent studies.

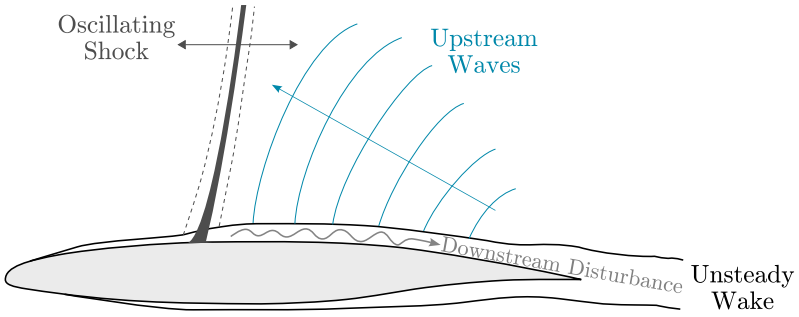

Figure 1.2: Model for self-sustained shock oscillation on aerofoils (adapted from Lee (1990)).

The following paragraphs provide the reader with insight on aerofoil shock-buffet dynamics to understand the main differences with those on transport-type wings, which are the main focus of the work herein.

In the turbulent transonic flow regime, periodic shock oscillations with low frequencies (well below the energetic scales of the incoming boundary layer) and large shock excursions (around 20% of the chord length) have been reported in several experimental and numerical studies (see for example McDevitt & Okuno (1985), Deck (2005) and Jacquin *et al.* (2009)). The first and arguably most popular model to describe shock buffet on aerofoils was proposed by Lee (1990) and is depicted in Fig. 1.2. This model can predict the periodic shock oscillation frequency as a result of an acoustic feedback loop. It is assumed that disturbances emanating from the shock-induced separation point travel downstream through the separated shear layer. Upon reaching the trailing edge, acoustic waves (sometimes called Kutta waves) are generated and travel upstream through the subsonic region above the separated flow, ultimately interacting with the shock. This completes the feedback loop which sustains the shock oscillation.

Following this work, several experiments of increasing complexity and instrumentation have described low-frequency shock oscillations, typically at Strouhal numbers (based on chord length) between 0.06 and 0.08 (Feldhusen-Hoffmann *et al.*, 2018). The hypotheses that the oscillating shock is affected by external acoustic forcing and that the shock directly influences conditions at the trailing edge have been confirmed experimentally supporting Lee's model (Hartmann *et al.*, 2012, 2013*a*; Feldhusen-Hoffmann *et al.*, 2018). However, efforts to directly measure or simulate the propagation of upstream and downstream travelling waves and disturbances have led to contradictory results such that the propagation path of the acoustic waves remains debated (Hartmann *et al.*, 2013*b*; Jacquin *et al.*, 2009). For instance, the experimental studies by Hartmann *et al.* (2012) and Feldhusen-Hoffmann *et al.* (2018) together with the numerical studies by Deck (2005) and Xiao *et al.* (2006) report good agreement between their buffet frequency and that predicted by Lee's model. However, considerable discrepancies were reported by Jacquin *et al.* (2009) and Garnier & Deck (2010) with the former suggesting a modified wave propagation feedback model, whereby the upstream propagating acoustic waves can travel both along the upper and lower surfaces. Such

discrepancies indicate that Lee's model might not be applicable in all situations, as contemplated by Giannelis *et al.* (2017).

A more recent explanation to aerofoil shock buffet by Crouch *et al.* (2007, 2009) is rooted within stability theory and describes shock buffet as a Hopf bifurcation with a globally unstable mode of the flow appearing beyond critical conditions. This numerical study resulted in good agreement with the experimental observations by McDevitt & Okuno (1985) in terms of the shock-oscillation frequency and the buffet onset angle of attack. Further work by Sartor *et al.* (2014) on a different aerofoil supports this link between aerofoil shock buffet and a global flow instability. The spatial structure of the globally unstable mode depicts the shock wave as the dominating flow feature but also shows a contribution within the downstream shear layer, such that buffet is described as a pulsating recirculating bubble synchronised with the shock displacement. Even though published work has described Crouch's description to be conflicting with Lee's model (Giannelis *et al.*, 2017), both authors are describing the same phenomenon using different approaches. However, it should be highlighted that the qualitative description of the shock-buffet dynamics is somewhat different. For instance, Crouch *et al.* (2009) describes the pressure perturbation to originate near the base of the shock. This disturbance moves upward along the shock wave and is ingested into the sonic region after reaching the top of this zone. This is accompanied by an aft movement of the shock which intensifies the perturbation as it approaches the trailing edge. This pressure wave also goes around the trailing edge, moves upstream along the pressure side and is ingested into the sonic zone as it reaches the leading edge. In the case of the model described by Lee (1990), the pressure wave generated at the shock is assumed to only propagate downstream inside the boundary layer as explained above.

Several numerical techniques have been employed to simulate two-dimensional shock buffet, including unsteady Reynolds-averaged Navier–Stokes (RANS) simulations (Brunet, 2003; Xiao *et al.*, 2006; Iovnovich & Raveh, 2012), detached-eddy simulations (DES), including the zonal (Deck, 2005) and the delayed (DDES) approach (Grossi *et al.*, 2014), and large-eddy simulations (LES) (Garnier & Deck, 2010; Fukushima & Kawai, 2017). Most of these studies consider a fully turbulent boundary layer upstream of the SWBLI. However, noticeable differences have recently been reported under laminar flow conditions, where laminar-to-turbulent transition takes place in the region of the SWBLI. In this case, the shock excursions are confined to the shock foot over smaller chordwise distances and at frequencies of over an order of magnitude higher than the fully turbulent case (Brion *et al.*, 2017; Dandois *et al.*, 2018). Furthermore, complex interactions between the shock wave, pressure waves and the boundary layer have been studied using direct numerical simulation at moderate Reynolds numbers of up to 800 000 by Zauner *et al.* (2019). In this case, the flow features were observed to take place at frequencies distinct from characteristic low-frequency lift fluctuations, with the latter occurring at a Strouhal number of approximately 0.1.

1.3 Finite Wing Shock Buffet

The difficulty in elucidating the flow physics governing transonic wing shock buffet is further compounded by three-dimensional interactions and complex geometries. Even though a number of research organisations have invested substantial resources in studying this topic, literature on swept-wing buffet remains limited, calling for synergistic experimental and numerical efforts. Early studies employing wind tunnel and flight tests (Hwang & Pi, 1975; Riddle, 1975; Roos, 1985) have shown a general agreement that wing buffet differs from aerofoil buffet in two main aspects. First, a narrow frequency peak no longer characterises the phenomenon. Instead, the shock oscillations are non-periodic with a broadband higher-frequency signature at Strouhal numbers between 0.2 and 0.6, based on mean aerodynamic chord (MAC) and reference freestream velocity. Second, shock oscillation takes place over shorter chordwise distances which can vary along the span depending on the extent of the separation region downstream of the shock. Benoit & Legrain (1987) highlighted how unsteady flow causes narrow-band fluctuations on aerofoils and unswept wings but do not apply to swept, transport-type wings. Instead, swept wings exhibit broadband fluctuations whilst the evolution of the separation region with angle of attack differs in terms of spanwise extent.

More recent experimental tests (Dandois, 2016; Koike *et al.*, 2016; Lawson *et al.*, 2016) employing highly-instrumented wind-tunnel models have confirmed the broadband signature and have further elucidated the phenomenon by computing characteristic propagation speeds. The advent of novel optical techniques such as dynamic pressure-sensitive paint (DPSP), essentially a fast-response pressure-sensitive paint coupled with high-frame-rate image capturing, has greatly progressed the understanding of the complex shock motion that takes place at shock-buffet conditions. Such data are critical to complement numerical work of ever-increasing fidelity, motivated by renewed interest in edge-of-the-envelope aerodynamics. The interested reader is referred to the review on PSP by Gregory *et al.* (2014). Early applications in transonic wind tunnels (Steimle *et al.*, 2012; Merienne *et al.*, 2013) had poor resolution and restricted coverage, limited by the paint composition, its application, and camera technology. Having demonstrated the potential to clarify the flow mechanisms of complex flows, this rapidly evolving technique attracted attention, with recent experiments successfully acquiring unsteady pressure over the entire wing surface (Lawson *et al.*, 2016; Sugioka *et al.*, 2018). In effect, rather than being confined to the discrete locations of pressure transducers, analysis is enabled over a much wider area, giving critical insight. Notably, the experimental test by Lawson *et al.* (2016) simultaneously measured unsteady pressure using DPSP and unsteady transducers together with structural response data at a wide range of flow conditions. For their so-called RBC12 half model, increased pressure fluctuations due to separated flow within a low-frequency range of $0.05 \leq St \leq 0.15$, where St is the Strouhal number based on mean aerodynamic chord,

coincide with the structural buffeting incidence defined by the direct measurement of the structural response using strain gauges and accelerometers. As the incidence is further increased penetrating into the light buffeting regime (see ESDU (1987)), the unsteady shock oscillation over larger chordwise extents at outboard stations a broader frequency range ($0.08 \leq St \leq 0.5$) becomes the main cause of structural buffeting.

1.4 Shock Unsteadiness and Swept-Wing Shock Buffet

Under the broad definition of SWBLI (see for example the reviews by Clemens & Narayanaswamy (2014) and Gaitonde (2015)), both frequency ranges for the shock oscillations observed by Lawson *et al.* (2016) would be categorised as manifestations of low-frequency shock unsteadiness, having frequencies of at least two orders of magnitude lower than those associated with wall-bounded turbulence. Even in the case of supersonic flows which comprise most of the SWBLI literature, the causality of the mechanisms driving the low-frequency shock motions remains controversial and debated. Swept-wing shock buffet research has primarily focused on the characteristic broadband outboard-running fluctuations. However, a thorough review of the literature also reveals a different phenomenon having an inboard-running behaviour at lower frequency. Evidence concerning this lower-frequency shock unsteadiness is almost exclusive to wind-tunnel tests, although a recent global stability analysis on an infinite-span swept wing has reported such behaviour for the long-wavelength mode(Crouch *et al.*, 2019). Close examination of the results by Dandois (2016) show that the highest signal coherence in a spanwise sense was obtained in the low-frequency range ($0.04 \leq St \leq 0.08$), whereby pressure fluctuations propagate inboard. This is analogous to the observation in Lawson *et al.* (2016) albeit on different wing models investigated in different wind tunnels. Noting that the shock is affected by upstream- and/or downstream-running perturbations (Sartor *et al.*, 2015) which might naturally be present in a wind-tunnel environment, such observations raise questions on the origin of this shock unsteadiness and its relation to the reportedly pure aerodynamic shock-buffet instability. In this regard, closed-circuit transonic wind tunnels exhibit upstream-propagating acoustic noise (Haxter *et al.*, 2017), whilst a receptivity analysis of an aerofoil in shock-buffet conditions revealed that such flow is receptive to disturbances propagating downstream, with the shock acting as a low-pass filter of the external forcing (Sartor *et al.*, 2014). In addition to the influence of boundary layer fluctuations and external disturbances, the wing's structural dynamics may also contribute to the shock unsteadiness. Under such high-loading conditions, a flexible wing encounters both static deformation and dynamic fluid-structure interaction in response to aerodynamic and external loading. In their numerical linearised-aerodynamics analysis, Timme & Thormann (2016) showed how forced wing vibration excites both a low-frequency response, dominated by the shock unsteadiness, and distinct higher-frequency peaks at typical swept-wing buffet

frequencies. Whilst the latter is greatly amplified around the critical flow condition, the lower-frequency shock unsteadiness has lower sensitivity, highlighting coexisting phenomena. Closer examination of the data showed that inboard propagation takes place at low frequencies on the RBC12, and the higher-frequency behaviour is found on different generations of civil aircraft wings (Belesiotis-Kataras & Timme, 2018).

Shifting the focus to the broadband-frequency signature typically reported in swept-wing shock-buffet studies, recent experimental work in several transonic wind tunnels (Dandois, 2016; Lawson *et al.*, 2016; Koike *et al.*, 2016) employing models equipped with dedicated instrumentation have confirmed characteristic bumps in the wall-pressure spectra, typically in a Strouhal number range between 0.2 and 0.6. A cross-spectral analysis of the unsteady transducer data reveals outboard-running spanwise propagations at this frequency bump, when considering conditions beyond buffet onset. On the numerical front, systematic work by Iovnovich & Raveh (2015) employing time-marching unsteady RANS simulations, revealed contrasting characteristics between straight/low-sweep-angle wings and those with sweep angles above 20°. At low sweep angles, shock oscillation is chordwise dominated and similar to that on aerofoils. On moderately and highly swept wings, pressure propagates along the shock in a spanwise direction towards the wing tip, showing a monotonic frequency increase with sweep angle for the shock oscillations. Pockets of downstream shock-induced separation, coined therein as buffet cells, synchronised with the outboard-travelling shock excursion, were also observed. A related numerical study on infinite swept wings has shown similar characteristics for buffet cells, linked with transonic shock buffet, and low-speed stall cells (Plante *et al.*, 2020).

Moreover, studies employing biglobal stability analysis on such infinite wings have identified, besides the typical aerofoil mode, monotone stationary spanwise-periodic modes on straight wings, which, with the introduction of sweep, become oscillatory with outboard propagation (Crouch *et al.*, 2019; Plante *et al.*, 2019; Paladini *et al.*, 2019). The term biglobal refers to a stability analysis in three-dimensional space with two inhomogeneous dimensions, with the third homogeneous direction treated as periodic (Theofilis, 2011). Increasingly sophisticated simulations, including scale-resolving DES (Brunet & Deck, 2008; Sartor & Timme, 2017; Ishida *et al.*, 2017), have been conducted on several geometries demonstrating the capability of capturing complex shock motion and characteristic spanwise propagation of buffet cells. Even though the time scales of shock buffet are much longer than those related to wall-bounded turbulence, hence justifying unsteady RANS simulations, scale-resolving simulations have explained the phenomenon in more detail and with a broader spectral content. The propagation of buffet cells has also been identified from a modal analysis of zonal DES data (Ohmichi *et al.*, 2018). The flow conditions simulated in those finite-wing studies are well beyond the point when flow unsteadiness is first observed and do not necessarily describe the flow physics in the vicinity of onset. In this spirit, the involve-

ment of a global instability in the onset dynamics has recently been reported from a triglobal stability analysis (global mode computation with three inhomogeneous spatial dimensions) on a finite wing (Timme, 2020). Therein, buffet cells are linked to an unstable eigenmode while the emergence of a group of modes with reduced decay rate agrees with the aforementioned broadband frequency trend. The same trigobal analysis methodology was employed by He & Timme (2020*b*) on infinite wings reproducing the continuous band of spanwise modes in the medium-wavelength range identified from biglobal stability studies (Crouch *et al.*, 2019; Plante *et al.*, 2019; Paladini *et al.*, 2019) discretely. Furthermore, the spanwise-periodic modes on infinite wings obtained from those studies were also reported from a recent resolvent analysis (He & Timme, 2020*a*).

1.5 Aim and Objectives of Work and Thesis Outline

The aim of this work is to present a synergistic study that further elucidates the flow physics governing shock-buffet onset on swept wings. While the limited literature on swept wing shock buffet tends to focus on cases well beyond onset, this work aims to fill this gap by presenting complementary analyses based on high-quality experimental and numerical data focusing on the inherent dynamics in the vicinity of shock-buffet onset. The work makes a contribution to the wider ambition in the community to clarify this important phenomenon in edge-of-the-envelope aerodynamics and to help inform future wing design.

This thesis addresses three principal objectives to fulfil the aforementioned aim. First, the extensive experimental database introduced by Lawson *et al.* (2016) is analysed to a much greater depth than has previously been performed, focusing on the unsteady flow physics that coincide with the onset of the structural buffeting response on a civil aircraft wing for a range of Mach numbers. Second, scale-resolving simulations are performed in the vicinity where flow unsteadiness is first observed, which poses a challenge in simulating separating and reattaching shallow shear layers. Third, suitable data-processing methods should be employed to qualitatively and quantitatively assess and compare these massive datasets. Data-based modal identification techniques, actively explored in the global fluid mechanics community, are used to enable the direct comparison between experimental and numerical data based on salient modal features.

The theoretical foundations of the methods used to process the datasets in this thesis are outlined in Chapter 2. The conventional way to study unsteady datasets is to assess their frequency content. The two main approaches to estimate the power spectral density from a signal, namely, non-parametric and parametric methods are described. Furthermore, modal decomposition and analysis is used to post-process spatio-temporal data providing deeper insight. This chapter describes the two widely used techniques including proper orthogonal decomposition and dynamic mode decomposition.

The RBC12 civil aircraft test case used for the experimental and numerical analyses is described in Chapter 3. This provides a useful reference for the geometrical and structural data of the wind-tunnel model continuously scrutinised herein.

Chapter 4 details the results and analyses of the experiments conducted in the Aircraft Research Association Transonic Wind Tunnel. The experimental testing was extensive covering seven Mach numbers between 0.70 and 0.84 together with a wide range of angles of attack from pre-onset to well-beyond onset conditions for several configurations. This chapter first describes the experiment and data cleaning, including the instrumentation, configurations and test campaign whilst outlining the flow corrections applied. The shock-buffet onset indicators are then reviewed to define the buffet-onset angle of attack at all Mach numbers tested. The analysis starts with conventional data analysis methods to set the picture for the type of flow separation and unsteadiness on this wing. Subsequently, modal analysis of the dynamic pressure-sensitive paint data gives further clarification of the flow phenomena both before the onset of structural buffeting and around onset. The analysis is primarily focused on the clean wing at the design Mach number of 0.80. Additionally, the influence of passive flow control using vortex generators and the effect of Mach number are also presented.

Chapter 5 complements the previous analysis by presenting scale-resolving simulations in the vicinity of buffet onset using the delayed DES approach. The flow models and numerics are first described including the governing Navier–Stokes equations, Favre- and Reynolds- averaging, and turbulence modelling. The flow solver and the numerical setup are then detailed. As in the experimental chapter, the simulations are assessed using both conventional and modal analysis methods. The primary focus is to reproduce the experimental flow field to gain more insight into the governing flow physics. In this regard, two simulations are performed to study the inherent buffet-onset dynamics at model scale whilst investigating the impact of the subgrid length scale and the transition from modelled to resolved turbulence, an important aspect in the numerical simulation of separated shallow shear layers. In addition, a third simulation at flight scale is conducted and analysed in order to assess the influence of Reynolds number on shock-buffet onset. The model-scale numerical datasets are validated against the clean wing experimental data from steady and unsteady pressure transducers, balance data, and dynamic pressure-sensitive paint data using pressure distributions, integrated coefficients and spectral analysis. Moreover, the dominant flow phenomena are directly compared based on salient modal features from both proper orthogonal decomposition and dynamic mode decomposition.

The results obtained experimentally and numerically are discussed in detail in Chapter 6. The analysis conducted herein is scrutinised within the context of a broader research effort and viewed alongside the published state-of-the-art. This chapter reconciles the pertinent characteristics, including propagation speeds and wavelength data

of the key flow phenomena around shock-buffet onset conditions identified herein. Furthermore, the possible causes and drivers thereof are contemplated.

Chapter 7 draws conclusions from the study conducted herein. The main findings and key messages are emphasised whilst providing suggestions for future work.

Chapter 2

Data Processing Methodology

The transonic flow at shock-buffet conditions exhibits complex behaviour and constitutes unsteady flow structures with various spatial and temporal scales. Insight into the state of the flow can be inferred from pressure distributions. With regards to unsteady signals, the conventional way to characterise their frequency signature is to compute their power spectral density data. This can be performed using non-parametric and parametric methods, the performance of which depends on the nature of the signal. This chapter details the theoretical background of such approaches, including the Welch method and the Burg method, which are used to analyse unsteady pressure signals at discrete locations. In addition to conventional analysis, more recent modal decomposition methods are outlined. This is motivated by the high-fidelity datasets generated by the experimental dynamic pressure-sensitive paint technique and numerical time-accurate simulations which can be challenging to post-process, due to both the sheer volume of data and the extraction of physically meaningful and interpretable outputs. In fact, modal decomposition and analysis has become widespread in the fluid dynamics community (Taira *et al.*, 2017). A simple visual inspection of the datasets herein reveals unsteady perturbations along and downstream of the shock. It can be anticipated that such flow features can be extracted through some mathematical procedure. In this spirit, this chapter describes two prominent modal decomposition techniques that identify and characterise important flow features from unsteady datasets. These techniques are often termed *data based* when flow-field data is taken as the input, with the resulting output having a spatial and temporal component aiding the elucidation of the flow physics. Two widely used data-based techniques are proper orthogonal decomposition (POD) and dynamic mode decomposition (DMD). These mathematical techniques decompose the dataset into a set of spatial features, typically called modes, accompanied by characteristic values, generally denoting the corresponding energy levels and frequencies and growth/decay rates, depending on the specific method used.

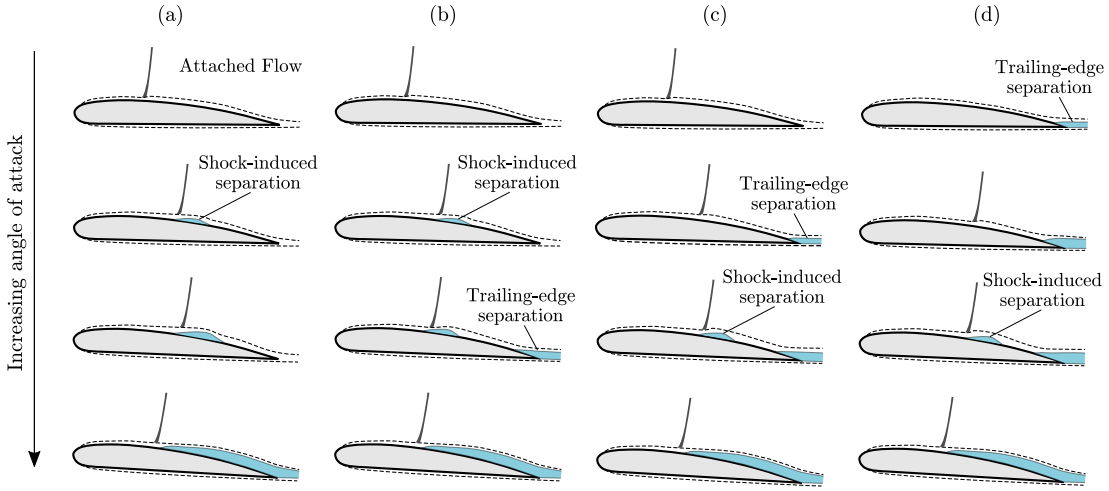

Figure 2.1: Types of high-speed flow separations on aerofoils; (a) shock-induced separation growing from the shock wave, (b) shock-induced separation provoking a trailing-edge separation, (c) rear separation provoked by the shock itself, and (d) trailing-edge separation exacerbated by the shock and shock-induced separation bubble (adapted from ESDU (1987)).

2.1 Conventional Techniques

2.1.1 Diagnosing Flow Separation

The nature of flow separation on both aerofoil sections and wings is a complex phenomenon. In the case of transonic flow, a region of supersonic flow develops which is terminated by a shock wave. The shock wave moves towards the trailing edge as the Mach number and/or angle of attack are increased. In turn, its strength increases until the pressure rise across the shock is sufficient to induce boundary-layer separation at the foot of the shock. This typically occurs as a separation bubble with the boundary layer reattaching further downstream. Initially, this might also be accompanied by trailing-edge separation depending on the geometry of the aerofoil together with the flow conditions. The different ways by which flow separations may occur on aerofoils at high speed are depicted in Fig. 2.1. The first case is the growth of a shock-induced separation bubble towards the trailing edge. Second, a trailing-edge separation can be provoked by the shock-induced separation. In the third case, the flow initially separates at the trailing edge before flow separation takes place at the shock foot. The fourth possibility is when the trailing-edge separation is exacerbated by the shock and the shock-induced separation.

In the case of three-dimensional wings, the appearance of flow separation is similar to that just described on aerofoils, assuming moderate sweep angles and medium to high aspect ratios. One way to diagnose the type of flow separation in the absence of skin friction data and flow visualisations is to analyse the surface pressure distributions. Figure 2.2 shows a typical pressure distribution at mid-semi-span of a swept-wing wind-tunnel model with a sweep angle of 25° (ESDU, 1987)). The pressure coefficient is

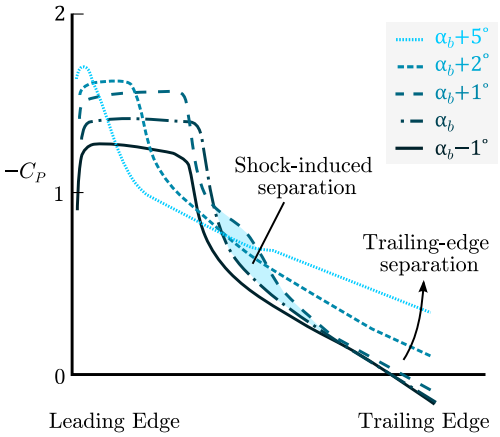

Figure 2.2: A typical pressure distribution on a moderately swept wing at the design Mach number (adapted from ESDU (1987)).

denoted by C_P whilst α_b represents the buffet-onset incidence. At the design Mach number, the embedded supersonic region continues to expand until α_b as the shock moves downstream with increasing angle of attack. As the latter is further incremented beyond α_b, a shock-induced separation bubble forms whilst the flow reattaches before reaching the trailing edge, as deduced from approximately constant pressure levels with angle of attack. The shock starts to move upstream with angle of attack beyond α_b and this becomes more apparent when the shock-induced separation merges with the trailing-edge separation above $(\alpha_b+2)°$. This so-called inverse shock motion takes place as flow separation reduces the effective aerodynamic incidence. The presence of a trailing-edge separation is inferred from diverging pressure levels with angle of attack.

The exact understanding of the flow evolution with angle of attack and the moment this boundary-layer separation first occurs is challenging since several factors affect the onset of flow separation. The dominant factors include the magnitude of the adverse pressure gradient within the pressure distribution, the local state of the boundary layer and the momentum thickness, amongst others. The observation of shock-induced separation merging with the trailing-edge separation described above is based on pressure data complemented by strain-gauge measurements, integrated normal force coefficient, and overall lift coefficient, as presented by ESDU (1987). The aim of this section is to introduce the reader to this method of diagnosing flow separation based on the interpretation of pressure distributions of a typical swept wing in transonic conditions.

2.1.2 Signal Processing

In signal processing terms, the experimental and numerical data herein contain unsteady signals that are referred to as random signals. Their variation in the future cannot be known exactly and only probabilistic statements about their variation are possible (Stoica & Moses, 2005). Mathematically, random signals consist of a random

sequence—an ensemble of possible realisations each having a probabilistic expectation. Discrete-time sequences do not have a finite energy, and hence, no discrete-time Fourier transform. Instead, random signals have finite average power and can be represented by an average power spectral density, referred to as power spectral density (PSD).

Let a sequence of random values with zero mean constitute the discrete-time signal

$$E\{x(t)\} = 0 \quad \forall \quad t \tag{2.1}$$

where E denotes the expectation operator that averages over the random sequence and $x(t)$ is the signal. Then, the PSD can be defined as

$$S(f) = \lim_{N\to\infty} E\left\{ \frac{1}{N} \left| \sum_{t=1}^{N} x(t) e^{-i2\pi ft} \right| \right\}. \tag{2.2}$$

This definition is useful for the following discussion on spectral estimation using non-parametric methods. Further motivation why $S(f)$ may be called a PSD and its properties are provided by Stoica & Moses (2005). For a signal consisting of N samples, $\{x(t)\}_{t=1}^{N}$, the expectation and limit operators in Eq. (2.2) cannot be applied. A classical way to estimate the spectral content is by applying a periodogram defined by

$$\hat{S}_p(f) = \frac{1}{N} \left| \sum_{t=1}^{N} x(t) e^{-i2\pi ft} \right|^2. \tag{2.3}$$

In practice, it is not possible to compute Eq. (2.3) over a continuum of frequencies and a sampling scheme is used for f, reducing the procedure to a discrete Fourier transform.

Several algorithms in the form of fast Fourier transforms have been developed to efficiently compute periodograms of large samples. Although periodograms provide adequate frequency resolution for sufficiently long signals, their spectral estimation is considered poor due to an inherently high variance. Several modifications have been introduced along the years, including the Bartlett (Bartlett, 1948) and Welch (Welch, 1967) methods. The Bartlett method reduces spectral variance by splitting signals into subsamples and then averaging the resulting periodograms at each frequency value. The Welch method provides further refinement by allowing overlapping data segments and windowing before computing each periodogram.

Consider N observations of the discrete-time signal to be split into a set of subsamples having M observations each, such that

$$x_j(t) = x((j-1)K + t) \tag{2.4}$$

for $t = 1, \ldots, M$ and $j = 1, \ldots B$, where B denotes the number of blocks or data segments. In the case that $K = M$, there are no overlapping segments and the subsampling

becomes identical to the Bartlett method ($B = N/M$). Typically, 50% overlapping is used in the Welch method ($K = M/2$ and $B \simeq 2N/M$). The windowed periodogram is defined as

$$\hat{S}_w(f) = \frac{1}{N} \left| \sum_{t=1}^{N} v(t)x(t)e^{-i2\pi ft} \right|^2 \tag{2.5}$$

where $v(t)$ denotes a weighting sequence (also called a temporal window or a taper). Using this definition, the windowed periodogram for the segment $x_j(t)$ is

$$\hat{S}_j(f) = \frac{1}{MP} \left| \sum_{t=1}^{M} v(t)x_j(t)e^{-i2\pi ft} \right|^2 \tag{2.6}$$

where P denotes the power of the temporal window

$$P = \frac{1}{M} \sum_{t=1}^{M} |v(t)|^2 . \tag{2.7}$$

Lastly, the windowed periodograms in Eq. (2.6) are averaged and the Welch PSD estimate is given by

$$\hat{S}_W(f) = \frac{1}{B} \sum_{j=1}^{B} \hat{S}_j(f). \tag{2.8}$$

The motive behind this method is that by allowing overlap, there is a greater number of periodograms to be averaged in Eq. (2.8) giving lower variance for the PSD estimate. Moreover, different windows can be used providing the user control over the bias/resolution properties (see Stoica & Moses (2005)). The choice of the window length is based on the selection between spectral resolution and statistical variance whilst its shape depends on the tradeoff between smearing and leakage effects. Therefore, a particular lag window can be regarded as a target point in the resolution/leakage tradeoff curve. Typically used windows are the *Hann* and *Hamming* windows which fall within the same class and have slightly varying parameters. The flexibility of the Welch method has rendered it as the standard signal processing method used in most shock-buffet experimental work (see for example Dandois (2016), Lawson *et al.* (2016) and Sugioka *et al.* (2018)), whereby signals from unsteady transducers are typically highly sampled and sufficiently long (thousands of cycles at the frequencies of interest).

Spectral estimation can also be performed using parametric methods whereby the signal is assumed to satisfy a model of a known functional form and the parameters of this model are estimated. Such methods, in particular the Burg method (Burg, 1967) employing an autoregressive model, are useful for short signals since they provide higher frequency resolution than non-parametric methods. In fact, autoregressive techniques are said to have *super-resolution* capabilities since they are able to resolve sinusoids which are very closely spaced in frequency and would not be resolved when using peri-

odograms (Stoica & Moses, 2005). The Burg method is used herein for the numerical time-accurate data since the computationally expensive simulations are shorter than the experimental signals and have very high temporal resolution of $\mathcal{O}$(MHz).

Cross-spectral analysis is a complementary technique that provides a measure of the linear relation between multiple signals. The statistical relation between two stationary signals $x(t)$ and $y(t)$ can be measured from the magnitude-squared coherence

$$C_{xy}(f) = \frac{|S_{xy}(f)|^2}{S_{xx}(f)S_{yy}(f)} \tag{2.9}$$

where S_{xy} is the cross-spectrum of the two signals whilst S_{xx} and S_{yy} denote their respective PSDs. The phase angle between the signals is

$$\phi_{xy}(f) = \arctan\left(\frac{\Re\{S_{xy}(f)\}}{\Im\{S_{xy}(f)\}}\right). \tag{2.10}$$

This technique is particularly useful herein as it allows the computation of phase speeds for the frequency bands at which the signals have high coherence (Dandois, 2016; Paladini *et al.*, 2018; Sugioka *et al.*, 2018). The propagation velocity U_p can be computed from the phase angle variation with distance at a selected frequency

$$U_p = 2\pi f \frac{\Delta s}{\Delta \phi} \tag{2.11}$$

where Δs represents the physical distance between the sensors located at s_1 and s_2, respectively, while $\Delta\phi = \phi_{s_2} - \phi_{s_1}$ is the phase difference between each sensor with respect to the reference sensor computed from Eq. (2.10). Alternatively, the propagation velocity can also be computed between two discrete sensors for a range of frequencies

$$U_p = 2\pi \Delta s \frac{\Delta f}{\Delta \phi} \tag{2.12}$$

where $\Delta f = f_2 - f_1$ and $\Delta\phi = \phi(f_2) - \phi(f_1)$.

2.2 Modal Methods

A general overview and a brief formulation of two widely used data-based modal decomposition techniques, namely, POD and DMD follows. The modal decomposition of input data snapshots into POD and DMD modes, each having a spatial and temporal component, is depicted in Fig. 2.3. The modal analysis framework developed herein integrates the parallelised `modred` library (Belson *et al.*, 2014) and employs the vector-space approach for the modal decomposition. In this approach, the snapshots are treated as vectors and are not stacked into a large input data matrix. This enables the computation of the modes from the whole dataset, as this formulation removes the

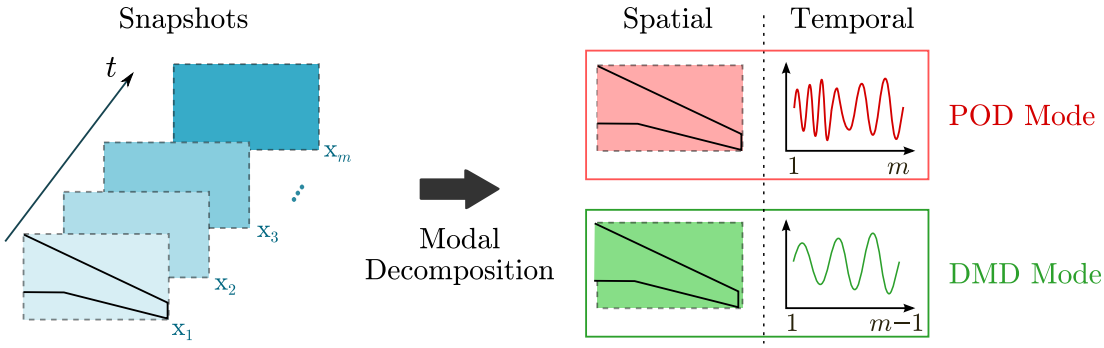

Figure 2.3: Modal decomposition of data snapshots into POD and DMD modes.

requirement of storing large matrices in computer memory. Further detail on the specific implementation of POD and DMD in the modred library is given in Appendix A.

2.2.1 Proper Orthogonal Decomposition

POD gives a set of orthonormal modes that are ranked by their contribution in optimising the variance of the input dataset in a least squares sense. Whilst this procedure is popular in various fields and known by a variety of names, such as Karhunen-Loève procedure and principal component analysis, the key idea is to represent the dataset by a minimum number of modes which capture the maximum amount of fluctuation. This technique was first used in the analysis of fluid flows by Lumley (1967) in order to extract coherent structures from a turbulent flow field. There are several ways to perform POD including the spatial (classical) method, the snapshot method and the direct singular value decomposition method (Taira *et al.*, 2017). The classical method is usually impractical for high-dimensional datasets, since the correlation matrix constitutes a matrix eigenvalue problem of size $n \times n$, where n is the dimension of the dataset, hence becoming restrictive. A better alternative is the method of snapshots (Sirovich, 1987) which uses a temporal correlation matrix giving rise to a much smaller eigenvalue problem of size $m \times m$, where m is the total number of snapshots and $m \ll n$. However, it is important to have a sufficient number of snapshots such that fluctuations of the flow features of interest are well resolved in time. The interested reader is referred to the publications by Berkooz *et al.* (1993), Holmes *et al.* (2012) and Taira *et al.* (2017) that describe its application to fluid flows and its connection to other methods. A brief formulation on the method of snapshots follows.

Consider an input dataset generalised by a set of vectors $\mathbf{x}_i$, where $\mathbf{x}_i$ represents an input vector of size n at each instance in time (for $i = 1, \ldots, m$). The data matrix $\mathbf{X}$ consists of m snapshots, $\mathbf{X} = [\mathbf{x}_i, \ldots, \mathbf{x}_m]$. When applying POD to a fluid flow, it is common practice to take mean-subtracted vector fields, such that the unsteady

component can be decomposed as

$$\mathbf{x}_i - \overline{\mathbf{x}} = \sum_{j=1}^{m} a_{i,j}\boldsymbol{\varphi}_j \tag{2.13}$$

where $\overline{\mathbf{x}} = \frac{1}{m}\sum_{i=1}^{m}\mathbf{x}_i$ and denotes the time average, $a_{i,j}$ represents the expansion coefficients at each time instant and $\boldsymbol{\varphi}_j$ are the spatial modes. Given the size of the datasets analysed herein ($n \approx 1 \times 10^6$ and $m = 10\,000$ for each experimental flow condition while $n \approx 50 \times 10^6$ and $m \approx 300$ for each numerical simulation), the method of snapshots is employed. Hereby, the following eigenvalue problem is solved

$$\mathbf{X}^T\mathbf{X}\boldsymbol{\psi}_j = \lambda_j\boldsymbol{\psi}_j, \quad \boldsymbol{\psi}_j \in \mathbb{R}^m \tag{2.14}$$

where $\boldsymbol{\psi}_j$ are the eigenvectors and λ_j represent the eigenvalues. The POD modes can then be computed from

$$\boldsymbol{\varphi}_j = \mathbf{X}\boldsymbol{\psi}_j\lambda_j^{-1/2} \in \mathbb{R}^m, \quad j = 1, \ldots, m \tag{2.15}$$

which can be written in matrix form as

$$\boldsymbol{\Phi} = \mathbf{X}\boldsymbol{\Psi}\boldsymbol{\Lambda}^{-1/2}, \quad \boldsymbol{\Phi} \in \mathbb{R}^{n\times m}. \tag{2.16}$$

2.2.2 Dynamic Mode Decomposition

DMD is a more recent technique that provides modes with a single characteristic frequency and growth/decay rate. This is the main advantage of this method since flow features can be isolated based on frequency content, in contrast with POD, where each POD mode is associated with a range of frequencies. DMD is purely data based, rooted in linear algebra, and relies on the eigendecomposition of a best-fit linear operator that approximates the dynamics present in the data (Taira *et al.*, 2017). Moreover, it enables the analysis of dynamical features and can also be applied when the dynamics are nonlinear, whereby structures lying on an attractor and oscillating at particular frequencies can be extracted (Tu *et al.*, 2014). However, in contrast with POD, resulting dynamic modes are not necessarily orthogonal, which can be a disadvantage in certain analyses such as when building reduced-order models. This does not pose a limitation herein since DMD is applied to isolate flow phenomena based on particular frequencies.

Requirements for data collection are the same for both modal decomposition methods. However, whilst it is typical to use mean-subtracted snapshots for POD to focus on the unsteady component only, the mean is retained for DMD such that resulting DMD modes can have *any* frequency subject to the Nyquist frequency. If the mean is subtracted, DMD would otherwise reduce to a discrete Fourier transform, as explained by Chen *et al.* (2012). The standard DMD algorithm introduced by Schmid (2010)

arranges snapshots into separate matrices $\mathbf{X}_1$ and $\mathbf{X}_2$ which are shifted in time, where

$$\mathbf{X}_1 = [\mathbf{x}_1, \ldots, \mathbf{x}_{m-1}] \in \mathbb{R}^{n \times m-1} \quad \text{and} \quad \mathbf{X}_2 = [\mathbf{x}_2, \ldots, \mathbf{x}_m] \in \mathbb{R}^{n \times m-1}. \tag{2.17}$$

It is assumed that each snapshot in time, $\mathbf{x}_i$ (for $i = 1, \ldots, m-1$), is linked to the next snapshot, $\mathbf{x}_{i+1}$, via a linear mapping $\boldsymbol{A}$, and, if the data are dynamically nonlinear, $\boldsymbol{A}$ represents an operator which approximates these dynamics, such that

$$\mathbf{X}_2 = \boldsymbol{A}\mathbf{X}_1. \tag{2.18}$$

Rather than computing the eigendecomposition of $\boldsymbol{A}$ explicitly, which is computationally expensive since $n \gg m$, several algorithms have been introduced to compute the DMD modes and eigenvalues, as discussed by Tu *et al.* (2014). The spatial structures are contained in the DMD modes $\boldsymbol{\varphi}_j$ (for $j = 1, \ldots, m-1$) which oscillate and/or grow/decay at characteristic values defined by the DMD eigenvalues μ_j. The resulting DMD eigenvalues can be mapped logarithmically as

$$\lambda_j = \frac{\ln(\mu_j)}{2\pi\Delta t} \tag{2.19}$$

where Δt denotes the time step between successive snapshots, equivalent to the reciprocal of the sampling frequency f_s. The corresponding growth/decay rate, σ_j, and frequency of oscillation, f_j, can be obtained from the real and imaginary components,

$$\sigma_j = \Re\{\lambda_j\} \quad \text{and} \quad f_j = \Im\{\lambda_j\}. \tag{2.20}$$

The contribution of each DMD mode $\boldsymbol{\varphi}_j$ to the original snapshots can be inferred by reconstructing the flow field from a chosen number, r, of DMD modes,

$$\mathbf{x}_i = \sum_{j=1}^{r} d_{i,j}\boldsymbol{\varphi}_j \tag{2.21}$$

where $d_{i,j}$ represents the scalar coefficient used for the reconstruction. Those coefficients projecting each snapshot onto the modes can be computed either via a least-squares projection onto projected DMD modes or from a biorthogonal projection using adjoint DMD modes (refer to Tu *et al.* (2014) for the motivation of referring to DMD modes resulting from the standard algorithm as projected). In the case of linearly consistent snapshots whereby the rank of the coefficient and augmented matrices is the same, the projection coefficients encode the time evolution, useful in identifying dynamically relevant modes. Since the introduction of the *standard* DMD method, a number of modifications and extensions have been developed (Taira *et al.*, 2017). A low-memory variant of the DMD algorithm (Tu *et al.*, 2014) is employed herein.

Chapter 3

RBC12 Half Model Test Case

The RBC12 wind-tunnel half-model is a wing-fuselage configuration, with no pylons or tailplane, representing a commercial aircraft of a typical 1970s/1980s design. The wind-tunnel model was manufactured using steel and designed for a Mach number of 0.80. The following geometrical details were derived from a coordinate measurement machine and were used to create an accurate computer-aided design (CAD) model required for the numerical work. The model has a reference area of $0.2959\,\mathrm{m}^2$ and a mean aerodynamic chord (MAC) of 0.2789 m. The model is raised by a plinth of 0.019 m (base plate or gap filler profile plate) to reduce the influence of the floor boundary layer which is included in the semi-span measurement of 1.104 m. Thus, the reference semi-span, b, is taken as 1.0846 m. The aspect ratio is 7.78, the leading-edge sweep angle, Λ_{LE}, is 28.3° and the quarter-chord sweep angle, $\Lambda_{c/4}$, is 25°. The scale factor of the model with respect to the full size aircraft dimensions is 17.5. The half-model mounted to the Aircraft Research Association (ARA) Transonic Wind Tunnel (TWT) floor and further geometrical details are presented in Fig. 3.1.

The RBC12 model has been extensively tested in the ARA TWT with specific focus on shock buffet by Lawson *et al.* (2016). Several buffet onset indicators using both steady and dynamic data were compared, as discussed in detail later in Section 4.2. The structural frequencies of the model have been reported as 38 Hz at first wing bending, 125 and 255 Hz at higher-frequency predominantly bending modes, and 328 Hz at the first torsion mode. These were determined by analysing the root strain gauge and accelerometer signals during a wind-off tap test and are available in (Lawson & Greenwell, 2015). Furthermore, aeroelastic modes similar to those at wind-off condition were obtained from the wind-on response at the design Mach number, $M = 0.80$, and low incidence. An additional peak at 114 Hz is also present and is thought to be the second harmonic of the first bending mode. The structural frequencies at wind on can be seen in Fig. 3.2 depicting power spectral density data of root strain gauge and wing-tip accelerometer signals at the design Mach number and angle of attack $\alpha = 0°$.

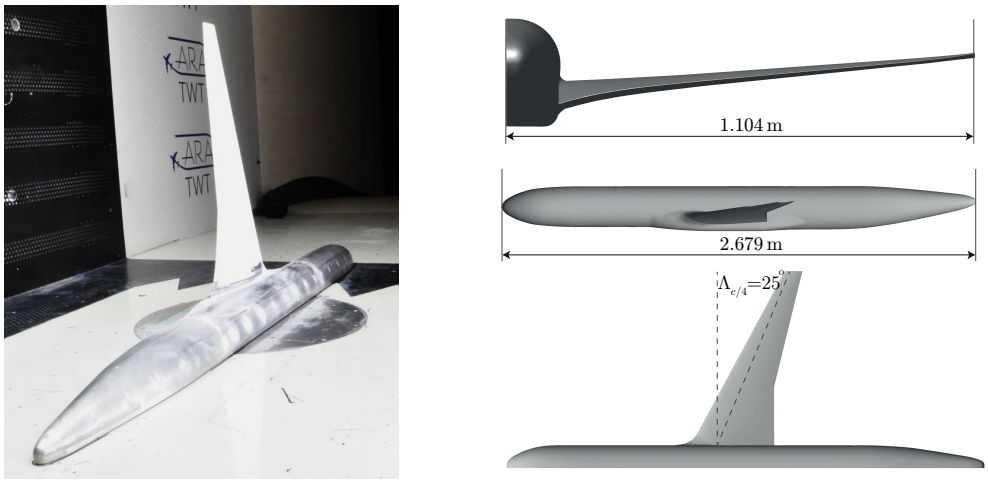

(a) Installation in ARA TWT **(b)** Geometrical information

Figure 3.1: The RBC12 half-model **(a)** mounted to the wind-tunnel floor and **(b)** some geometrical information (note, semi-span of 1.104 m includes the model plinth of 0.019 m).

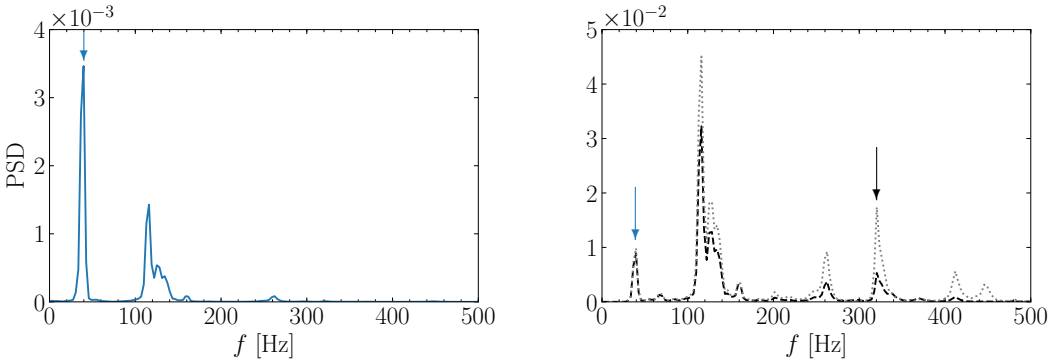

(a) Wind-on root strain gauge **(b)** Wind-on tip accelerometers

Figure 3.2: Wind-on structural frequencies from root strain gauge (——) and accelerometers at two chordwise locations close to the wing tip (- - - and ·····). The first bending mode is denoted by the blue arrow and the black arrow represents the first torsion mode.

Chapter 4

Experimental Analysis

The analysis presented in this chapter is based on experimental tests conducted in early 2015 within the European Commission Clean Sky Buffet Control of Transonic Wings (BUCOLIC) project. The BUCOLIC project was part of the Buffet Control Technology Stream under the Smart Fixed Wing Aircraft strategic Clean Sky programme. The sheer quantity of data and complexity of the flow physics precluded a complete study within the project time frame, leaving much to be investigated and learned, motivating the study herein. The experiments were conducted in the Aircraft Research Association Transonic Wind Tunnel using a half-model wing-fuselage configuration, called RBC12, representing a commercial aircraft of a typical 1970s/1980s design. This model was highly instrumented including conventional static pressure taps, unsteady pressure transducers, accelerometers and a root strain gauge. In addition, the model was coated with dynamic pressure-sensitive paint providing unsteady surface pressure measurements of high spatial and temporal resolution. The wind-tunnel testing was extensive, covering angles of attack from pre-onset to well beyond buffet onset at seven Mach numbers between 0.70 and 0.84. Moreover, four configurations were tested; the clean wing, two different arrays with vane vortex generators, and an alternative transition location. The spatial coverage and the temporal resolution of the data together with the wide range of flow conditions and configurations render this dataset unique, enabling deep analysis into transonic shock buffet. Other datasets have either limited spatial and/or temporal resolution or a smaller range of flow conditions. This chapter presents detailed analysis of the clean wing configuration based on traditional signal processing tools in addition to modal analysis of the dynamic pressure-sensitive paint data using both proper orthogonal decomposition and dynamic mode decomposition. Furthermore, the influence of passive flow control by vane vortex generators on buffet onset is scrutinised by analysing two vortex-generator arrays.

4.1 Experimental Description and Data Cleaning

The necessary background to comprehend the analysis is introduced to the reader. Details of the experimental test campaign including the wind-tunnel facility and the test-specific model instrumentation are provided. Data cleaning including flow corrections and the methodology for the dynamic pressure-sensitive paint data processing are then discussed. For further information on the experimental testing, the reader is referred to Lawson (2015) and Lawson & Greenwell (2015).

4.1.1 Wind-Tunnel Facility

The ARA Transonic Wind Tunnel is a closed-circuit, continuous type transonic facility with an operating Mach number of up to 1.4. The test section is 2.74 m wide by 2.44 m high and the stagnation pressure can be varied between 80 and 120 kPa. During the tests analysed herein, this was maintained at around 100 kPa and the stagnation temperature was between 290 and 310 K, giving a Reynolds number of approximately 13 million per metre at Mach 0.80. The working section ceiling and side walls are 22% porous whilst the floor is solid. Turbulence levels in the test section are relatively low for this type of facility and were measured at 0.1% longitudinally (streamwise direction u) and 0.2% laterally (along the v direction) (Green *et al.*, 1992).

4.1.2 Instrumentation and Data Acquisition

The existing RBC12 half-model (a port wing) introduced in Chapter 3 was modified with dedicated instrumentation for the BUCOLIC shock-buffet focused test campaign allowing a wide range of measurements. The model was mounted on the ARA five-component (excluding side force along the fuselage axis) balance having two independent sets of strain gauges from which averaged aerodynamic forces (normal and axial force) and moments (pitching, rolling and yawing moment) were derived. Mean pressure data were obtained from 369 static pressure taps along the fuselage and wing (162 on the upper surface, 112 on the lower surface) using seven 64-port Electronic Pressure Scanner modules logged to a steady-state data acquisition system. Conventional unsteady model instrumentation amounted to 27 unsteady transducers (24 on upper surface, 3 on lower surface), 8 accelerometers and a root strain gauge. The unsteady signals were acquired via dedicated channels at 100 kHz over ten-second samples using the dynamic data acquisition system (DDAS). This system is capable of sampling all 224 channels simultaneously with a total of 57 channels employed for these tests. The latter includes the model instrumentation in addition to other sensors located on the wind-tunnel floor, walls and roof. Anti-aliasing was achieved digitally via a sigma-delta type analogue-to-digital converter by means of over-sampling, rather than through an analogue low-pass filter.

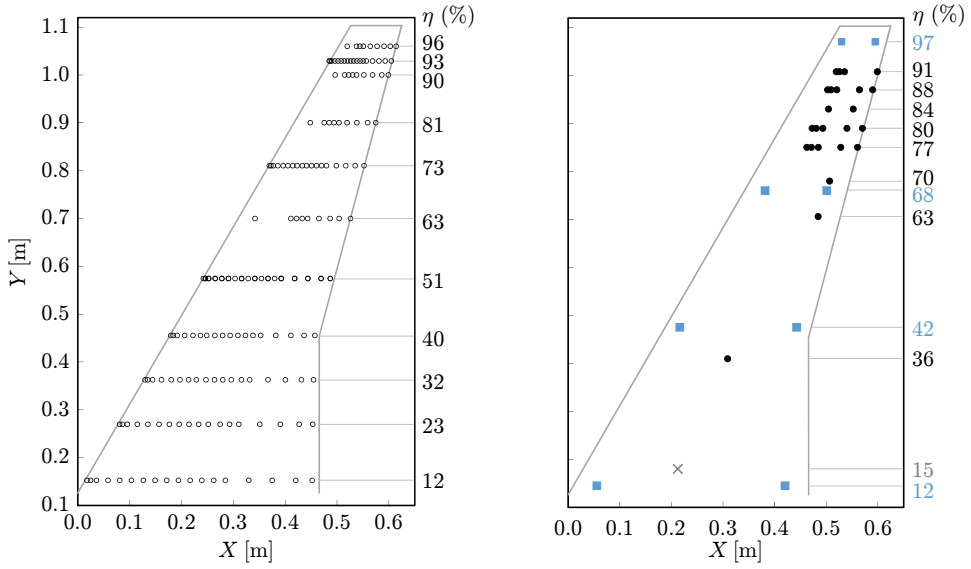

(a) 162 static pressure taps **(b)** Unsteady instrumentation

Figure 4.1: Model instrumentation on upper surface. Static pressure taps are shown by open circles whereas unsteady pressure transducers, accelerometers and a root strain gauge are denoted by the black filled circles, blue filled squares, and the grey cross, respectively.

The locations of the upper-surface static pressure taps and unsteady instrumentation are shown in Fig. 4.1, where X and Y denote the chordwise and spanwise coordinates along the model axes, respectively. Note that since the half model is mounted to the wind-tunnel floor, the spanwise direction of the model corresponds to the wind tunnel floor normal direction. The spanwise position is made dimensionless by the reference semi-span b after subtracting the plinth thickness, such that $\eta = (Y - 0.019)/b$. Herein, the precise locations of the transducers are provided by the local chordwise coordinate, $x = X - X_{LE}$, and the local chord length, $c = X_{TE} - X_{LE}$, where subscripts LE and TE denote leading and trailing edge, respectively.

Additionally, a DPSP system was employed consisting of two high-speed Vision Research Phantom (v1610 and v1611) synchronised cameras, installed inside the wind-tunnel side walls to view the upper and lower wing surfaces. The model was coated with fast-response PSP developed by Innovative Scientific Solutions Incorporated (Crafton *et al.*, 2015) and illuminated with high power ultra-violet light-emitting diode lights. Critically, this system captured the three-dimensional flow development through unsteady surface pressure measurements of high spatial and temporal resolution. Data were typically recorded at 4000 frames-per-second (fps) for five seconds, except for a single run of the clean configuration at $M = 0.80$, using 2000 fps for ten seconds. The camera resolution was 1280 pixel by 800 pixel, equivalent to around 1.3 pixel/mm on the surface, a bit depth of 12 bits, and an exposure time of between 150 and 250 μs.

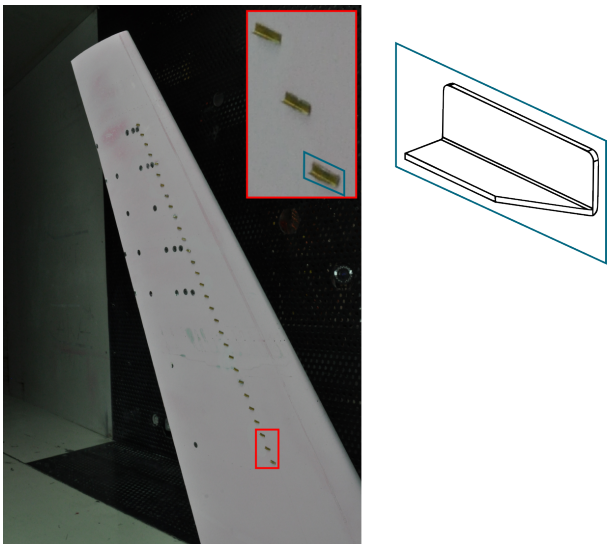

Figure 4.2: The full array with 30 vane vortex generators.

4.1.3 Configurations and Test Campaign

The wind-tunnel test campaign included four configurations, each tested at a wide range of flow conditions: (i) clean wing, (ii) full array of 30 vane vortex generators, (iii) sparse array of 8 vane vortex generators, and (iv) clean wing with alternative transition location. Transition was fixed on both fuselage and wing by means of sparsely distributed Ballotini set in a thin film of epoxy resin. The transition location for configurations (i) through (iii) on the wing upper surface is 10% local chord at the tip, 14% at the crank and 15% at the root, while this is at 5% on the lower surface. The alternative transition location in configuration (iv) on the upper surface is farther downstream at 25% chord, with the lower surface unaltered. The fuselage was tripped 104 mm aft of the nose throughout. Laminar-to-turbulent transition was verified based on time-averaged temperature traces from infrared thermography employed during particular runs.

Passive buffet control was studied by means of vane vortex generators (VGs). The VG parameters were selected for maximum separation control rather than minimum drag, following the guidelines in ESDU (1995). The VGs were set toed-in, co-rotating at 17° with respect to the fuselage centreline, such that the vane angle was 25°, based on a local flow angle calculation of 8° inboard. The VG height of 1.3 mm is equal to the estimated boundary-layer thickness just upstream of the shock location from a numerical simulation in the vicinity of buffet onset at $M = 0.80$. The VGs have a bottom length of 5 mm, taper ratio of 0.6, aspect ratio of 1.3 and 60° sweep. The devices are the same in both full and sparse VG configurations, since for the latter, three out of every four VGs were removed. These were located at 32% local chord between 63% and 91% semi-span. For the full VG array, shown in Fig. 4.2, the spanwise spacing is equal to 10 mm resulting in a spanwise spacing-to-height ratio of 7.7.

Table 4.1: Summary of wind-tunnel flow conditions for three configurations.

M	T (K)	P (kPa)	U_∞ (m/s)	ρ (kg/m^3)	μ (kg m^{-1}s^{-1}, $\times 10^{-5}$)	Re ($\times 10^6$)
Clean Configuration						
0.70	271	70.4	231	0.91	1.71	3.42
0.74	269	67.9	243	0.88	1.70	3.51
0.76	271	67.1	251	0.86	1.71	3.54
0.78	267	65.9	257	0.86	1.69	3.66
0.80	268	65.3	263	0.85	1.69	3.67
0.82	266	63.5	268	0.83	1.68	3.70
0.84	264	61.6	274	0.81	1.67	3.71
Full VG Configuration						
0.78	267	65.6	256	0.86	1.69	3.62
0.80	267	64.2	262	0.84	1.69	3.63
0.82	265	63.0	268	0.83	1.68	3.69
Sparse VG Configuration						
0.78	267	66.3	256	0.87	1.69	3.66
0.80	265	65.0	261	0.85	1.68	3.71
0.82	266	63.8	268	0.84	1.68	3.72

The analysis presented herein focuses primarily on the first configuration, i.e., the clean wing with nominal transition, tested extensively at a range of flow conditions from $M = 0.70$ to 0.84. In contrast, the configurations with vane vortex generators were tested between $M = 0.78$ and 0.82. At each Mach number, DDAS data were measured from fine pitch runs, typically with 0.1° angle of attack increments, whereas data from DDAS and DPSP measurements were acquired simultaneously at coarser increments of approximately 0.2°, depending on the Mach number. The angle of attack was typically varied between 0° and 8°, resulting in a total of 911 DDAS points and 274 DPSP points. The Reynolds number variation throughout the runs was between 2.7 and 3.9 million with MAC as reference length. The flow conditions of the data analysed herein, including the freestream static temperature, T, static pressure, P, velocity, U_∞, density, ρ, and the dynamic viscosity, μ, for the test runs with simultaneous DDAS and DPSP acquisition are summarised in Table 4.1. The values have been averaged over the test run since conditions in the wind tunnel undergo slight variation.

4.1.4 Flow Corrections

The experimental data reported herein have been corrected for wind-tunnel interference effects, compatible with previous work (Lawson *et al.*, 2016). For such tests where the half-model is mounted to the floor, interference effects arise from the floor and side walls. Even though this is not an issue in incremental testing where relative differences between various configurations are explored, the influence on flow development

is important when comparing with numerical simulation in absolute terms whereby interference-free flow is considered. Interference effects can be classified into two groups: (i) effects on Mach number and (ii) effects on incidence.

Solid blockage due to the presence of the model in the wind tunnel accounts for interference on Mach number. An empirical correction employing the standard method of infinite array sources, described by Garner *et al.* (1966) using the model longitudinal area distribution and the effect of porosity, is applied to correctly set the tunnel speed. The calculated blockage correction is quite small, ranging between -0.01% and -0.12% of Mach number at the smallest and largest Mach numbers tested, respectively.

Effects on aerodynamic incidence are believed to occur due to the following factors. A gap exists between the model and the floor to enable force and moment measurement. Moreover, the fuselage is immersed in the floor boundary layer. Even though the model is raised by a plinth (base plate or gap filler profile plate) that is approximately equal to the floor boundary-layer displacement thickness, there is less lift generated by the fuselage and an overall small reduction in lift-curve slope. Furthermore, for the configurations coated with DPSP, the paint results in a thicker boundary layer due to increased surface roughness, which in effect causes a slight upstream shock position. Therefore, three corrections are applied to correct for aerodynamic incidence. First, a wall-constraint correction is calculated as a function of wing span and area, lift coefficient, and wall porosity and is equal to $\Delta\alpha = -(0.6351 C_L)^\circ$. Second, for the configurations coated with DPSP, a small paint-effect correction is introduced. The influence on effective aerodynamic incidence was estimated at around -0.1° by comparing pressure distributions of the painted and the unpainted model at the same flow conditions (Lawson & Greenwell, 2015). Third, the flow in the vicinity of a wind-tunnel model may experience a small flow angle. Half models cannot be inverted and therefore an estimate has to be used by comparing half model zero-lift incidence with that of the full model. Full-model data of the RBC12 was not available and a flow angle of approximately -0.35° was estimated from the average flow angle correction of several other models tested in the ARA TWT (Lawson & Greenwell, 2015). For these reasons, only the wall constraint and paint effect corrections have been directly applied to the experimental data. However, better agreement with the numerical data is achieved when also including the flow angle estimate, as discussed in Section 5.3.2.

4.1.5 Dynamic Pressure-Sensitive Paint Processing

The acquired images were pre-processed to convert image intensities into static pressure data using an in-house software (Lawson *et al.*, 2016). First, the images are aligned to compensate for small model and camera movements caused by the wind-tunnel environment, whereby each frame is aligned to a wind-off image via an image-registration algorithm based on cross-correlation. Second, the variation in illumination over the

recording time is then accounted for by normalising the images by a high-order curve fit of the lamp-power history. Third, intensity ratios are calculated by the quotient of the wind-off and wind-on images, such that any discrepancies in intensity over the wing are also corrected. Finally, the calibration between image intensity and static pressure is applied to every image, based on a least-squares relationship between the image-intensity ratios in the proximity of various reference static pressure taps.

Further details of this involved process and its validation are described by Lawson *et al.* (2016) reporting satisfactory agreement between the time-averaged DPSP data and the static pressure taps with a maximum deviation of within $\pm 2000\,\mathrm{Pa}$ (corresponding to $\pm 3\%$ of reference stagnation pressure at the design Mach number). This uncertainty was lower at various spanwise stations and chordwise positions. More importantly, excellent agreement between the frequency spectra from unsteady pressure transducers and adjacent pixel data was obtained, rendering this optical measurement technique suitable to analyse the unsteady surface pressure flow field with confidence. Such comparisons are available in the report by Lawson & Greenwell (2015).

4.2 Shock Buffet and Buffeting Onset Indication

Several buffet-onset indicators have been devised over the years to define buffet onset from wind-tunnel measurements. These indicators are summarised in ESDU (1987) based on several wind-tunnel and flight tests compiled in AGARD (1975). Aerodynamic indicators include trailing-edge pressure divergence, lift-curve slope reduction, and breaks in the pitching moment and axial force variation with incidence. Generally, such criteria rely on the assumption that sufficiently significant flow separation causes a deviation from a linear low-incidence trend where the flow remains attached. Moreover, these indicators can be derived from steady experimental data and easily extend to numerical data. However, it is emphasised that all methods are approximate and do not always result in close agreement with flight test data. In the case of experimental testing, the structural response can be directly measured from root strain gauges and wing-tip accelerometers. Dynamic measurements of root strain and wing-tip acceleration are considered essential for the prediction of wing buffeting from wind-tunnel tests, giving the closest predictions when compared to full-scale flight. Furthermore, whilst steady aerodynamic indicators can predict initial flow separation, a very small separated area generally gives rise to high-frequency excitations, without inducing significant buffeting. In this context, the term buffeting refers to the structural response, whereas buffet relates to the fluid unsteadiness. The onset of the structural response requires a larger separation to excite the wing and might not coincide with the buffet onset incidence predicted by aerodynamic indicators.

Lawson *et al.* (2016) scrutinised several of these criteria using steady and dynamic data for the RBC12 half model. Good agreement between the strain gauge and ac-

celerometer divergence, which mainly respond to wing bending, and aerodynamic indicators based on trailing-edge pressure divergence at 80% semi-span and lift-curve slope reduction was reported. The criteria based on axial force and pitching moment were less reliable. It should be noted that the local criterion based on trailing-edge pressure divergence requires separation to first occur at the trailing edge. In the case of a finite wing, this is sensitive to the choice of spanwise location. Furthermore, the lift-curve slope reduction method relies on the definition of the linear slope, for which there are various, and which also changes with configuration.

It can be hypothesised that the location where flow separation first occurs and its spanwise extent varies with Mach number and configuration. Therefore, in order to allow an investigation across a range of flow conditions, a global criterion based on the structural response is preferred, such as the strain-gauge signal. Since the strain gauge responds primarily to wing bending, this defines the onset of structural buffeting, even though it is commonly referred to as a shock-buffet onset indicator. It should be emphasised that the shock can exhibit unsteadiness before an indicated break from a linear trend, rendering an unequivocal definition of shock-buffet onset quite intricate.

There are several ways of measuring the wing buffeting magnitude using strain-gauge data of nominally rigid wind-tunnel models. One approach is to calculate a buffet excitation parameter for a particular structural mode as proposed by Jones (1971). This method requires careful recording of the model's wing-tip acceleration, structural damping and generalised mass in a particular mode shape, which may not be possible. Another method which is typically used for comparative wind-tunnel tests, for example when comparing different wing designs tested in several wind tunnels, is based on the relationship between the measured model response and the level of flow unsteadiness at the frequency of interest. A buffeting coefficient C_B is calculated, independent of the mass and damping properties of the model. Furthermore, various definitions for C_B exist in the literature. Mabey (1971) defines C_B based on the response at a particular structural mode normalised by the dynamic pressure whereas Balakrishna & Acheson (2011) define C_B by the wide-band signal normalised by the zero angle of attack response. In order to enable comparisons between various wind-tunnel models and flight-test data, Mabey (1971) also proposed a method to compute a corrected buffeting coefficient, C_B'', which takes into account the background tunnel-induced buffeting. Lawson & Greenwell (2015) estimated the background unsteadiness and the buffet excitation parameter to calculate C_B'', showing that buffeting for the RBC12 is within the light buffeting range (Mabey, 1971).

However, the strain-gauge response can also be used as an absolute measure. Herein, the structural buffeting onset is defined from the dimensional buffeting coefficient as a function of Mach number and angle of attack. This is the same approach used by Balakrishna & Acheson (2011) except that the buffeting coefficient is not normalised by the zero angle of attack response herein, as this would vary with Mach number. The

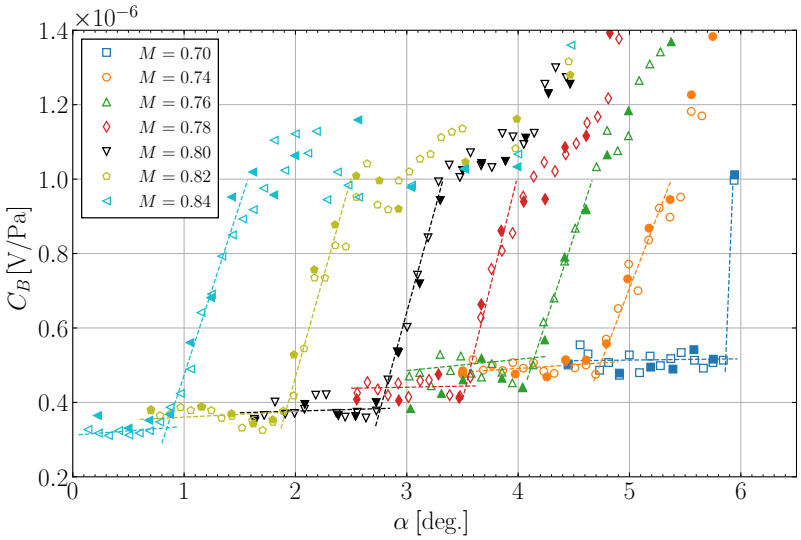

Figure 4.3: Dimensional buffeting coefficient over angle of attack for a range of Mach numbers for the clean configuration; open symbols represent fine-pitch runs with DDAS, filled symbols denote coarser-pitch runs that also include DPSP acquisition.

dimensional buffeting coefficient is computed in the time-domain from the root-mean-square (RMS) of the ten-second, unfiltered strain-gauge signal consisting of $n = 1 \times 10^6$ values, $V_\epsilon(t)$ in Volts, normalised by dynamic pressure, q,

$$C_B(M, \alpha) = \frac{\sqrt{\frac{1}{n}(V_\epsilon(1)^2 + V_\epsilon(2)^2 + \ldots + V_\epsilon(n)^2)}}{q}. \tag{4.1}$$

It should be noted that C_B is readily available from the steady-state data acquisition system computed by RMS amplifiers. However, a more accurate RMS measurement is achieved by using the highly-sampled data from the DDAS.

The dimensional buffeting coefficient for the clean configuration, computed using Eq. (4.1) and the DDAS signal, as a function of angle of attack for a range of Mach numbers, is shown in Fig. 4.3. Both fine-pitch runs with DDAS and data points having DPSP acquisition are presented. Throughout the Mach number range, a similar response prior to the onset of buffeting is observed due to the wind-tunnel background unsteadiness. As the angle of attack is further increased, a sharp rise in C_B indicates buffeting onset. This holds true especially at the lower Mach numbers ($M \leq 0.80$), at which α_b can be defined to within $\pm 0.05°$ from the fine-pitch runs. However, at the higher Mach numbers, $M = 0.82$ and 0.84, identifying a clear buffet-onset incidence is more difficult since the divergence is more gradual. Furthermore, the large jump in buffeting levels for the clean wing at $M = 0.70$ and $\alpha = 5.9°$ occurs as the shock shifts upstream of the boundary-layer tripping and causes a large separation region.

This is also challenging for the configurations with VGs, with the corresponding data depicted in Fig. 4.4. For this reason, the reference buffet-onset incidence, summarised

Table 4.2: Buffet-onset incidence as obtained from strain-gauge data for three configurations.

	Mach Number						
	0.70	0.74	0.76	0.78	0.80	0.82	0.84
Clean	5.9°	4.7°	4.1°	3.5°	2.7°	1.9°	0.8°
Sparse VG				3.7°	2.9°	2.1°	
Full VG				3.9°	3.1°	2.3°	

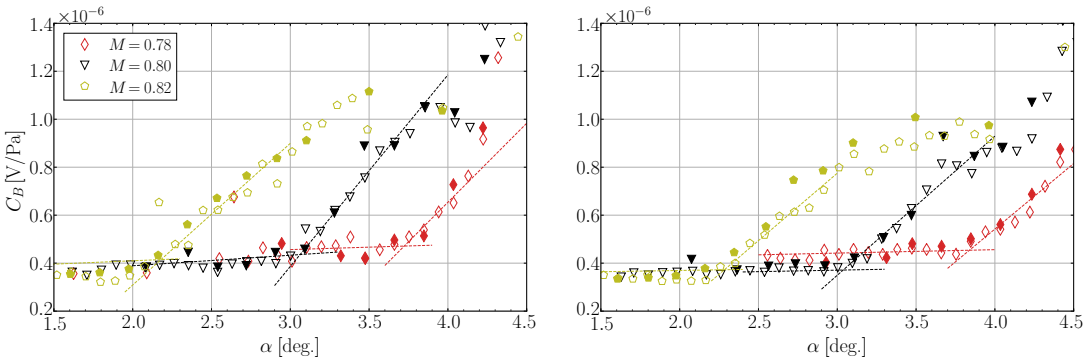

(a) Sparse VG configuration **(b)** Full VG configuration

Figure 4.4: Dimensional buffeting coefficient over angle of attack for a range of Mach numbers for the VG configurations. Same symbol notation as in Fig. 4.3.

in Table 4.2, is taken as the cross-over point between linear trends computed at low incidence and during the initial rise in buffeting magnitude. The VGs are effective between $M = 0.78$ and 0.82, delaying buffet onset by up to 0.4°. Furthermore, it is clear that the rise in buffeting levels is more gradual relative to the clean wing, especially for the full VG configuration. This implies that the VGs also alleviate buffeting levels beyond onset. However, at certain flow conditions, typically at lower Mach number and higher angle of attack, the VGs become counteractive and increase buffeting levels (e.g. sparse VG, $M = 0.78$, $\alpha > 4.2°$). Visualisation of the DPSP data and static pressure distributions reveals that the shock sits upstream of the VGs and the chordwise extent of the shock unsteadiness increases drastically.

It should be noted that while these figures show unfiltered data, the same onset points are found from the strain-gauge signal band-pass filtered at the first wing-bending frequency. This is expected since the first wing-bending response dominates the strain-gauge output of such a steel model with low structural damping.

4.3 Conventional Analysis

The data from static pressure taps, unsteady pressure transducers and dynamic pressure-sensitive paint is now analysed using conventional techniques. The first step is to infer flow-field features and the type of flow separation on this wing by analysing

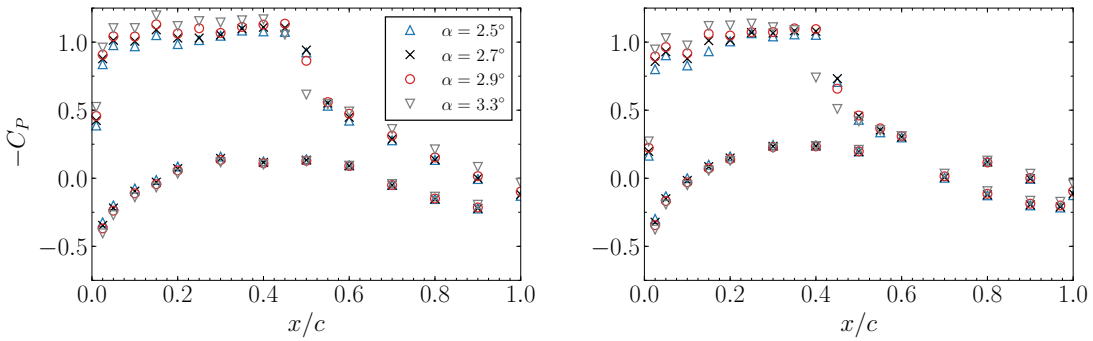

(a) $\eta = 0.73$ **(b)** $\eta = 0.93$

Figure 4.5: Static pressure distributions at two outboard spanwise stations around structural buffeting onset at four angles of attack and $M = 0.80$.

static pressure tap and DPSP data in Section 4.3.1. Insight into the complex shock motion that characterises swept-wing shock buffet is not possible from such time-averaged data and this inherently unsteady phenomenon merits a detailed analysis of dynamic data. In this spirit, the surface pressure unsteadiness is depicted by the standard deviation of the DPSP data in Section 4.3.2 to provide surface-flow visualisation and to link particular flow features with structural buffeting onset. Furthermore, frequency spectra from unsteady pressure transducer data are discussed in Section 4.3.3 highlighting the spectral signature of the shock unsteadiness and the shock-buffet phenomenon.

4.3.1 Time-Averaged Surface Pressure Flow Features

The RBC12 model is equipped with a high number of static-pressure taps which can be used to deduce the surface pressure flow field and the type of flow separation, especially when viewed alongside time-averaged static pressure from DPSP. The following analysis is based on the methodology described in Section 2.1.1. Chordwise pressure distributions at four angles of attack around buffet onset at two spanwise stations on the suction and pressure surfaces are shown in Fig. 4.5. Analysis of the pressure distributions at both $\eta = 0.73$ and 0.93 highlights how suction levels in the supersonic region continue to increase with angle of attack. However, the supersonic region becomes smaller in terms of chordwise extent beyond $\alpha = 2.9°$ as the shock moves forward possibly under the action of a shock-induced separation. Levels of pressure coefficient, C_P, downstream of the shock between $x/c = 0.55$ and 0.60 at $\eta = 0.73$ diverge beyond $\alpha = 2.5°$ suggesting the presence of a shock-induced separation bubble. However, pressure levels farther downstream are approximately the same at $\alpha = 2.5°$ and 2.7° as the flow remains attached. The shock-induced separation bubble merges with the trailing-edge separation beyond $\alpha = 2.9°$ and pressure levels diverge with angle of attack between the shock and the trailing edge. This separated region that forms beyond $\alpha = 2.9°$ is limited in terms of spanwise extent and does not reach the wing tip. This

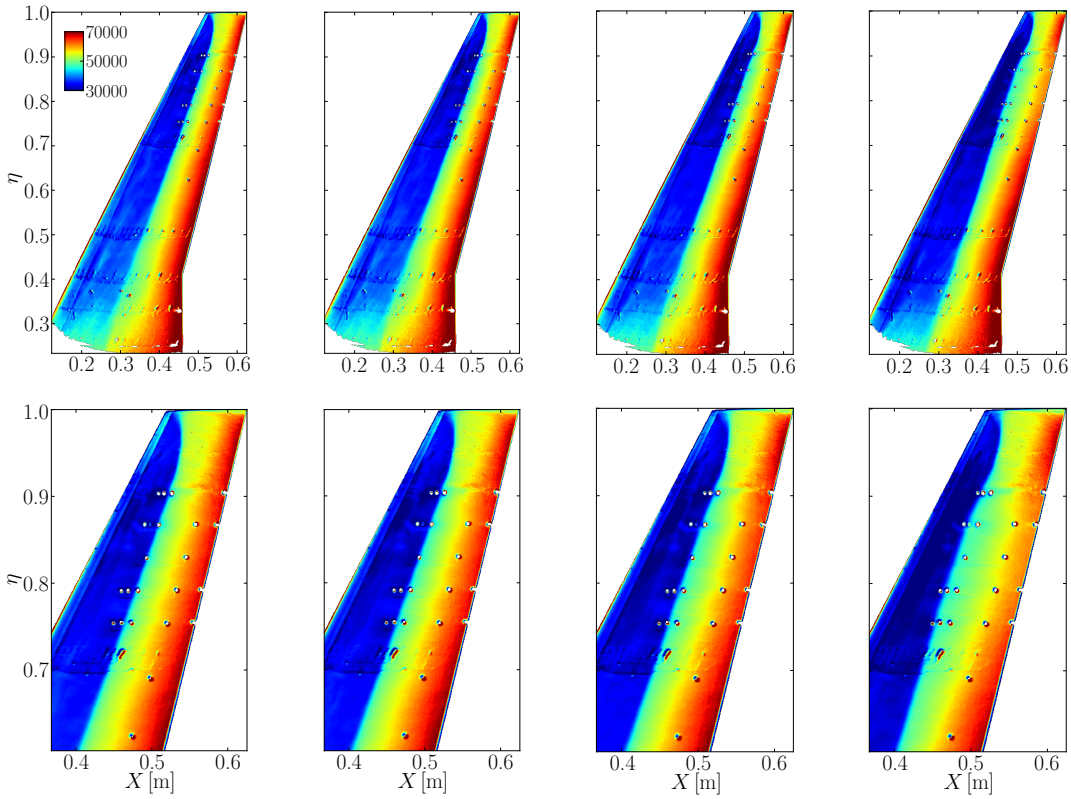

(a) $\alpha = 2.5°$ **(b)** $\alpha = 2.7°$ **(c)** $\alpha = 2.9°$ **(d)** $\alpha = 3.3°$

Figure 4.6: Time-averaged static pressure in pascal on the suction surface from DPSP at $M = 0.80$; overall flow field (top) and magnified outboard section (bottom).

is highlighted by the pressure distribution farther outboard at $\eta = 0.93$ in Fig. 4.5b. Whilst the shock bubble seems more pronounced at higher angle of attack (between $x/c = 0.48$ and 0.60), pressure remains constant with angle of attack at $x/c = 0.60$ and 0.80, contrasting with the distribution at $\eta = 0.73$. This infers that the flow tends to reattach between the shock-induced separation bubble and the trailing edge at $\eta = 0.93$, where the effective angle of attack is lower due to the twisted wing. The twist of the outboard wing at this flow condition is $-0.2°$ (nose down) (Lawson *et al.*, 2016). However, as the angle of attack is further increased to $\alpha = 3.3°$, trailing-edge separation becomes evident.

These observations become more apparent from the time-averaged static pressure fields from DPSP data for the same angles of attack, representing conditions pre and post buffet onset at $M = 0.80$, depicted in Fig. 4.6. The figures at the bottom magnify the outboard region of the wing whereby a close inspection of the shock location, relative to the unsteady pressure transducers (visible as small circles), reveals how the shock starts to move upstream with angle of attack as a locally separated region forms on the outboard section of the wing between $\alpha = 2.7°$ and $2.9°$. This corresponds to the rise in buffeting levels in Fig. 4.3.

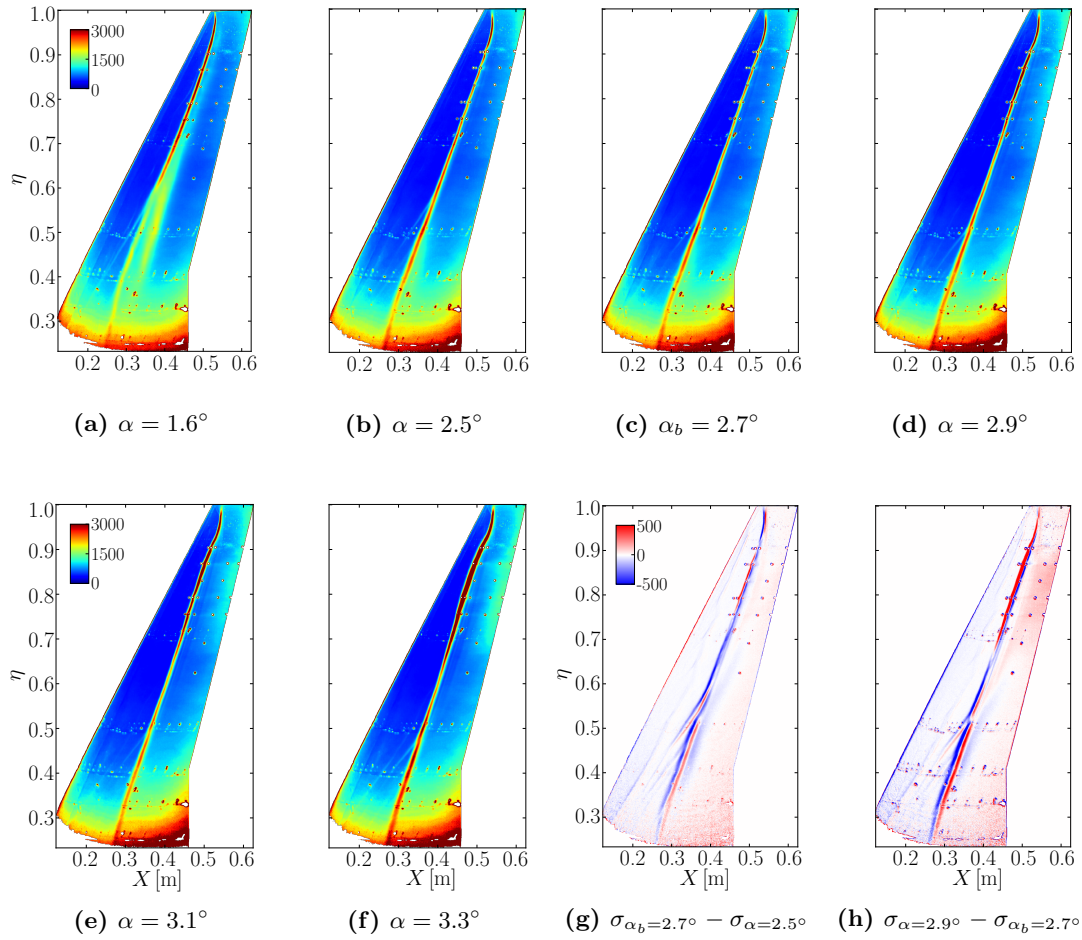

(a) $\alpha = 1.6°$ **(b)** $\alpha = 2.5°$ **(c)** $\alpha_b = 2.7°$ **(d)** $\alpha = 2.9°$

(e) $\alpha = 3.1°$ **(f)** $\alpha = 3.3°$ **(g)** $\sigma_{\alpha_b=2.7°} - \sigma_{\alpha=2.5°}$ **(h)** $\sigma_{\alpha=2.9°} - \sigma_{\alpha_b=2.7°}$

Figure 4.7: Standard deviation (**a**)–(**f**) and relative standard deviation between pairs of α (**g**) and (**h**) of DPSP static pressure in pascal at $M = 0.80$.

4.3.2 Surface Pressure Unsteadiness

A unique aspect of this experimental dataset is the large number of flow conditions with DPSP measurements, whereby its spatio-temporal resolution enables a detailed unsteady analysis that is not limited to discrete points, as is the case otherwise with unsteady transducers. The standard deviation of pressure, σ, was computed on a pixel-by-pixel basis to assess the level of flow unsteadiness. Figures 4.7a through 4.7f present the standard deviation for a number of angles of attack, ranging from well below buffet onset to beyond onset. The highest levels of unsteadiness are confined to the shock foot, which is already unsteady at pre-onset conditions. As the angle of attack is increased, the shock progresses downstream and becomes stronger. The shock-induced separation rapidly extends to the trailing edge at α_b, causing a localised region of separated flow on the outboard section of the wing, visualised by elevated σ values. Consequently, the shock moves upstream and oscillates over larger chordwise extents. It should be noted that the high values of σ inboard of the crank ($\eta < 0.35$) are an artefact of the experimental setup, due to lower illumination levels, and have no physical meaning.

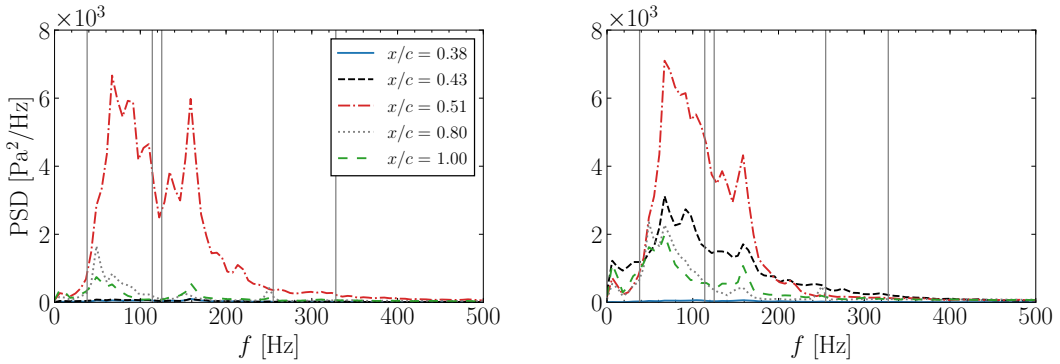

(a) $\alpha_b = 2.7°$ **(b)** $\alpha = 2.9°$

Figure 4.8: Chordwise PSD data at $\eta = 0.80$ for two angles of attack around structural buffeting onset at $M = 0.80$. The vertical lines denote the model's wind-on structural frequencies

The localised separation is more evident from the relative standard deviation between two incidence angles. Figures 4.7g and 4.7h depict how the standard deviation of pressure is changing between selected pairs of incidence angles—the first corresponding to two angles of attack at α_b and just below, the second through the initial rise in buffeting levels. In Fig. 4.7g, there are signs of increased unsteadiness near the trailing edge and the shock starts to move upstream with incidence (the downstream position of the shock is indicated by lower values of σ). Then, in Fig. 4.7h, the separated region on the outboard section of the wing becomes clear and manifests itself as a region of increased σ. Along this spanwise region, the shock has shifted upstream (higher values of σ), whereas farther inboard, where the flow remains attached, the shock moves downstream at the higher angle of attack, resulting in an S-shaped curvature of the shock position from a planform point-of-view. This observation coincides with the increased structural response measured by the strain gauge in Fig. 4.3, as this outboard region yields unsteady surface loads. This rather uncommon analysis using relative standard deviation of surface pressure was selected since it results in a clear visualisation of the separated flow region taking place in the vicinity of structural buffeting onset.

4.3.3 Unsteady Transducer Analysis

The Welch method discussed in Section 2.1.2 is used herein to compute the PSD data of the unsteady signals from both DDAS and DPSP. Specifically, a Hann window is applied to data segments with 50% overlap ($K = M/2$). In the case of data recorded by the DDAS, consisting of ten-second signals sampled at a sampling frequency $f_s = 100\,\text{kHz}$ ($N = 1\,000\,000$), the length of each block, $M = 2^{14} = 16\,384$, gives a frequency resolution (f_s/M) of 6.1 Hz. The PSD estimates used for the cross-spectral analysis in Eq. (2.9) are computed using the Welch method with the same parameters.

The frequency spectra at discrete locations on the wing are analysed in this section. Starting with the chordwise frequency spectra obtained from the unsteady pressure transducers on the suction surface detailed in Fig. 4.1b, Fig. 4.8 shows the PSD data

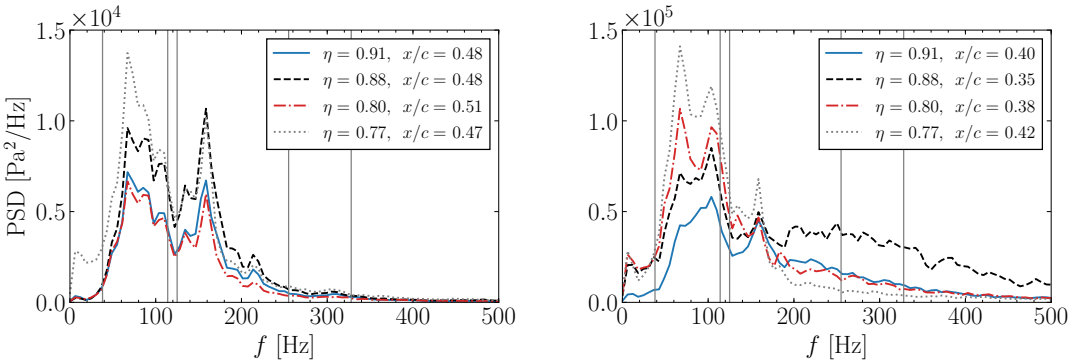

(a) $\alpha_b = 2.7°$ **(b)** $\alpha = 3.3°$

Figure 4.9: Spanwise PSD data approximately along shock for two angles of attack at $M = 0.80$. Note the tenfold increase of PSD values at $\alpha = 3.3°$.

at $\eta = 0.80$ and five chordwise positions around structural buffeting onset, specifically at $\alpha_b = 2.7°$ and $\alpha = 2.9°$. The signal at chordwise station $x/c = 0.51$ has the highest magnitude, indicating close proximity to the shock perturbations, and is characterised by a broadband signature between 50 and 140 Hz ($0.05 \leq St \leq 0.14$). The peak at 160 Hz corresponds to the wind-tunnel fan-passing frequency at this Mach number and is pronounced owing to its periodicity. At $\alpha_b = 2.7°$, the two transducers farthest upstream in the supersonic region give very low levels of unsteadiness. In contrast, both transducers downstream of the shock, at $x/c = 0.80$ and close to the trailing edge, indicate elevated fluctuations. With a slight increase in angle of attack to $\alpha = 2.9°$, these two transducers measure higher energy levels at lower frequencies, centred at a peak of around 70 Hz ($St = 0.07$). The location of these transducers suggests that the the unsteadiness of the shock-induced separation, which extends to the trailing edge at this particular spanwise station, has this characteristic spectral signature. The shock moves upstream with increasing angle of attack (sometimes called inverse shock motion) reaching the transducer at $x/c = 0.43$, which can be provoked by, or provoking, this flow separation which ultimately lowers the effective aerodynamic incidence. The shock loocation is corroborated by the data from static pressure taps presented in Section 4.3.1 and the DPSP standard deviation in Figs. 4.7c and 4.7d. Such unsteadiness centred at low frequency is a recurring observation that is discussed several times herein with particular focus in Chapter 6.

To investigate whether the spectral content of the shock unsteadiness varies with span, the chordwise PSD data were computed at every spanwise station equipped with unsteady transducers, and those showing the highest energy levels were selected as being closest to the shock. The frequency content at buffeting onset is similar between $\eta = 0.77$ and 0.91, as shown in Fig. 4.9a, with the main peak centred around 70 Hz ($St = 0.07$). However, going half a degree above the structural buffeting onset ($\alpha = 3.3°$), the prominent frequency shifts to around 110 Hz at the outboard

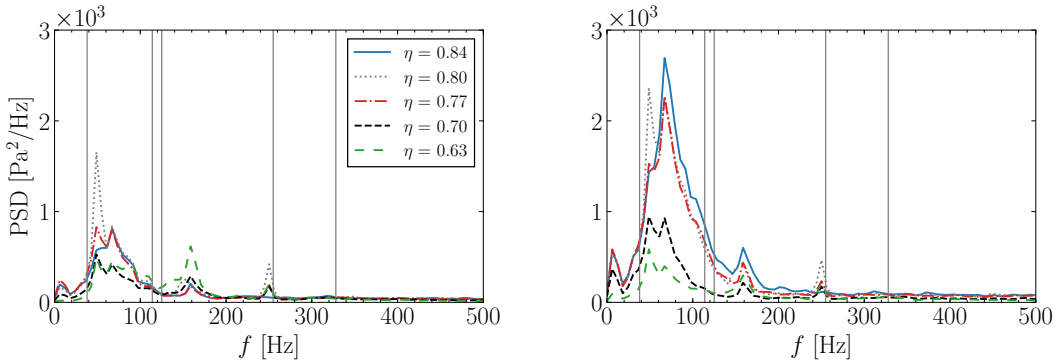

(a) $\alpha_b = 2.7°$ **(b)** $\alpha = 2.9°$

Figure 4.10: Spanwise PSD data downstream of shock at $x/c = 0.80$ around structural buffeting onset at $M = 0.80$.

stations ($\eta = 0.88$ and 0.91), as depicted in Fig. 4.9b (this shift is consistent when varying the block size of the PSD computation). The shock has moved farther upstream at each spanwise station and the PSD levels have increased significantly by an order of magnitude. Furthermore, higher-frequency fluctuations between 200 and 500 Hz ($0.2 \leq St \leq 0.5$) become apparent, especially near the tip, which are in the range of frequencies associated with fully established swept-wing shock buffet (Koike *et al.*, 2016; Dandois, 2016; Sugioka *et al.*, 2018).

When quoting Strouhal numbers for such a tapered wing, care should be taken due to the large variation in the local chord length along the span. While MAC (0.2789 m) is a useful reference length, the local chord varies between $c = 0.173$ m and 0.126 m for spanwise stations between $\eta = 0.77$ and 0.91, with the latter value being less than half the MAC. Consequently, the shift of the prominent peak from 70 Hz to 110 Hz within the shock-unsteadiness bump at $\alpha = 3.3°$ results in the same local Strouhal number of 0.05 at each respective station. Although this value is typically associated with aerofoil buffet, the mechanism for the shock unsteadiness on wings is not merely an acoustic feedback mechanism governed by the chordwise distance to the trailing edge, since the shock unsteadiness has a similar signature along the span for the range of flow conditions analysed. The mean shock position is a function of angle of attack (amongst other parameters), and hence, the chordwise distance between the shock foot and the trailing edge is changing with angle of attack. Possible sources for the shock-unsteadiness bump centred at $St = 0.07$ are discussed in Chapter 6.

Having analysed the frequency content along the shock, Fig. 4.10 focuses farther downstream and shows the PSD data at 80% local chord between $\eta = 0.63$ and 0.84 around the onset of structural buffeting, specifically at $\alpha_b = 2.7°$ and $\alpha = 2.9°$. The transducers located at the outboard sections between $\eta = 0.77$ and 0.84 have higher energy levels at $\alpha = 2.9°$ with broadband spectral content centred around 70 Hz. These three transducers are located within the localised separation region indicated by ele-

vated relative standard deviation between $\alpha_b = 2.7°$ and $\alpha = 2.9°$ in Fig. 4.7h. In contrast, the spectra farther inboard at $\eta = 0.70$ and 0.63 are similar for both angles of attack, as corroborated by Fig. 4.7h, whereby these transducers are located in areas with almost zero relative σ. This implies that the increased buffeting level registered by the strain gauge at $\alpha = 2.9°$, shown in Fig. 4.3, can be attributed to the shock-induced separated region located on the outboard section of the wing and consequent shock oscillation. Surface pressure fluctuations in this region at onset have frequencies corresponding to the shock-unsteadiness bump. Recall that the peak at 160 Hz is the wind-tunnel fan-passing frequency while the peaks at 50 and 250 Hz are related to the power supply, the latter becoming only visible at low PSD levels.

These observations highlight the existence of distinct phenomena across particular frequency bands. First, low-frequency shock unsteadiness centred at $St = 0.07$, based on MAC, is present throughout the range of flow conditions analysed. Reaching buffeting onset, the stronger shock causes the shock-induced separation to merge with the trailing-edge separation between particular spanwise stations confined outboard, such that a broader unsteady region exhibits more intense fluctuations. Second, with a further increase in angle of attack, higher-frequency oscillations between $0.2 \leq St \leq 0.5$, attributed to the shock-buffet phenomenon, become more dominant near the wing tip.

4.4 Data-Based Modal Analysis

The main advantage of modal analysis techniques is their ability to provide a spatio-temporal representation of the flow dynamics. Therefore, the DPSP data is now analysed using data-based modal analysis techniques including POD and DMD. The standard deviation analysis in Section 4.3.2 was limited to the visualisation of the overall level of unsteadiness and did not provide information regarding its time history or frequency content. Whilst the latter was provided by the unsteady transducers in Section 4.3.3, this was restricted to discrete locations. Instead, the modal analysis extends this over almost the entire wing. First, the POD analysis in Section 4.4.1 clarifies the spatio-temporal nature of the three-dimensional shock structure and its motion along the span. Second, the DMD analysis in Section 4.4.2, in addition to corroborating previous observations, clearly isolates the two key flow phenomena put forward herein.

4.4.1 Proper Orthogonal Decomposition

Proper orthogonal decomposition was applied to the mean-subtracted DPSP pressure snapshots to extract the dominant flow features. A large number of snapshots, $m = 10\,000$, comprising 5 s of flow at $M = 0.80$ (captured at 2000 fps) and 2.5 s for the other Mach numbers (captured at 4000 fps), were used such that the principal dynamics are well-resolved in time. A total of 20 000 snapshots are available for each flow condition,

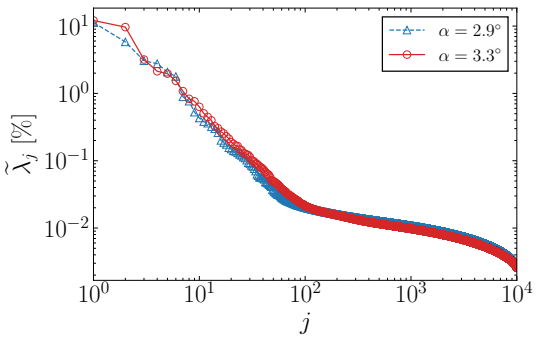

Figure 4.11: Energy distribution of POD modes at $M = 0.80$.

however, setting $m = 10\,000$ was deemed sufficient after investigating the impact of sample size. Using the first 10 000 snapshots, the second 10 000 or all 20 000 gave the same modes suggesting statistical convergence. In contrast, different sets of 1000 snapshots each resulted in a dominant mode with contributions from both the structural response of the model and the shock unsteadiness, rather than well-defined modes that result from 10 000 snapshots. The frequency spectra corresponding to the temporal component of the POD modes were calculated using the Welch method. The signal from the DPSP data consists of $N = 10\,000$ samples and the length of each block is either 500 or 1000, depending on the frame rate (either 2000 or 4000 fps), resulting in a frequency resolution of 4 Hz.

Around the onset of structural buffeting, dominant POD modes are related to either the structural response of the model, discussed first, or the shock unsteadiness along the span, discussed second. Image alignment accounting for small model and camera movements during pre-processing yields a registration error with strong gradients around the surface features, such as model edges and instrumentation. Since it is present in all images, this is extracted as a strong energetic feature and consequently appears as the model structural response in the first or second POD mode (Crafton *et al.*, 2017). Other dominant modes capture the shock unsteadiness, being the main aerodynamic feature with large static pressure gradients over extensive spatial areas. This is a travelling structure and is hence found in several modes. Furthermore, less dominant, higher-order modes are related to smaller-scale perturbations within the shock region and fluctuations in the flow downstream. Typically, from a set of 10 000 modes, tens are related to these features. However, such flow features have a small contribution to the overall flow field since the POD energy rapidly decays after the first few dominant modes. Moreover, thousands of lower energy modes increasingly become contaminated by incoherent camera noise and show no obvious relation to the aerodynamics. This can be seen in Fig. 4.11 which depicts the POD energy distribution at $M = 0.80$ and two angles of attack. The change in slope after approximately 100 modes corresponds to the onset of modes with incoherent noise.

Table 4.3: Eigenvalue contribution of eight POD modes at $M = 0.80$ and two angles of attack.

$\alpha = 2.9°$			$\alpha = 3.3°$		
j	$\widetilde{\lambda}_j$ (%)	$\sum_{k=1}^{j} \widetilde{\lambda}_k$ (%)	j	$\widetilde{\lambda}_j$ (%)	$\sum_{k=1}^{j} \widetilde{\lambda}_k$ (%)
1	11.3	11.3	1	12.1	12.1
2	5.8	17.1	3	3.2	25.0
3	3.1	20.2	4	2.1	27.7
4	2.8	23.0	7	1.1	31.7
5	2.1	25.0	8	0.8	32.5
6	1.8	26.8	9	0.8	33.3
7	0.9	27.8	11	0.5	34.4
8	0.8	28.5	13	0.4	35.5

Dominant POD modes obtained at $\alpha = 2.9°$ are shown in Fig. 4.12, depicting the spatial amplitudes representing fluctuations around the mean pressure, while the relative contributions of the eigenvalues are given in Table 4.3 and depicted in Fig. 4.11. These were normalised by their sum, representing their relative energy

$$\widetilde{\lambda}_j = \frac{\lambda_j}{\sum_{k=1}^{m} \lambda_k}. \tag{4.2}$$

The spatial amplitudes are dimensionless and to get reconstructed pressure based on specific modes, the modes are multiplied by the eigenvalues λ_j and the expansion coefficients $a_{i,j}$.

Considering the first eight modes, modes 1, 3, 6 and 8 are dominated by the structural response while the other modes capture the shock unsteadiness, as confirmed from the PSD of the temporal coefficients, presented in Fig. 4.13. Modes related to the structural response have peaks at the first wing-bending frequency and other wind-on structural modes summarised in Chapter 3. Such wind-on frequencies will vary to some extent due to the coupling between the fluid and the structure to give aeroelastic modes, which were found to be similar to those at wind-off condition. The lower-frequency peak at 20 Hz is present in modes showing contribution at the leading and trailing edges of the model and is possibly related to wind-tunnel wall vibration, to which the cameras are mounted. Lower-frequency behaviour at 10 Hz might be induced by wind-tunnel unsteadiness but there is presently no complete understanding of the exact source. Finite element analysis of the full wind tunnel is out of scope herein and is suggested as future work to confirm these low frequencies. Modes 2 and 4, in Figs. 4.12b and 4.12d, have the greatest contribution along the shock wave hinting at the shock unsteadiness, whilst the spatial amplitudes of mode 2 invert sign at around $\eta = 0.65$. This is reminiscent of the relative standard deviation around buffeting onset, shown in Fig. 4.7h, and

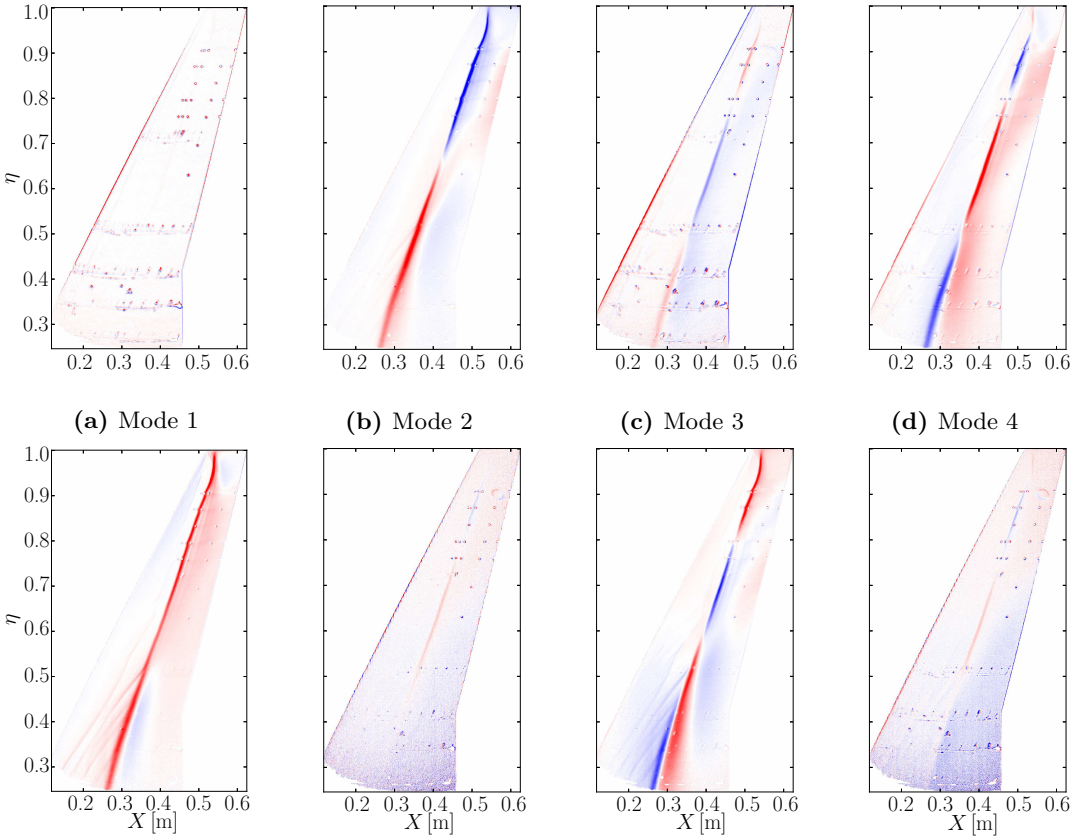

(a) Mode 1 **(b)** Mode 2 **(c)** Mode 3 **(d)** Mode 4

(e) Mode 5 **(f)** Mode 6 **(g)** Mode 7 **(h)** Mode 8

Figure 4.12: Spatial component of first eight POD modes at $M = 0.80$ and $\alpha = 2.9°$. The spatial amplitudes are coloured from blue to red, representing opposite signs (-0.01 to 0.01).

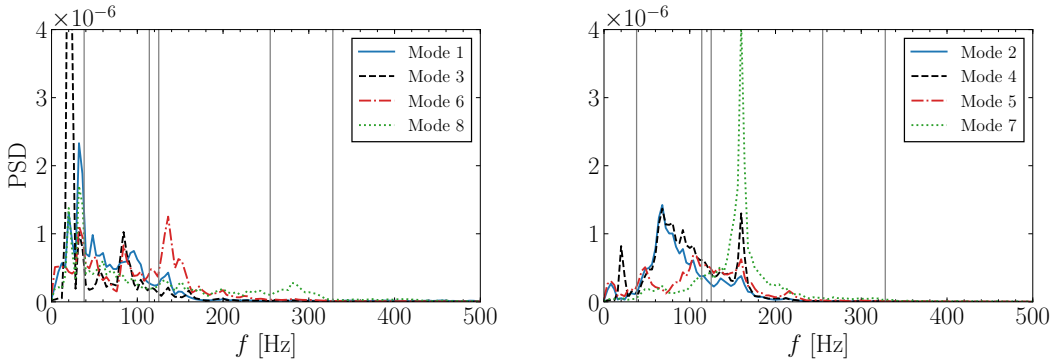

(a) Structure dominated modes **(b)** Shock unsteadiness modes

Figure 4.13: PSD of temporal coefficients for the first eight POD modes at $M = 0.80$ and $\alpha = 2.9°$ shown in Fig. 4.12.

corroborates the flow physics described in Section 4.3.2. An instantaneous pressure snapshot based on this mode, when scaled by a negative temporal coefficient, has a positive pressure fluctuation between $\eta = 0.65$ and the wing tip (i.e. the shock is upstream of its mean location), accompanied by a lower pressure near the trailing edge,

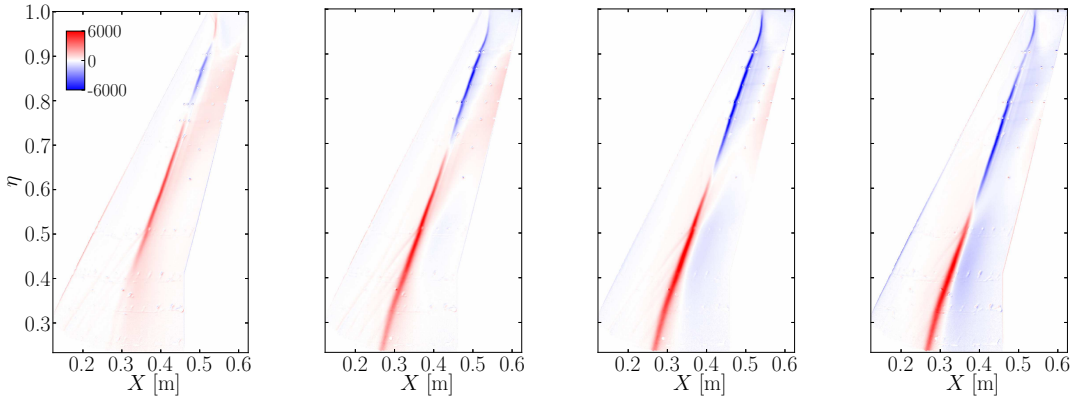

(a) POD reconstructed snapshots using modes 2, 4 and 5

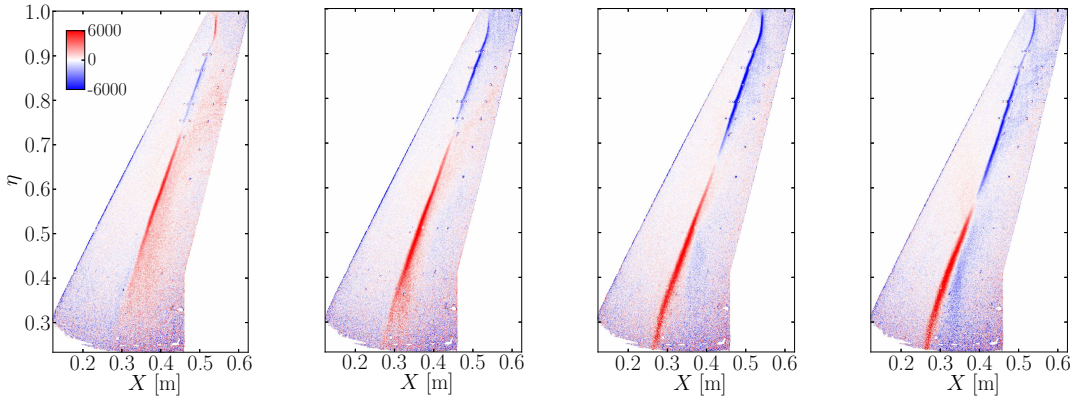

(b) Original snapshots from DPSP

Figure 4.14: Instantaneous snapshots at $M = 0.80$ and $\alpha = 2.9°$, starting from $t = 0.0175\,\mathrm{s}$ in steps of $\Delta t = 0.0015\,\mathrm{s}$, coloured by static pressure deviation from mean, in pascal.

indicative of shock-induced rear separation. Farther inboard, the shock is downstream of its mean position and the flow remains attached. The opposite can be said for a positive temporal coefficient, that is, the shock is downstream outboard and upstream inboard. Hence, such a mode represents an S-shaped spanwise shock curvature that exhibits broadband, low-frequency oscillations, peaking at around 70 Hz, depicted in Fig. 4.13b. Mode 5 in Fig. 4.12e represents particular instances where the shock either sits at its forwardmost or aftmost positions along the whole span. Higher spatial amplitudes near the wing tip, together with a shift to higher-frequency content centred at 110 Hz in Fig. 4.13b, support the unsteady transducer analysis at a post-onset flow condition in Section 4.3.3. Figure 4.12g depicting mode 7 shows a pressure disturbance along the shock and over the entire wing. The corresponding prominent peak at 160 Hz corresponds to the wind-tunnel fan-passing frequency.

The physical contribution of aerodynamically-relevant POD modes can be visualised by reconstructing the surface pressure using specific modes and their corresponding eigenvalues and temporal coefficients, in this case, modes 2, 4 and 5—the three dominant modes correlated to the shock unsteadiness. Figure 4.14 shows a sequence of

instantaneous snapshots starting at $t = 0.0175\,\mathrm{s}$, both reconstructed flow field and original snapshots, coloured by the pressure deviation from the mean flow. Initially, in the first image, the shock sits downstream of its mean position between $\eta = 0.75$ and 0.90. This outboard perturbation propagates both towards the tip and the root, while the location where the shock curves between its upstream and downstream positions continues to move inboard. As the shock adopts a downstream position, a localised region of lower pressure simultaneously propagates downstream towards the trailing edge. By the end of the sequence, the outboard shock is moving upstream and is close to its mean position. This results in a higher relative velocity with respect to the freestream and subsequent snapshots, not shown in the figure, depict a locally strengthened shock that causes rear separation and a shock-induced separation bubble which convects downstream and merges at the trailing edge. This latter part of the sequence can be seen in a movie available with the published online material[1] of Masini *et al.* (2020). Repeatedly, the flow separates and reattaches over the outboard portion of the wing, locally resulting in shock perturbations which propagate both inboard and outboard at this angle of attack, just above structural buffeting onset.

Increasing the angle of attack to $\alpha = 3.3°$, dominant POD modes capture the characteristic low-frequency shock unsteadiness along the span, the structural response, and smaller-scale perturbations confined to the outboard region, attributed to the shock-buffet instability. Figure 4.15 depicts the spatial component of predominantly aerodynamic modes, excluding modes capturing the structural response. The relative contributions of the eigenvalues are presented in Table 4.3 and shown in Fig. 4.11 while PSD data of the temporal coefficients are depicted in Fig. 4.16. The shock, positioned farther upstream and undergoing larger excursions, is evident from a comparison of modes that capture the spanwise shock unsteadiness at both $\alpha = 2.9°$ and $3.3°$, specifically Figs. 4.12b, 4.12d, 4.12e, 4.12g and Figs. 4.15a through 4.15d. It should be noted that more intense fluctuations related to the S-shaped shock curvature at $\alpha = 3.3°$ shift to mode 1, becoming the dominant feature instead of the structural response. Moreover, modes with high spatial amplitudes in the outboard region, such as modes 7, 8, 11 and 13, temporally show broadband, higher-frequency behaviour, above 200 Hz, as depicted in Fig. 4.16. This corroborates the unsteady transducer analysis discussed in Section 4.3.3, whereby PSD data at $\alpha = 3.3°$ in Fig. 4.9b highlighted fluctuations above 200 Hz, which are not evident at $\alpha = 2.9°$. These observations support the idea of coexisting phenomena beyond shock-buffet onset conditions; namely, low-frequency shock unsteadiness along the whole span centred at 70 Hz together with higher-frequency oscillations above 200 Hz on the outboard wing.

The higher-frequency oscillations, which have an outboard-running behaviour, are clear from instantaneous pressure snapshots, depicted in Fig. 4.17, both from a POD reconstruction using solely the modes shown in Fig. 4.15 and the original data. The

[1] Available at `https://doi.org/10.1017/jfm.2019.906`.

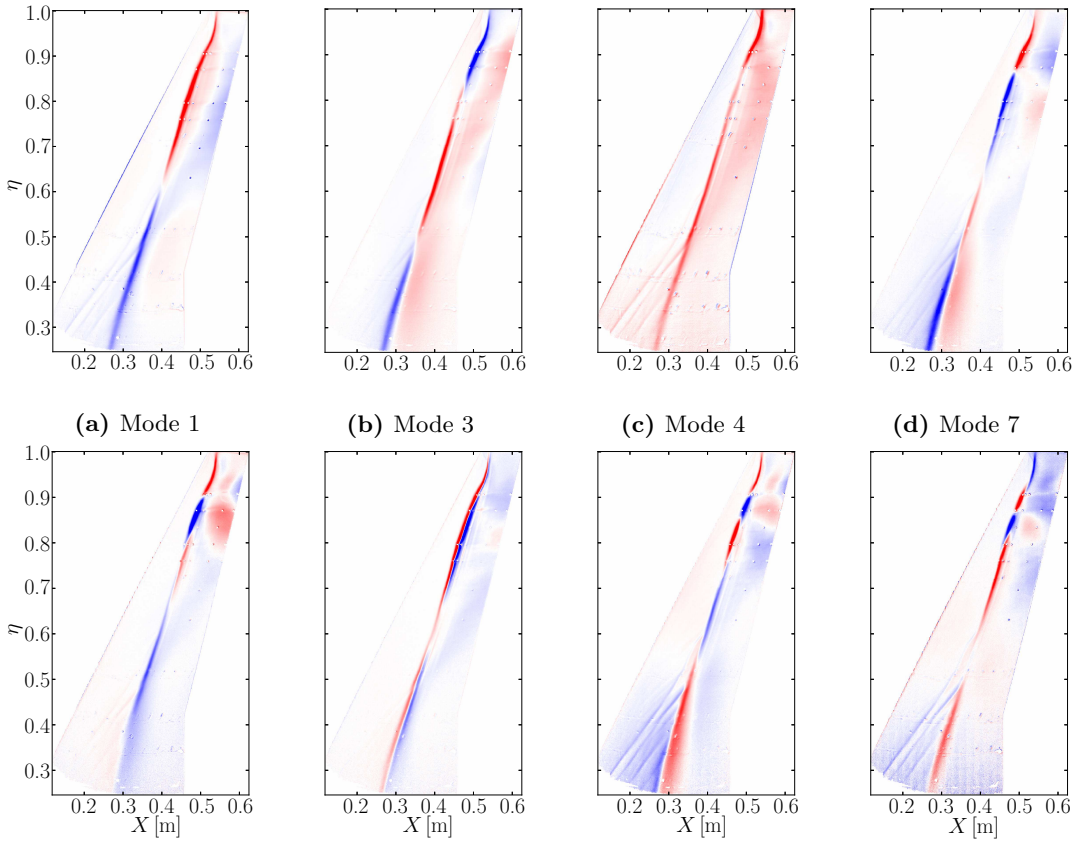

(a) Mode 1 **(b)** Mode 3 **(c)** Mode 4 **(d)** Mode 7

(e) Mode 8 **(f)** Mode 9 **(g)** Mode 11 **(h)** Mode 13

Figure 4.15: Spatial component of dominant POD modes at $M = 0.80$ and $\alpha = 3.3°$ capturing low-frequency shock unsteadiness and shock buffet. The spatial amplitudes are coloured as in Fig. 4.12. Structure-dominated modes are not shown.

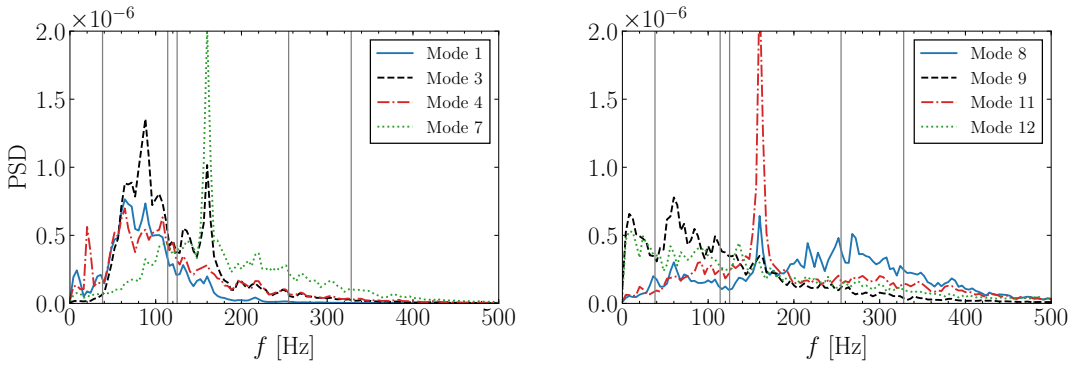

Figure 4.16: PSD of temporal coefficients of selected POD modes at $M = 0.80$ and $\alpha = 3.3°$.

upstream shock perturbation between $\eta = 0.75$ and 0.90 at $t = 0.045\,\mathrm{s}$, characterised by a positive pressure deviation, propagates towards the wing tip in the successive snapshots, each separated by $\Delta t = 0.0005\,\mathrm{s}$. This smaller time step, compared to Fig. 4.14, highlights the higher-frequency behaviour of these outboard-running disturbances. Additionally, the lower-frequency, inboard-running wave elicited at $\alpha = 2.9°$ can also be

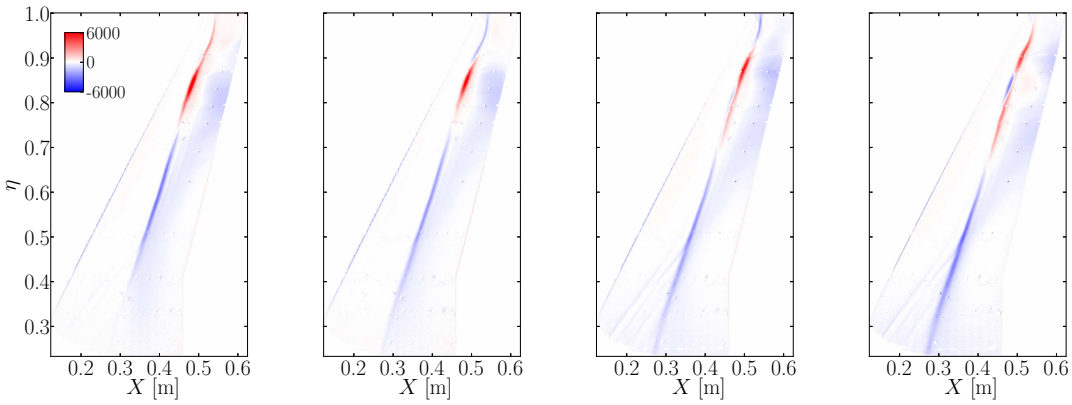

(a) POD reconstructed snapshots using modes 1, 3, 4, 7, 8, 9, 11 and 13

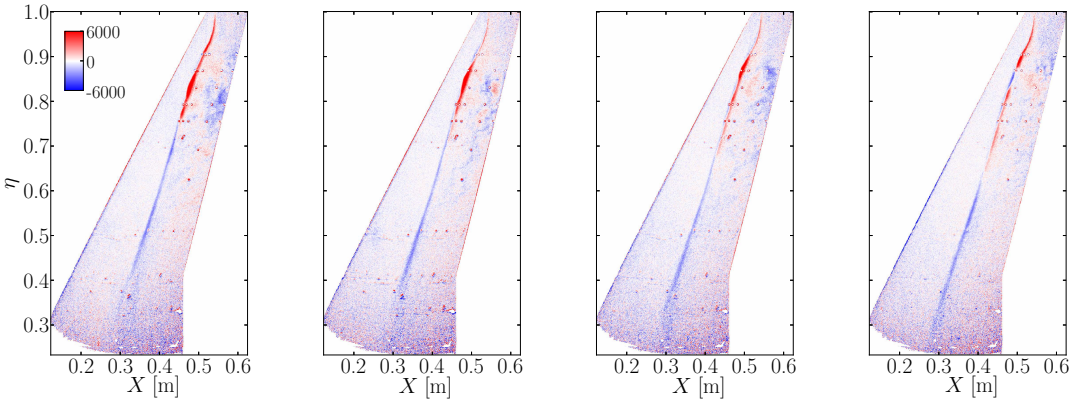

(b) Original snapshots from DPSP

Figure 4.17: Instantaneous snapshots at $M = 0.80$ and $\alpha = 3.3°$, starting from $t = 0.045\,\mathrm{s}$ in steps of $\Delta t = 0.0005\,\mathrm{s}$, coloured by static pressure deviation from mean, in pascal.

observed at $\alpha = 3.3°$, simultaneously travelling towards the root. The location where the shock curves from its upstream to downstream position moves from $\eta = 0.75$ in the first snapshot to $\eta = 0.63$ in the last snapshot of the sequence. The reader is referred to the published online material[2].

4.4.2 Dynamic Mode Decomposition

DMD was applied to the DPSP snapshots to extract dynamic information from surface pressure data and to isolate the flow phenomena based on frequency. The results presented are based on 1000 snapshots, comprising 0.5 s of flow data at $M = 0.80$ and $\alpha = 3.3°$. The analysis was repeated using different sets of 1000 snapshots in time and using 10 000 snapshots, giving resulting modes within the same frequency range that look similar when visualised. More importantly, resulting modes, both for the shock unsteadiness at lower frequencies and for swept-wing shock buffet at higher frequencies, corroborate the distinct flow phenomena highlighted previously.

[2]Available at `https://doi.org/10.1017/jfm.2019.906`.

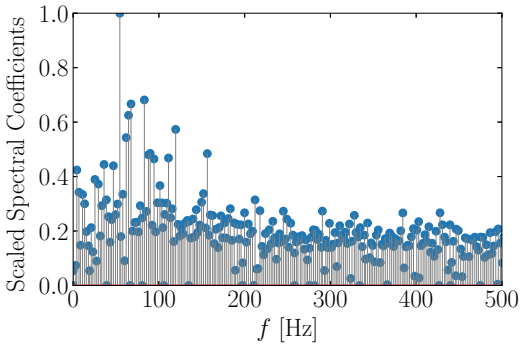

Figure 4.18: DMD spectrum at $M = 0.80$ and $\alpha = 3.3°$.

The computed DMD spectrum is shown in Fig. 4.18. Herein, the spectral coefficients have been computed as the norm of the first projection coefficient (see Eq. (2.21)), analytically equivalent to the least-squares projection of the first snapshot onto a projected DMD mode (Tu *et al.*, 2014). The spectral coefficients are scaled by the DMD eigenvalues, such that the scaled spectral coefficients in Fig. 4.18 are equal to $|d_{1,j}| \cdot |\mu_j|^{m-1}$ and have been normalised with the maximum value (excluding the mean flow mode). This scaling promotes growing and slowly-decaying modes, while reducing the peaks of modes with large norms but of a quickly-decaying nature (Tu *et al.*, 2014). Dominant modes within the low-frequency shock-unsteadiness range are identified, together with a number of modes within the shock-buffet range, such that the DMD spectrum is reminiscent of the PSD data computed from unsteady transducers, shown in Fig. 4.9b.

The DMD mode with the highest spectral peak has a frequency of 54 Hz. Its spatial structure has a small contribution to the shock unsteadiness but is dominated by the structural response. The mode oscillating at 83 Hz has the second highest spectral peak and is depicted in Fig. 4.19. Each DMD mode is a complex-valued spatial field scaled to unit norm, and the spatial amplitudes of both real and imaginary parts are shown. Furthermore, their magnitude and phase angle at each spatial point are also presented. Significant perturbations along the shock, the shock-induced separation bubble, and trailing-edge separation on the outboard wing are visible. The S-shaped shock curvature resulting from the reversed-flow region on the outboard wing, which possibly pushes the shock upstream, closely resembles the dominant POD mode at the same flow condition, shown previously in Fig. 4.15a. Furthermore, variations between the real and imaginary parts of DMD modes encode information regarding the propagation of pressure perturbations. The magnitude of the complex number in Fig. 4.19c highlights the shock-dominated low-frequency dynamics, with the strongest perturbations occurring upstream of the localised separated region. Spanwise pressure propagation along the shock becomes clear from the phase contours in Fig. 4.19d. Apparent discontinuities are due to phase wrapping and are unphysical. The phase variation along the shock reveals a pressure propagation that simultaneously travels in the inboard and

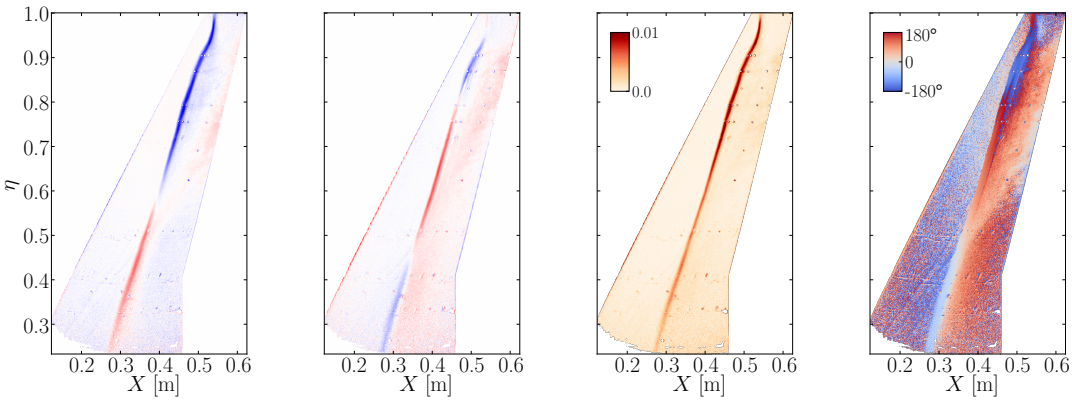

(a) Real part **(b)** Imaginary part **(c)** Magnitude **(d)** Phase angle

Figure 4.19: DMD mode at 83 Hz; the spatial amplitudes in (a) and (b) are coloured from blue to red, representing opposite signs (−0.01 to 0.01).

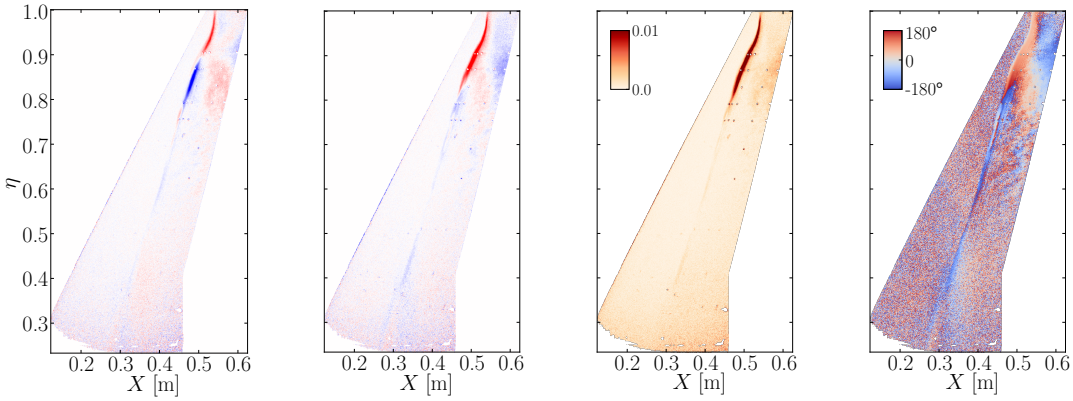

(a) Real part **(b)** Imaginary part **(c)** Magnitude **(d)** Phase angle

Figure 4.20: DMD mode at 245 Hz; the spatial amplitudes are coloured as in Fig. 4.19.

outboard directions, reversing its path close to the wing tip at $\eta = 0.87$, consistent with the discussion in Chapter 6. Considering the streamwise propagation of pressure, the trailing edge separation on the outboard wing has an opposite phase to the shock foot (a phase difference of around π). This implies that an upstream shock movement is accompanied by a decrease in pressure at the trailing edge, and vice versa, corroborating the flow physics inferred from the POD spatial amplitudes, with opposite signs between the shock foot and the trailing edge, in Fig. 4.15a.

The broadband nature of swept-wing shock buffet yields a relatively continuous distribution of modes in Fig. 4.18. A similar DMD spectrum has been reported for broadband low-frequency unsteadiness in supersonic SWBLI (Priebe *et al.*, 2016). Although there are no particularly dominant spectral peaks within the higher-frequency range ($0.2 \leq St \leq 0.5$) in Fig. 4.18, visualisation of these DMD modes reveals the highest contribution along the outboard shock and the separated flow structures convecting downstream. Figure 4.20 illustrates a DMD mode oscillating at 245 Hz with a relatively

high spectral coefficient, when compared to modes within this frequency range. The spatial amplitudes and magnitude in Figs. 4.20a through 4.20c highlight perturbations confined to the tip region, corresponding to the higher-frequency outboard-running behaviour. This outboard propagation of pressure towards the wing tip is confirmed from the phase contours in Fig. 4.20d, with the phase gradually decreasing along the shock foot towards the tip.

It should be emphasised that in order to get an accurate reconstruction of the shock dynamics, several DMD modes should be included, in line with the broadband nature of the problem. The aim of this section is to isolate the distinct flow phenomena on the upper wing surface beyond shock-buffet onset conditions—the predominantly inboard-running low-frequency shock-unsteadiness behaviour almost along the whole span and the higher-frequency, outboard-running behaviour confined to the tip region. These contrasting characteristics were confirmed from time-resolved snapshots based solely on the modes presented in Figs. 4.19 and 4.20. Movies of these reconstructions are available with the online published material[3].

4.5 Influence of Vane Vortex Generators

The influence of the configurations with the sparse and full vortex-generator arrays described in Section 4.1.3 is now studied. The aim is to clarify the influence of passive flow control on shock-buffet onset. The role of the vortex generators in delaying the onset of this instability is elucidated via unsteady transducer and DPSP data. This is limited to the design Mach number aiding comparison with the uncontrolled case.

The surface pressure unsteadiness for the sparse and full VG configurations is visualised in Fig. 4.21 from the standard deviation of the DPSP data at four angles of attack starting from the buffet-onset incidence. It should be noted that the full VG configuration was first tested, followed by the sparse array. Some VGs were removed for the latter and for this reason, some spots at all VG locations can still be seen from the DPSP data. This is just an experimentation artefact and is not physical. The first observation is that the shock sits further downstream at the higher buffet-onset incidence when compared to the clean wing. This is expected since the vortices created by the VGs promote more mixing with the outer flow rendering the boundary layer less prone to separation, in turn delaying the onset of inverse shock motion. Moreover, the chordwise extent of the shock unsteadiness is smaller and the standard deviation along the shock has lower magnitude downstream of the VGs. These observations become more evident in Fig. 4.22 which magnifies the outboard section for the three configurations at $\alpha = 3.3°$. Although inverse shock motion takes place beyond buffet onset in all configurations, as a result of the mutual interaction between the shock and the localised flow separation on the outer wing, there are clear differences in the flow topology. The

[3]Available at `https://doi.org/10.1017/jfm.2019.906`.

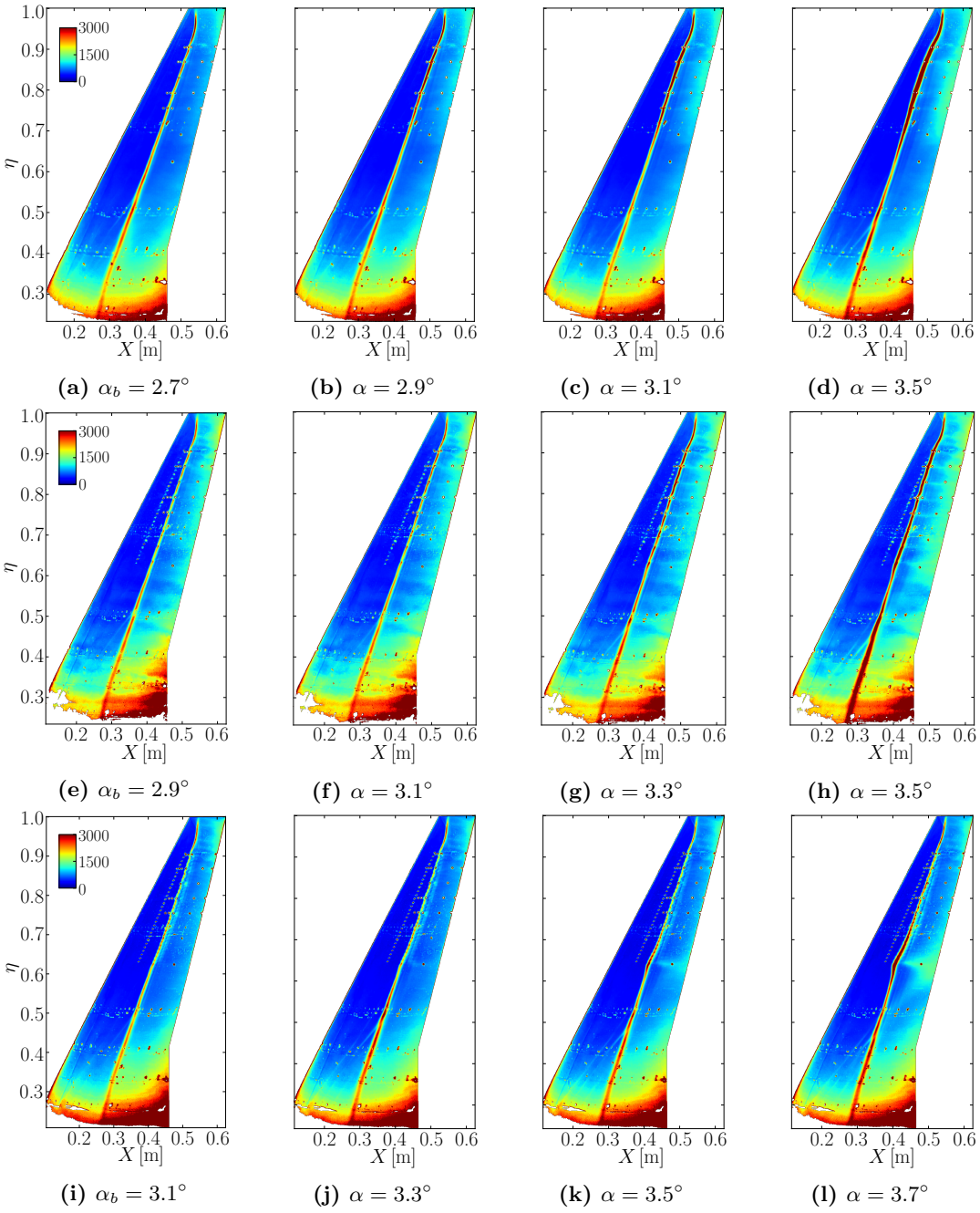

(a) $\alpha_b = 2.7°$ **(b)** $\alpha = 2.9°$ **(c)** $\alpha = 3.1°$ **(d)** $\alpha = 3.5°$

(e) $\alpha_b = 2.9°$ **(f)** $\alpha = 3.1°$ **(g)** $\alpha = 3.3°$ **(h)** $\alpha = 3.5°$

(i) $\alpha_b = 3.1°$ **(j)** $\alpha = 3.3°$ **(k)** $\alpha = 3.5°$ **(l)** $\alpha = 3.7°$

Figure 4.21: Standard deviation of DPSP static pressure in pascal at $M = 0.80$ for the clean wing (top), sparse (middle) and full VG (bottom) configurations. Some of the clean wing data are reproduced from Fig. 4.7 for convenience.

flow topology for the clean wing and the sparse VG array is similar, characterised by a separated flow region between $\eta = 0.65$ and 0.90 together with an upstream movement of the shock which undergoes larger oscillations. However, a different pattern results for the full VG array, whereby the upstream shock motion with angle of attack is more gradual on the outer wing and the shock unsweeps distinctively just downstream of

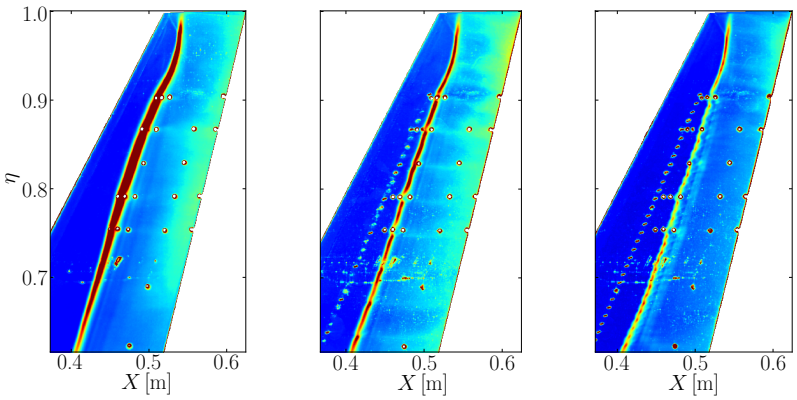

(a) Clean wing **(b)** Sparse VG **(c)** Full VG

Figure 4.22: Magnified view of the standard deviation of DPSP static pressure on the outer wing at $\alpha = 3.3°$ and $M = 0.80$.

the most inboard VG at $\eta = 0.63$. This generates an intense flow separation and the spanwise region downstream is characterised by relatively higher standard deviation values, as highlighted in Figs. 4.21k and 4.21l. Interestingly, the larger number of vortices generated by the full array create evident corrugation along the shock foot. A similar wavy pattern along the shock was also observed from oil-flow visualisations on the NASA Common Research Model at similar flow conditions (Koike *et al.*, 2015).

The analysis of the unsteady pressure transducer signals corroborates the observations from the DPSP standard deviation. The RMS of the signals from the five unsteady pressure transducers at $\eta = 0.80$ is presented in Fig. 4.23 for the three configurations at four angles of attack starting from α_b. The shock location can be traced from high RMS levels. Considering the clean wing data in Fig. 4.23a, the shock moves upstream with incidence and reaches the transducer at $x/c = 0.43$ and $\alpha = 3.1°$. This trend continues with increasing angle of attack and the shock reaches $x/c = 0.38$ at $\alpha = 3.3°$. The shock exhibits broad chordwise oscillations since both transducers at $x/c = 0.38$ and 0.43 register high RMS levels. In contrast, the shock sits farther downstream at the same angle of attack when the VGs are installed. This implies that shock-induced separation, inverse shock motion and buffet onset are all delayed, as depicted previously in Fig. 4.22. For the full VG configuration, RMS levels at $x/c = 0.38$ remain very low as the shock does not reach this transducer even at $\alpha = 3.7°$. Moreover, the unsteadiness is lower with the VGs installed over the whole range of flow conditions presented in Fig. 4.23 confirming that pressure fluctuations mainly driven by the shock oscillations are being attenuated. Furthermore, the RMS levels close to the trailing edge increase steadily with angle of attack throughout, as a result of higher unsteadiness associated with separated flow beyond the buffet-onset incidence.

The analysis of the frequency spectra of controlled cases reveals a similar spectral signature when compared to the clean wing in shock-buffet conditions. Power spectral

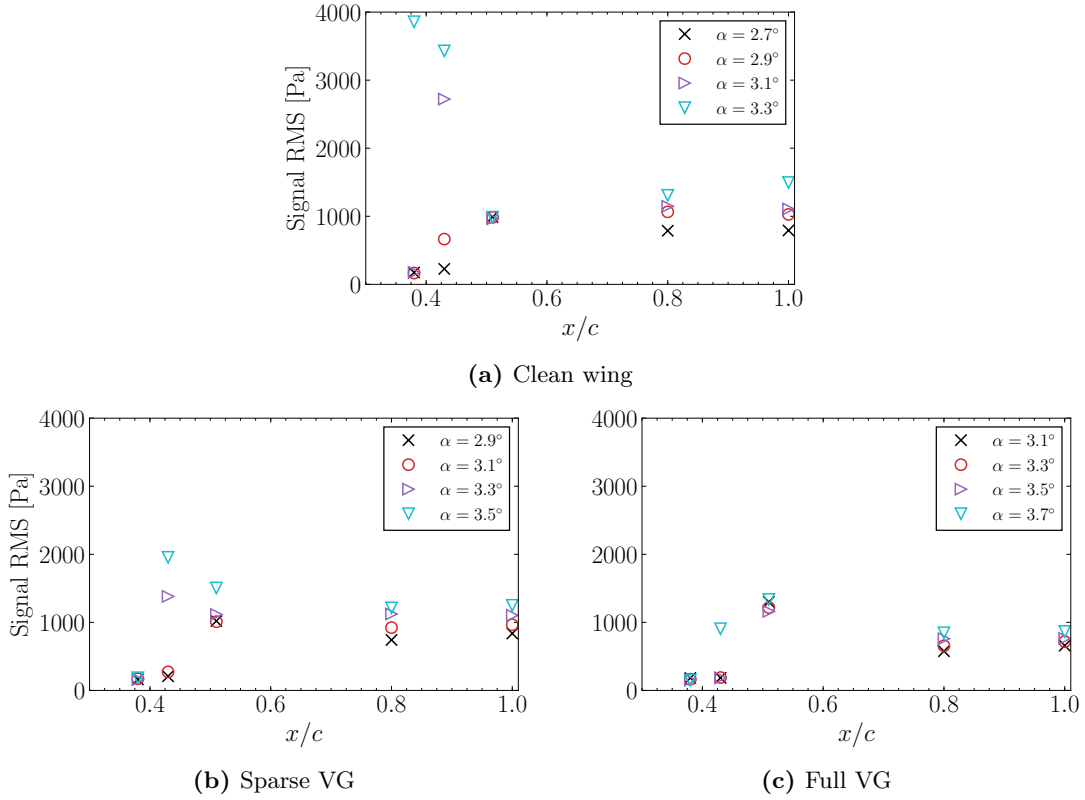

(a) Clean wing

(b) Sparse VG

(c) Full VG

Figure 4.23: Chordwise unsteady transducer RMS levels at $\eta = 0.80$ with increasing angle of attack from buffet onset at $M = 0.80$.

density data from the transducers closest to the shock at four spanwise stations between $\eta = 0.77$ and 0.91 are depicted in Fig. 4.24. The flow conditions correspond to buffet onset and 0.6° beyond onset. All spectra are characterised by low-frequency content centred around 70 Hz ($St = 0.07$). Even though the PSD levels increase with angle of attack as a result of more energetic shock oscillations, the PSD levels in Figs. 4.24d and 4.24f are lower than those recorded for the clean wing at 0.6° above onset in Fig. 4.24b. Moreover, higher-frequency content between 200 and 500 Hz, apparent near the wing tip for the uncontrolled case at $\alpha = 3.3°$, seems to be suppressed by passive flow control.

4.6 Summary of Experimental Analysis

The key insight from analysing an extensive experimental database covering a wide range of flow conditions susceptible to swept-wing shock buffet is the identification of two distinct, and possibly connected, phenomena that dominate the flow physics around the onset of the shock-buffet instability. First, low-frequency shock unsteadiness at Strouhal numbers between 0.05 and 0.15 (based on mean aerodynamic chord and reference freestream velocity) predominantly propagates pressure disturbances inboard and is already present pre-onset. Second, broadband higher-frequency outboard-

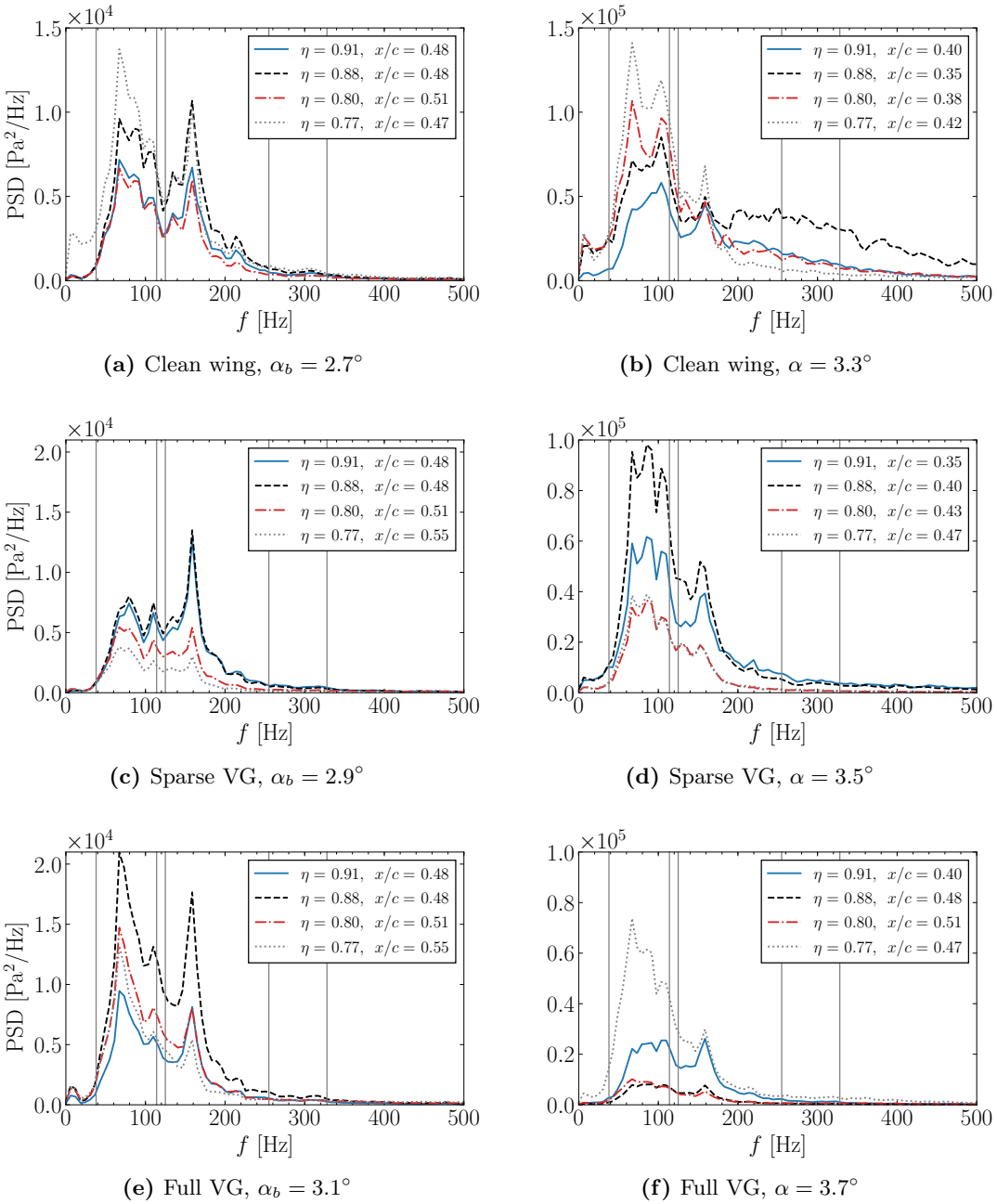

(a) Clean wing, $\alpha_b = 2.7°$ **(b)** Clean wing, $\alpha = 3.3°$

(c) Sparse VG, $\alpha_b = 2.9°$ **(d)** Sparse VG, $\alpha = 3.5°$

(e) Full VG, $\alpha_b = 3.1°$ **(f)** Full VG, $\alpha = 3.7°$

Figure 4.24: Spanwise PSD data approximately along shock at α_b (left) and 0.6° above (right) for the clean wing (top), sparse (middle) and full (bottom) VG configurations at $M = 0.80$. Note the tenfold increase of PSD values at 0.6° beyond α_b.

running perturbations occur along the shock wave and in the downstream shock-induced separated region, at Strouhal numbers between 0.2 and 0.5, only beyond buffet-onset conditions. Up until now, published literature has focused on the second phenomenon whilst the lower-frequency shock unsteadiness has not been analysed thoroughly. Understanding the exact sources and relation between these two observations is too expensive and out of scope for the work herein. Instead, the ability of state-of-the-art

numerical simulation in reproducing the experimental data is scrutinised in Chapter 5, with the hope for more insight. Chapter 6 takes a closer look into these phenomena and provides the pertinent characteristics such as propagation speed and wavelength. The discussion contemplates possible sources for the unsteadiness whilst comparing and contrasting the two phenomena based on the experimental and numerical datasets herein in conjunction with the published literature.

Chapter 5

Numerical Analysis

Scale-resolving simulations in the vicinity of buffet onset are presented complementing the high-quality experimental data analysed in Chapter 4. The numerical simulations employ the delayed detached-eddy simulation approach which is motivated by the desire for accurate prediction at the edge of the flight envelope and feasible computation of separated flow at high Reynolds number. The difficulty in simulating separating and reattaching shallow shear layers with such techniques is well known. Hence, the impact of two subgrid length-scale definitions is investigated. The relevant theoretical foundations are described together with an outline of the numerical method adopted for the scale-resolving simulations performed using the compressible finite-volume solver DLR TAU. A hybrid low-dissipation and low-dispersion numerical scheme is chosen to resolve the inherently unsteady flow physics whilst ensuring numerical stability on hybrid grids. Two hybrid meshes specifically designed for detached-eddy simulation are used. The impact of the subgrid length scale is analysed with two scale-resolving simulations at model scale, using both the standard definition of maximum local spacing and a more recent vorticity-sensitive variant, reproducing the experiment with Reynolds number of 3.75×10^6 and validated against experimental data from traditional steady and unsteady instrumentation together with dynamic pressure-sensitive paint. Another simulation at full scale, with reference Reynolds number of 27×10^6, clarifies scaling effects on shock buffet which is crucial to allow meaningful interpretation of sub-scale wind-tunnel test data and its relation to the full-scale flight vehicle. Modal analysis techniques including proper orthogonal decomposition and dynamic mode decomposition are used to analyse both surface data and field snapshots, allowing direct quantitative comparison with the experimental data based on salient modal features whilst giving critical insight into the flow physics.

5.1 Flow Models and Solver

5.1.1 Flow Models

Governing Equations: Navier–Stokes Equations

The fundamental behaviour of fluid flow is governed by the Navier–Stokes equations. This system of equations is undoubtedly pivotal in the field of fluid dynamics and is derived from first principles of mass conservation, Newton's second law of motion and the first law of thermodynamics, hence conserving mass, momentum and energy. These equations are now widely applied for the computation of practical aerodynamic flows and comprise the top tier of the aerodynamic modelling hierarchy (Blazek, 2015). Considering the governing equations of a compressible Newtonian fluid in differential form allows compact and clear notation using the tensor notation described in Appendix B

$$\begin{aligned} \frac{\partial \rho}{\partial t} + \frac{\partial}{\partial x_i}(\rho v_i) &= 0 \\ \frac{\partial}{\partial t}(\rho v_i) + \frac{\partial}{\partial x_j}(\rho v_j v_i) &= -\frac{\partial P}{\partial x_i} + \frac{\partial \tau_{ij}}{\partial x_j} \\ \frac{\partial}{\partial t}(\rho E) + \frac{\partial}{\partial x_j}(\rho v_j H) &= \frac{\partial}{\partial x_j}(v_i \tau_{ij}) + \frac{\partial}{\partial x_j}\left(\kappa \frac{\partial T}{\partial x_j}\right) \end{aligned} \tag{5.1}$$

where x_i denotes Cartesian coordinates, t represents time, ρ is the density, v_i is a velocity component, E is the total energy per unit mass, T is static temperature, P is static pressure, H represents the total enthalpy, τ_{ij} is the viscous stress tensor, and κ is the thermal conductivity coefficient. The total energy per unit mass and total enthalpy can be obtained from

$$E = e + \frac{1}{2} v_i v_i \quad \text{and} \quad H = h + \frac{1}{2} v_i v_i \tag{5.2}$$

where e is the internal energy per unit mass and h is the specific enthalpy. The viscous stress tensor is

$$\tau_{ij} = 2\mu \; S_{ij} + \lambda \frac{\partial v_k}{\partial x_k} \delta_{ij} = 2\mu \; S_{ij} - \left(\frac{2}{3}\mu\right) \frac{\partial v_k}{\partial x_k} \delta_{ij} \tag{5.3}$$

after applying Stoke's hypothesis (Stokes, 1845) for the bulk viscosity to eliminate the second viscosity coefficient, λ. The terms in Eq. (5.3) include the dynamic viscosity, μ, the strain-rate tensor, S_{ij}, the divergence of the velocity, $\partial v_k / \partial x_k$, and the Kronecker delta, δ_{ij}. The dynamic viscosity μ and the thermal conductivity coefficient, κ, are functions of the state of the fluid. The components of the strain-rate tensor are

$$S_{ij} = \frac{1}{2}\left(\frac{\partial v_i}{\partial x_j} + \frac{\partial v_j}{\partial x_i}\right). \tag{5.4}$$

The Navier–Stokes equations in three dimensions are a system of five equations for the five conservative variables. However, there are a total of seven unknown flow field variables. Thermodynamic relations between the state variables are formulated in order to provide two additional equations. Assuming that the working fluid behaves like a calorically perfect gas, the pressure can be expressed in terms of the conservative variables by combining the equation of state and the following thermodynamic definitions

$$R = c_p - c_v, \quad \gamma = \frac{c_p}{c_v} \tag{5.5}$$

where R is the specific gas constant, c_p and c_v are the specific heat coefficients at constant pressure and volume, respectively, and γ is the heat capacity ratio. To complete the set of equations, the dynamic viscosity, μ, and the thermal conductivity coefficient, κ, are supplied. The dynamic viscosity is strongly dependent on temperature but is only weakly dependent on pressure. The Sutherland formula is typically used to supply the dynamic viscosity coefficient in terms of static temperature, with the latter depending on density, pressure and the heat capacity ratio. In the case of gases, the temperature dependence of κ is similar to that of μ having the following relationship

$$\kappa = c_p \frac{\mu}{Pr} \tag{5.6}$$

where Pr is the Prandtl number and is constant for the entire flow field. The value for air is taken as 0.72.

The direct numerical solution of the Navier–Stokes equations requires vast computational resources which increase dramatically (approximately cubic relationship) with Reynolds number. Despite the massive leaps in computational power over the past few decades, this remains infeasible for industrial aerodynamic problems and is limited to academic cases (Slotnick *et al.*, 2014). For instance, Zauner *et al.* (2019) simulated the transonic flow over an aerofoil at a Reynolds number of 500 000 employing $\mathcal{O}(10^4)$ cores using meshes of $\mathcal{O}(10^9)$ computational points (for a short span of 5% chord length). Flows over complex geometries of industrial interest are instead typically solved by decomposing into a mean and fluctuating component and applying a suitable averaging process. However, this results in additional unknown terms, known as the Reynolds stresses, and a turbulence model is required for closure. Numerous turbulence models varying greatly in complexity and computational expense have been developed over the years. First, an outline of the Reynolds-averaged Navier–Stokes equations (RANS), currently the industrial standard for high Reynolds number applications is provided. After reviewing the widely-used one-equation Spalart–Allmaras turbulence model, detached-eddy simulation (DES), a hybrid method between RANS and large-eddy simulation (LES) bridging the computational requirements and the demand for time-accurate simulation, is described. The interested reader is referred to the book by Wilcox (1993) for a more extensive discussion dealing with turbulence.

Favre- and Reynolds-averaged Navier–Stokes Equations

One way to approximate turbulent flows is to decompose the flow variables into mean and fluctuating components, as proposed by Reynolds (1895). The Reynolds decomposition for an arbitrary variable φ can be written as

$$\varphi = \overline{\varphi} + \varphi' \tag{5.7}$$

where $\overline{\varphi}$ denotes the mean value and φ' represents the fluctuations. The mean value is obtained by time averaging, such that any changes occur in space and not in time. In the case of compressible flow, whereby density cannot be treated as a constant, it is typical to also employ Favre decomposition (Favre, 1965*a*,*b*) which is mass weighted. The Favre average of an arbitrary variable is

$$\widetilde{\varphi} = \frac{1}{\bar{\rho}} \lim_{\Delta t \to \infty} \frac{1}{\Delta t} \int_t^{t+\Delta t} \rho\varphi \mathrm{d}t \tag{5.8}$$

where $\bar{\rho}$ denotes the Reynolds-averaged density and Δt is a time interval, such that the Favre decomposition is

$$\varphi = \widetilde{\varphi} + \varphi'' \tag{5.9}$$

where $\widetilde{\varphi}$ denotes the mean value and φ'' is the fluctuating component. The application of Reynolds averaging to density and pressure and Favre averaging to the remaining flow variables in Eq. (5.1) yields the Favre- and Reynolds-averaged Navier–Stokes equations

$$\begin{aligned}
\frac{\partial \overline{\rho}}{\partial t} + \frac{\partial}{\partial x_i}(\bar{\rho}\tilde{v}_i) &= 0 \\
\frac{\partial}{\partial t}(\bar{\rho}\tilde{v}_i) + \frac{\partial}{\partial x_j}(\bar{\rho}\tilde{v}_j\tilde{v}_i) &= -\frac{\partial \bar{P}}{\partial x_i} + \frac{\partial}{\partial x_j}\left(\tilde{\tau}_{ij} - \bar{\rho}\widetilde{v_i''v_j''}\right) \\
\frac{\partial}{\partial t}(\bar{\rho}\widetilde{E}) + \frac{\partial}{\partial x_j}(\bar{\rho}\tilde{v}_j\widetilde{H}) &= \frac{\partial}{\partial x_j}\left(\kappa\frac{\partial \widetilde{T}}{\partial x_j} - \bar{\rho}\widetilde{v_j''h''} + \widetilde{\tau_{ij}v_i''} - \bar{\rho}\widetilde{v_j''k}\right) \\
&\quad + \frac{\partial}{\partial x_j}\left[\tilde{v}_i\left(\tilde{\tau}_{ij} - \bar{\rho}\widetilde{v_i''v_j''}\right)\right]
\end{aligned} \tag{5.10}$$

where k denotes the turbulent kinetic energy (Wilcox, 1993). The Favre-averaged turbulent kinetic energy per unit volume can be defined as

$$\bar{\rho}\tilde{k} = \frac{1}{2}\bar{\rho}\widetilde{v_i''v_i''} \tag{5.11}$$

and the viscous stress tensor in Eq. (5.10) becomes extended by the Favre-averaged Reynolds-stress tensor

$$\tau_{ij}^F = -\bar{\rho}\widetilde{v_i''v_j''}. \tag{5.12}$$

The total energy and total enthalpy in Eq. (5.10) are

$$\bar{\rho}\widetilde{E} = \bar{\rho}\tilde{e} + \frac{1}{2}\bar{\rho}\tilde{v}_i\tilde{v}_i + \frac{1}{2}\bar{\rho}\widetilde{v_i''v_i''} = \bar{\rho}\tilde{e} + \frac{1}{2}\bar{\rho}\tilde{v}_i\tilde{v}_i + \bar{\rho}\tilde{k} \tag{5.13}$$

$$\bar{\rho}\widetilde{H} = \bar{\rho}\tilde{h} + \frac{1}{2}\bar{\rho}\tilde{v}_i\tilde{v}_i + \frac{1}{2}\bar{\rho}\widetilde{v_i''v_i''} = \bar{\rho}\tilde{h} + \frac{1}{2}\bar{\rho}\tilde{v}_i\tilde{v}_i + \bar{\rho}\tilde{k} \tag{5.14}$$

using the definition in Eq. (5.11). The averaging procedure results in additional terms and requires six components of the Favre-averaged Reynolds-stress tensor and three components of the turbulent heat-flux vector for closure. Two particular terms on the right-hand side of the energy equation in Eq. (5.10) are the molecular diffusion $\frac{\partial}{\partial x_j}(\widetilde{\tau_{ij}v_i''})$ and the turbulent transport of the turbulent kinetic energy $\frac{\partial}{\partial x_j}(\bar{\rho}\widetilde{v_j''k})$. These terms are often neglected in transonic and supersonic flows (Wilcox, 1993).

An important concept in turbulence modelling is the Boussinesq hypothesis (Boussinesq, 1877). This assumes a linear relationship between the turbulent shear stress and the mean strain rate, using eddy viscosity, μ_t, as the proportionality factor. In the case of the compressible Favre- and Reynolds-averaged Navier–Stokes equations, this reads

$$\tau_{ij}^F = -\bar{\rho}\widetilde{v_i''v_j''} = 2\mu_t\widetilde{S}_{ij} - \left(\frac{2}{3}\mu_t\right)\frac{\partial\tilde{v}_k}{\partial x_k}\delta_{ij} - \frac{2}{3}\bar{\rho}\tilde{k}\delta_{ij}. \tag{5.15}$$

This equation is similar to Eq. (5.3) and the dynamic viscosity coefficient μ in the viscous stress tensor is typically replaced by the sum of a laminar and turbulent part ($\mu = \mu_l + \mu_t$), whereby Sutherland's law is used for the former and the latter is supplied by the turbulence model, unless second-order closures (Reynolds-stress models) are employed. The turbulent heat-flux vector is based on the classical Reynolds analogy

$$\bar{\rho}\widetilde{v_j''h''} = -\kappa_t\frac{\partial\widetilde{T}}{\partial x_j} \tag{5.16}$$

and the turbulent thermal conductivity coefficient, κ_t, is calculated from Eq. (5.6) and using the turbulent values for the Prandtl number ($Pr_t = 0.9$) and the dynamic viscosity coefficient.

Spalart-Allmaras Turbulence Model

There is a large family of turbulence models that can be used for closure of the RANS equations, usually classified by the order of the closure. A detailed overview can be found in Wilcox (1993). The one-equation Spalart–Allmaras (S–A) model (Spalart & Allmaras, 1992) is a routinely used tubulence model for aerospace applications. The turbulent eddy viscosity is defined as

$$\mu_t = f_{v1}\rho\hat{\nu} \tag{5.17}$$

where f_{v1} is a near-wall damping function and $\hat{\nu}$ is the intermediate eddy-viscosity variable. The function f_{v1} depends on the intermediate eddy viscosity $\hat{\nu}$ and the laminar kinematic viscosity ($\nu_l = \mu_l/\rho$)

$$f_{v1} = \frac{\chi^3}{\chi^3 + C_{v1}^3}, \quad \text{where} \quad \chi = \frac{\hat{\nu}}{\nu_l} \quad \text{and} \quad C_{v1} = 7.1. \tag{5.18}$$

The intermediate eddy viscosity is obtained from the transport equation having the following form

$$\frac{\partial \rho\hat{\nu}}{\partial t} + \frac{\partial}{\partial_j}(\rho\hat{\nu}v_j) = \mathcal{P}_{\rho\hat{\nu}} + \mathcal{D}_{\rho\hat{\nu}} + \mathcal{W}_{\rho\hat{\nu}} \tag{5.19}$$

where the terms on the right-hand side denote the production, diffusion and near-wall turbulence destruction terms, respectively. Each of these is computed via a number of auxiliary functions and calibrated constants available in Spalart & Allmaras (1992). A negative variant called the negative S–A model was developed more recently with slight modifications to the production, destruction and diffusion terms, specifically targeted towards under-resolved grids and unphysical transient states (Allmaras *et al.*, 2012). This is the turbulence model used consistently herein.

Detached-Eddy Simulation

The challenges imposed by massively separated flow at high Reynolds number together with the demand for accurate predictions on the edge of the flight envelope have motivated the development of scale-resolving simulations. Time averaging loses its validity in flow problems where the mean-flow frequencies are of the same order as the turbulent fluctuations (Blazek, 2015). LES is usually employed for the detailed prediction of unsteady flow phenomena where standard turbulence models fail. However, LES imposes high requirements on spatial and temporal resolution, greatly increasing computational cost. Furthermore, direct numerical simulation requires yet more extensive computational resources and is hence currently limited to low Reynolds number and relatively simple flow problems. This has driven the idea behind hybrid RANS/LES methods such as the well-known DES approach which is designed to treat attached boundary layers with the RANS formulation and apply LES in separated-flow regions. The reader is referred to the work by Spalart *et al.* (1997) who provide a detailed motivation for the introduction of this method.

The original DES formulation is based on the S–A turbulence model and is typically referred to as DES97. The original idea was to have a single turbulence model functioning as a subgrid-scale model for LES in fine enough regions and a RANS model in coarser regions (Travin *et al.*, 2000). The transport equation of the S–A turbulence model contains a destruction term for its intermediate eddy viscosity $\hat{\nu}$, proportional to $(1/d)^2$, where d is the minimum distance to a wall. Instead, the variable d is replaced

by the DES length scale

$$l_{\mathrm{DES}} = \min(d, C_{\mathrm{DES}}\Delta) \tag{5.20}$$

where C_{DES} is a constant and Δ is a grid spacing parameter, denoted as subgrid length scale and motivated by the presence of highly anisotropic grids especially in the boundary-layer region (Spalart *et al.*, 1997). This was originally defined as the largest grid spacing in all directions, $\Delta = \Delta_{\max} = \max(\Delta x, \Delta y, \Delta z)$, whilst the C_{DES} constant was found to be optimal at 0.65 for homogeneous turbulence (Strelets, 2001).

A common issue encountered in the literature when using DES in its original form, that is, treating the boundary layer with a RANS model and employing LES in separated regions, is the grey area problem and the high dependency on grid spacing. The grey area refers to the transition between the RANS and LES regions. This poses an intrinsic difficulty in DES unless the separation is abrupt, often fixed by the geometry (Spalart, 2009). Furthermore, the grid spacing can result in so-called modelled-stress depletion with more severe cases ultimately causing premature grid-induced separation (Menter & Kuntz, 2004). Modelled-stress depletion arises when the grid activates the DES limiter ($l_{\mathrm{DES}} = C_{\mathrm{DES}}\Delta$) but is not fine enough to support the resolved LES content and velocity fluctuations. In turn, the eddy viscosity and consequently the modelled Reynolds stress are too low, without any resolved stress to restore the balance (Spalart *et al.*, 1997). This incorrect behaviour is pertinent in problems with thickening boundary layers and shallow separation regions (Spalart *et al.*, 2006). Such inherent difficulty to the original DES method should be accounted for when simulating shock buffet, whereby a shallow separation bubble may be induced by a moving shock position without a clear geometric feature.

The delayed detached-eddy simulation (DDES) approach was introduced by Spalart *et al.* (2006) with a change in formulation to account for these deficiencies. The main idea is to shield the boundary layer, preserving RANS mode and delaying the LES function by making the DES length-scale limiter also dependent on the solution, rather than the grid only (Spalart, 2009). The modified DDES length scale is

$$l_{\mathrm{DDES}} = d - f_{\mathrm{d}} \max\left(0, d - C_{\mathrm{DES}}\Delta\right) \tag{5.21}$$

where f_{d} is the delay function computed as

$$f_{\mathrm{d}} \equiv 1 - \tanh([8r_{\mathrm{d}}]^3) \quad \text{and} \quad r_{\mathrm{d}} = \frac{\hat{\nu}}{\sqrt{U_{i,j}U_{i,j}}\kappa^2 d^2} \tag{5.22}$$

where $U_{i,j}$ denotes the velocity gradients and κ is the von Kármán constant. The delay function is designed to be $f_{\mathrm{d}} = 1$ in the LES region giving DES97 and $f_{\mathrm{d}} = 0$ elsewhere, resulting in RANS mode. With the introduction of the delayed formulation, the length scale now depends on both intermediate eddy viscosity and the grid spacing, hence taking into account the state of the time-dependent flow (Spalart *et al.*, 2006).

Furthermore, various definitions for the subgrid length scale Δ have been introduced over the years. A commonly applied length scale in LES is the cube-root of the grid-cell volume, $\Delta_{\text{vol}} = \sqrt[3]{\Delta x \Delta y \Delta z}$ (Breuer, 1998). However, the definition based on grid spacing is preferred in DES as explained by Shur *et al.* (2015). Moreover, vorticity based definitions that take into account the state of the flow have been introduced with the aim to reduce dependence on grid spacing. For the following discussion, the flow is assumed in the x-direction and gradients predominantly in the y-direction. The concept of making Δ depend not only on the grid spacing but also on the flow solution using the local vorticity vector was introduced by Chauvet *et al.* (2007) and generalised for unstructured meshes by Deck (2012). This formulation of a vorticity sensitive subgrid length scale Δ_ω removes the dominance of the grid spacing in the z direction and reduces to $\sqrt{\Delta x \Delta y}$ when the flow is essentially two-dimensional with the vorticity vector aligned with the coarse z direction. However, this definition, similar to the Δ_{vol}, still involves the smallest of grid spacings and is physically unjustified (Mockett *et al.*, 2015; Shur *et al.*, 2015). For this reason, Mockett *et al.* (2015) introduced an alternative definition which lessens the influence of the smallest grid direction and reduces to $\max(\Delta x, \Delta y)$. Consider a cell with centre vector $\mathbf{r}$ and vertices located at $\mathbf{r}_n$, where $n = 1, \ldots, 8$ for hexahedral cells, this vorticity-sensitive subgrid length scale that reduces to a maximum edge formulation is

$$\tilde{\Delta}_\omega = \frac{1}{\sqrt{3}} \max_{n,m=1,8} |(\mathbf{l}_n - \mathbf{l}_m)| \tag{5.23}$$

where $\mathbf{l}_n$ is a set of cross-product points computed as $\mathbf{l}_n = \mathbf{n}_\omega \times (\mathbf{r}_n - \mathbf{r})$ and $\mathbf{n}_\omega$ is the unit vector aligned with the vorticity vector. Therefore, this definition is equal to the diameter of the set of cross-product points divided by $\sqrt{3}$.

While a detailed discussion is given by Shur *et al.* (2015), a brief explanation is provided for a free shear layer. Consider a free shear layer flowing in the $x-y$ plane. The grid is anisotropic with a much larger Δz when compared to Δx and Δy. Assuming that the vorticity vector is nearly aligned with z in the initial region of the shear layer, then the flow is essentially two-dimensional. Therefore, $\tilde{\Delta}_\omega$ defined by Eq. (5.23) reduces to $\frac{1}{\sqrt{3}} \left(\Delta x^2 + \Delta y^2\right)^{1/2}$. This is of $\mathcal{O}\left(\max\left\{\Delta x, \Delta y\right\}\right)$, rather than Δz in the case of $\Delta_{\max}$, or $\sqrt{\Delta x \Delta y}$ in the case of Δ_ω. This makes sense physically since the eddies have nearly the same scale in x and y and can be resolved accurately since their size is limited by the larger of these two grid directions (Shur *et al.*, 2015). In the case of three-dimensional flow, $\tilde{\Delta}_\omega$ is of the order of $\Delta_{\max}$ unless the vorticity vector is aligned with one of the grid coordinate directions, such that it reduces to $\mathcal{O}\left(\max\left\{\Delta_i, \Delta_j\right\}\right)$. Therefore, the smallest grid spacing does not rule (Mockett *et al.*, 2015).

5.1.2 Flow Solver

All simulations presented herein were performed using the unstructured compressible finite-volume solver TAU, developed by the German Aerospace Center (DLR). The

DLR-TAU software package is widely used in the European aerospace sector and various validation studies are available in the literature (see for example Schwamborn *et al.* (1999) and Schwamborn *et al.* (2006)). The second-order central scheme is used to discretise the inviscid fluxes of the mean flow equations in all simulations. Scalar artificial dissipation is used for steady RANS simulations whilst a minimal level of fourth-order matrix-valued artificial dissipation is used in DDES to minimise discretisation errors (including both dissipation and dispersion) and provide sufficient numerical stability (Probst & Reuß, 2015), as will be explained in the next paragraph. The turbulence model of choice herein is the negative S–A model. The first-order Roe scheme is employed to discretise the convective fluxes of the turbulence equation in the case of steady RANS and the second-order central scheme is used for DDES. Previous experience has shown that the prediction of unsteady regions is sensitive to both the choice of turbulence-model discretisation and the variant of a specific turbulence model (notably the use of a compressibility correction to the S–A model (Spalart, 2000)). Effectively, the choices made can have an impact on the eddy-viscosity levels, which can inhibit the unsteadiness (see for instance Crouch *et al.* (2007), Grossi *et al.* (2014), Sartor & Timme (2017) and Plante *et al.* (2019)). Gradients of the flow variables are reconstructed with a least-squares approach which minimises errors in a hybrid mesh, such as those used herein. Switching between RANS and LES regions is investigated by using two definitions of the subgrid length scale; the first is the classical DES choice of $\Delta_{\max}$ and the second is a vorticity-sensitive filter, denoted $\tilde{\Delta}_{\omega}$. The latter definition can detect the dominant two-dimensional character of early shear layers to promote a faster unlocking of the Kelvin–Helmholtz instability and early development of resolved turbulence, as described in the previous section.

The numerical methods within existing second-order-accurate finite-volume flow solvers are primarily designed for steady-state problems with smooth large-scale structures in their statistically averaged solution (Löwe *et al.*, 2016). Most numerical methods, even high-order codes used for efficient RANS computations, have numerical dissipation that yields inaccurate representation of the medium- to small-scale turbulent structures. However, the underlying time-accurate flow physics are unsteady and vortex dominated, with their space-time behaviour exhibiting a broad range of turbulent scales, requiring accurate resolution (Moin, 2002). Although the requirements of suitable numerical methods for scale-resolving simulations is an ongoing theme of research, their dissipative and dispersive properties have been identified as crucial elements. A low-dissipation scheme is one that is numerically stable with significantly reduced levels of numerical dissipation. One way to achieve this is to employ numerical methods based on the skew-symmetric form for the convection operator, as explained by Kravchenko & Moin (1997). Furthermore, dispersive properties affect the shape of the vortices that are convected with the mean flow. It is essential for the numerical method to preserve coherent structures existing over a large range of spatial and temporal scales that ex-

change mass, momentum and energy (Probst *et al.*, 2016; Löwe *et al.*, 2016). The hybrid low dissipation and low dispersion (LD2) scheme is employed for all scale-resolving simulations presented herein using DDES with low-Reynolds-number correction (Spalart *et al.*, 2006). The latter is readily available in TAU and was previously used for RBC12 simulations well beyond shock-buffet onset (Sartor & Timme, 2017). Low dissipation is ensured by setting the fourth-order dissipation coefficient to 1/256 for the reference scheme and 1/1024 for the LD2 scheme. This scheme is essential for scale-resolving simulations as explained in Appendix C which summarises the development of such numerical methods based on the work by Löwe *et al.* (2016) and Probst *et al.* (2016).

With regards to temporal discretisation, steady-state simulations employ local time-stepping to accelerate convergence in combination with a semi-implicit Backward-Euler scheme with a lower-upper symmetric Gauss–Seidel solver. In the scale-resolving time-marching simulations, the standard second-order dual-time stepping approach of Jameson (1991) (using the steady-state solver for convergence in dual time) is employed. The physical time steps are $1\,\mu$s and $20\,\mu$s at model scale and full scale, respectively. These correspond to a CFL number of $\mathcal{O}(1)$, calculated using the grid spacing in the *focus region* (the region close to the body where flow separation and turbulence must be well resolved) and a conservative measure of 1.5 times freestream velocity (Spalart, 2001). A dynamic Cauchy convergence criterion is applied for dual-time iterations, controlled by the drag coefficient with a relative error smaller than 10^{-8} within the last 20 iterations. Moreover, a minimum of 100 inner iterations is always performed such that the density residual norm converges by at least an order of magnitude. For the full-scale simulation, a minimum of 150 inner iterations is specified instead.

5.2 Test Case and Data Description

5.2.1 Numerical Setup

Flow Conditions

The test case is the half wing-body configuration called RBC12, earlier described in Chapter 3. When studying the influence of flight conditions, the experimental half-model dimensions were scaled up by a factor of 17.5. The reference Reynolds number based on MAC is 3.75×10^6 for the model-scale simulations and 27×10^6 for the full-scale simulation. For numerical simulations, transition was fixed at model scale to replicate the wind-tunnel test employing boundary-layer tripping, as explained in Section 4.1.3, whereas fully-turbulent conditions were assumed at full scale. Far-field conditions using a hemispherical domain are applied at a distance of 25 semi-span lengths (around 90 MACs) and a symmetry boundary condition is imposed on the centre plane.

The model-scale simulations aim to match the experimental aerodynamic flow-field in the vicinity of buffet onset. This sets the current simulations apart from previous

Table 5.1: Flow conditions for scale-resolving simulations at model and full scale.

Parameter	Model scale	Full scale
Mach number	0.801	0.801
Re_{MAC}	3.75×10^6	27.03×10^6
Angle of attack, deg.	3.1	3.1
Reference temperature, K	266.5	216.7
Reference pressure, kPa	66.0	20.7
Reference length, m	0.279	4.881
Reference density, kg/m^3	0.863	0.333

studies which were conducted at conditions well beyond buffet onset ($> (\alpha_b + 1.0°)$). The geometry is considered rigid excluding any static deformation or dynamic fluid-structure interaction, such that the study focuses exclusively on the inherent fluid dynamics of shock buffet. The RBC12 model has been extensively tested in the Aircraft Research Association Transonic Wind Tunnel and any static deformation is believed to have negligible influence, as discussed by Lawson *et al.* (2016). This assertion requires further scrutiny and finite-element studies of the model together with numerical simulations taking into account the deformation are suggested for future work. At the design Mach number of 0.80, a critical angle of attack of around $\alpha = 3.0°$ was obtained from unsteady RANS simulations using forced transition (Sartor & Timme, 2015) and a global stability analysis in fully turbulent conditions (Timme & Thormann, 2016), when using the S–A model for turbulence closure. In the present simulations, the angle of attack was set at $\alpha = 3.1°$ after running a number of short exploratory time-marching simulations at lower angles. In order to simulate the influence of flight conditions and Reynolds number effects on buffet onset, atmospheric conditions at an altitude of 38 000 ft based on the U.S. Standard Atmosphere (NASA, 1976) were considered. The flow conditions for the scale-resolving simulations are summarised in Table 5.1.

Computational Mesh

Hybrid meshes were produced by the Aircraft Research Association using the SOLAR mesh generator (Shaw *et al.*, 2003) generally following industry best-practice guidelines (Rudnik *et al.*, 2018). The meshes consist of hexahedral-, prism- and tetrahedral-type elements and were highly refined to resolve the turbulent structures in the separated zone. Rather than just scaling the model-scale mesh, a new mesh was generated after scaling the geometry in order to maintain the same y^+ of around 0.5, such that wall functions are not used. Some key figures of the meshes are summarised in Table 5.2. Two large mesh sources for the LES focus region were added to the standard meshing sources routinely used in complex wing geometries, as depicted in Fig. 5.1. The first source extends from $\eta = 0.60$ to just outboard of the wing tip in a spanwise sense and

Table 5.2: Mesh information both at model and full scale.

Parameter	Model scale	Full scale
Mesh points n, ($\times 10^6$)	50.4	52.2
Elements, ($\times 10^6$)	203.1	207.0
First cell height, m	5.30×10^{-7}	1.35×10^{-6}
Target spacing Δ_0, m	0.0007	0.0150
Target spacing Δ_0, MAC	0.003	0.003

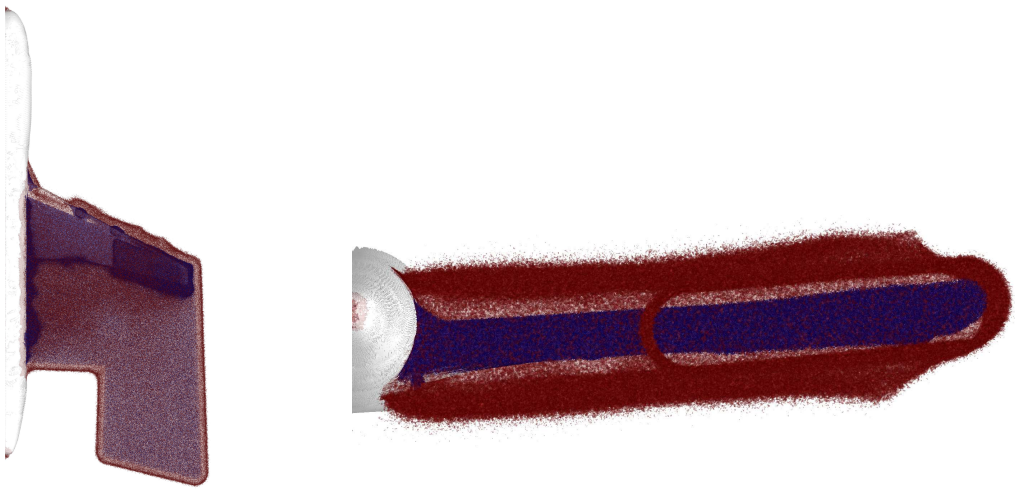

Figure 5.1: Isovolumes of model-scale mesh highlighting refinement due to LES mesh sources; top view on the left, back-to-front view on the right. Highly-refined elements of size $5 \times 10^{-9}\,\mathrm{m}^3$ are shaded in blue, larger elements of size $5 \times 10^{-8}\,\mathrm{m}^3$ are shaded in red.

from just aft of the leading edge to around 4 MACs downstream of the trailing edge in the chordwise direction. In this region, the surface elements have a target spacing of $\Delta_0 \approx 0.003$ MAC, $\Delta_0 = \max(\Delta x, \Delta y, \Delta z)$. This value is similar to that used in a previous DDES simulation by Grossi *et al.* (2014) employing 0.004 chord length target spacing near the shock location to simulate aerofoil buffet. The location of this finest region in the mesh was informed by experimental analysis (Lawson *et al.*, 2016; Masini *et al.*, 2020) and previous simulations (Sartor & Timme, 2017; Timme & Thormann, 2016), both showing separation on this wing to occur first on outboard sections. The second source covers the inboard region, extending from the wing root to $\eta = 0.60$, and approximately 2 MACs downstream of the crank. Although the mesh spacing in this region is larger, $\Delta_0 \approx 0.007$ MAC, this source was primarily included to have a smooth transition from the highly refined outboard region in case eddies propagate inboard.

5.2.2 Data Output and Post Processing

The model-scale simulation with the classical DES subgrid length scale (referred to as DDES I) was run for a total physical time of 0.121 s (121 000 time steps) and is

Table 5.3: Summary of numerical data analysed using modal analysis techniques.

Dataset	Type	Variable	f_s (kHz)	m	t_1 (s)	t_m (s)
Experimental	Surface (DPSP)	C_P	2	10000	0.0005	5
Numerical	Surface (DDES I)	C_P	10	906	0.0305	0.121
Numerical	Surface (DDES II)	C_P	10	501	0.05	0.1
Numerical	Surface (DDES FS)	C_P	0.2	203	0.18	1.19
Numerical	Field (DDES I)	C_P	4	363	0.0305	0.121
Numerical	Field (DDES I)	u	20	261	0.081	0.094

considered as a complete simulation with eighteen buffet cycles allowing statistical analysis after an initial transient phase. The total physical time of the second simulation at model scale employing the vorticity-sensitive definition (referred to as DDES II) is 0.06 s (60 000 time steps) after restarting from an arbitrary instantaneous flow field of DDES I at $t = 0.04$ s. DDES II comprises around twelve buffet cycles, sufficient to assess the influence of this more recent formulation. The full-scale simulation (denoted DDES FS) aiming to study the influence of flight Reynolds number also uses the classical DES subgrid length scale and was run for a total physical time of 1.19 s (59 500 time steps), comprising around twelve buffet cycles. Flow-field data were gathered at every 250 time steps, equating to a sampling frequency, f_s, of 4 kHz at model scale and 0.2 kHz at full scale, respectively. Surface data was output at 10 kHz and 0.2 kHz, respectively. Additionally, a portion of the DDES I field data was sampled at 20 kHz, between 0.081 s and 0.094 s, to investigate higher-frequency behaviour in the wing wake. For this more complete simulation, point data was also sampled at every time step (1 MHz) at 37 specific locations—27 of which correspond to the unsteady pressure transducers on the wind-tunnel model, depicted previously in Fig. 4.1b, and 10 points are located in the wake along two spanwise stations at $\eta = 63\%$ and 77% semi-span. These sampling rates were chosen to resolve the dynamics of swept-wing buffet, namely, large-scale shock motion and associated buffet cells in the separated region. Moreover, both qualitative and quantitative comparisons with the experimental dataset are possible, including direct comparison with the unsteady surface pressure data measured with DPSP.

In addition to traditional post processing, these massive datasets are analysed using data-based modal analysis techniques, including POD and DMD. The flow-field data are decomposed into a set of spatio-temporal modes aiding the elucidation of the flow dynamics, as explained in Chapter 2. In this chapter, the input is a set of vectors (commonly called snapshots) each consisting of n spatial points (in this case the computational points) at each instance in time (for $i = 1, \ldots, m$). Modal decomposition is performed using the vector-space approach described in Appendix A, enabling the analysis of the whole dataset. An overview of the data analysed in this chapter is summarised in Table 5.3, where t_1 and t_m denote the physical time of the first and

last snapshot, respectively. Flow variables are considered separately for the modal decomposition. Previous work employing data-based modal analysis for fluid flow has reported no considerable differences when using a combination of flow variables rather than separate variables (Ohmichi *et al.*, 2018). In contrast, reduced-order modelling using modal methods for subspace projection of the operator typically utilises the entire state vector (Bekemeyer & Timme, 2019).

5.3 Conventional Analysis

Results from steady-state and time-accurate simulations are analysed using conventional techniques such as pressure distributions and spectral analysis. These are compared with the experimental analysis giving confidence in the numerical approach.

5.3.1 Steady-State Simulations

Steady-state simulations were performed and analysed for the validation of the newly generated meshes and to elucidate the surface flow-field features, before running any computationally intensive time-accurate simulations. The angle of attack was varied between $\alpha = 2.0°$ and $3.3°$ in increments of $0.1°$ while closely monitoring the convergence of the density residual norm as a possible indicator of physically unsteady flow. Good convergence of at least nine orders of magnitude was obtained up to $\alpha = 2.8°$ at both model and full scale. The density residual norm levels out beyond $\alpha = 2.9°$ and does not converge deeper than five orders of magnitude at wind-tunnel conditions. For the full-scale simulations, convergence of up to six orders of magnitude is achieved for angles of attack not exceeding $3.0°$ and five orders of magnitude at higher angles of attack. Those stagnating convergence norms suggest unsteady flow.

The surface pressure coefficient on the upper surface for several angles of attack is presented in Fig. 5.2. Figures 5.2a through 5.2d show the time-averaged values from the experimental DPSP dataset around buffet onset. The corresponding results from numerical steady-state simulations at both wind-tunnel and full scale are depicted in Figs. 5.2e through 5.2l. The numerical surface pressure visualisations are enhanced by skin-friction lines and the boundaries of reverse-flow regions (based on streamwise velocity component) are denoted by the dashed lines. It should be noted that for any particular angle of attack, the experimental data without the flow angle correction results in a lower lift coefficient, as discussed later in relation to Fig. 5.9. However, the evolution of surface-flow phenomena with increasing angle of attack from pre-onset to beyond onset is similar. Essentially, trailing-edge separation confined to the outboard wing rapidly merges with the shock-induced separation bubble resulting in a region of localised separation on the outboard wing. The RANS simulations at $\alpha = 2.6°$ predict a shock-induced separation bubble which extends from mid-span and almost reaches

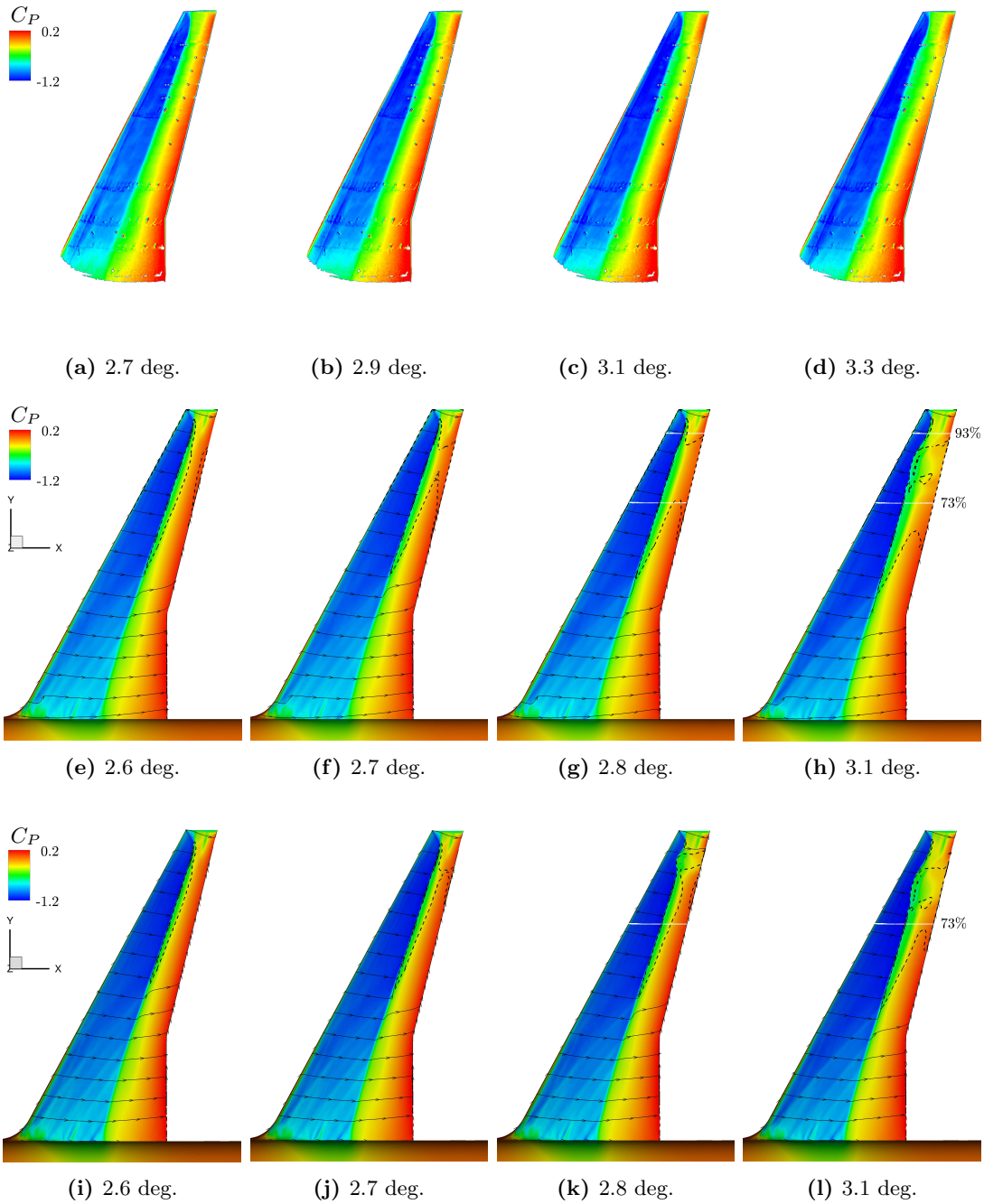

(a) 2.7 deg. **(b)** 2.9 deg. **(c)** 3.1 deg. **(d)** 3.3 deg.

(e) 2.6 deg. **(f)** 2.7 deg. **(g)** 2.8 deg. **(h)** 3.1 deg.

(i) 2.6 deg. **(j)** 2.7 deg. **(k)** 2.8 deg. **(l)** 3.1 deg.

Figure 5.2: Comparison of surface pressure coefficient distribution from experiment and steady-state simulations at a range of angles of attack; (a–d) mean surface pressure from experimental DPSP, (e–h) model-scale simulations ($Re_{\mathrm{MAC}} = 3.75 \times 10^6$) and (i–l) full-scale simulations ($Re_{\mathrm{MAC}} = 27 \times 10^6$). The surface flow is highlighted by skin friction lines and boundaries of reverse-flow regions are denoted by the dashed lines.

the wing tip. At model scale, trailing-edge separation occurs between 70 and 89% semi-span. Although this is not visible at full scale, as soon as the angle of attack is slightly increased to 2.7°, the incipient separation at the trailing edge starts to merge

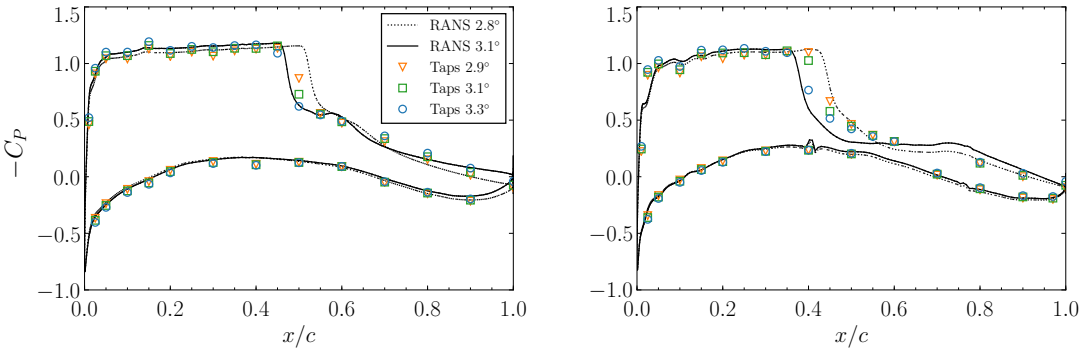

(a) 73% semi-span **(b)** 93% semi-span

Figure 5.3: Chordwise pressure distributions from steady-state simulations at model scale (lines) and experimental static pressure taps (symbols) at two outboard sections.

with the shock-induced separation bubble and the reverse-flow region widens with angle of attack. This corroborates the flow physics around buffet onset on the RBC12 wing analysed at a wide range of Mach numbers, both experimentally in Chapter 4 and numerically (Sartor & Timme, 2016). This localised separated flow perturbs the shock, causing an upstream motion of the shock position with angle of attack, sometimes referred to as inverse shock motion, eventually generating spanwise oscillations visible from the shock trace at $\alpha = 3.1°$. These observations indicate that separated flow at full scale is only slightly delayed compared to model scale, and therefore, the shock buffet onset incidence is expected to be similar to that at model scale. In the same spirit, the onset angle obtained for the NASA Common Research Model in different studies did not vary noticeably for a range of Reynolds number between 1.5×10^6 and 40×10^6 (Illi *et al.*, 2013; Ohmichi *et al.*, 2018; Timme, 2020). It must be emphasised that the steady flow field herein is not converged beyond $\alpha = 2.9°$, and any resulting flow unsteadiness from a numerical steady-state solution scheme strictly is not time-accurate due to local time-stepping to help accelerate convergence. Caution is warranted in interpreting such findings. The shock-buffet onset incidence is discussed in detail using time-marching unsteady simulations in Section 5.3.2.

Steady-state chordwise pressure distributions of these RANS simulations were quantitatively assessed with respect to experimental pressure-tap data at representative spanwise locations. Pressure distributions at the two outboard stations labelled in Fig. 5.2h are compared in Fig. 5.3. The formation of a separation region and an associated upstream shock movement with increasing angle of attack can be deduced both from numerical and experimental results following the methodology in Section 2.1.1. At $\alpha = 3.1°$, the RANS pressure distribution at 73% semi-span clearly depicts pressure divergence close to the trailing edge, indicative of incipient separation. This is corroborated by the experimental data, whereby pressure levels diverge with angle of attack between $x/c = 0.60$ and 1.0 at 73% semi-span, as the angle of attack is increased

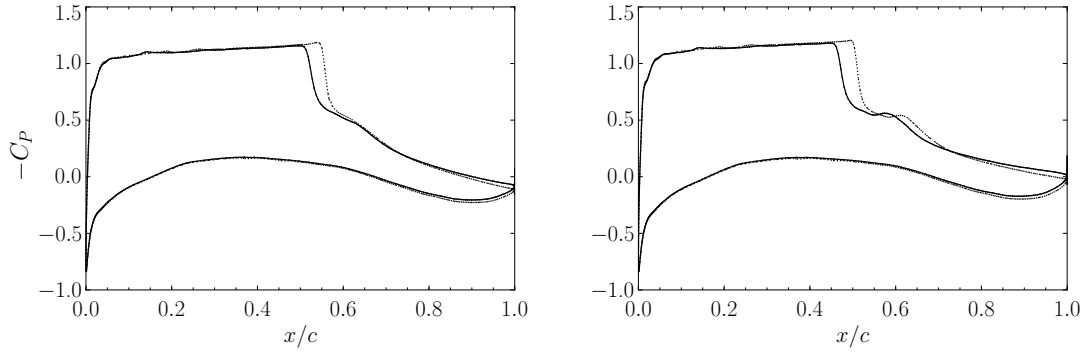

(a) 2.8 deg. **(b)** 3.1 deg.

Figure 5.4: Comparison of chordwise pressure distributions at 73% semi-span; (——) depicts model scale with $Re_{\mathrm{MAC}} = 3.75 \times 10^6$ and (·····) represents full scale with $Re_{\mathrm{MAC}} = 27 \times 10^6$.

from $\alpha = 2.9°$ to $3.3°$. Overall, there is closer agreement with experimental data at higher angle of attack due to the effect of a small flow angle present in the wind-tunnel flow, estimated to be around $-0.35°$, as outlined in Section 4.1.4. Furthermore, the RANS simulations presented herein were compared favourably with solutions obtained previously using several mesh refinement levels (Sartor & Timme, 2015, 2016). The influence of flight Reynolds number on the numerical pressure distributions at 73% semi-span is highlighted in Fig. 5.4. The higher Reynolds number results in a thinner boundary layer and the shock wave sits further downstream, causing a larger extent of supercritical flow and lift generation. A detailed discussion on these points follows.

5.3.2 Delayed Detached-Eddy Simulations

The time-marching simulations using the subgrid length scale $\Delta_{\max}$ (DDES I and DDES FS) were started from partially converged RANS flow fields at each respective angle of attack, whilst the simulation with $\tilde{\Delta}_\omega$ (labelled as DDES II) was started from an arbitrary instantaneous flow field of DDES I at $t = 0.04\,\mathrm{s}$. A concise and intuitive overview of the numerical results together with the underlying experimental DPSP data can be found in the time-averaged surface pressure coefficient in Fig. 5.5 and corresponding standard deviation, σ, in Fig. 5.6. The choice of the experimental angle of attack ($\alpha = 3.3°$) is motivated by the closest total lift coefficient due to the aforementioned flow angle correction, as explained below with the help of Figs. 5.7 and 5.9. The DPSP data at $\alpha = 3.5°$ is expected to result in closer agreement, as will become clear below, but was not processed herein. From Fig. 5.5, it can be deduced that DDES II, compared with DDES I, results in a farther-upstream mean shock position and a wider separation area between approximately 70% and 90% semi-span, in closer agreement with the experimental data. These insights are reinforced by the corresponding standard deviations in Fig. 5.6, which additionally help assessing the level of flow unsteadiness. As expected, the bulk of unsteadiness is confined to the unsteady

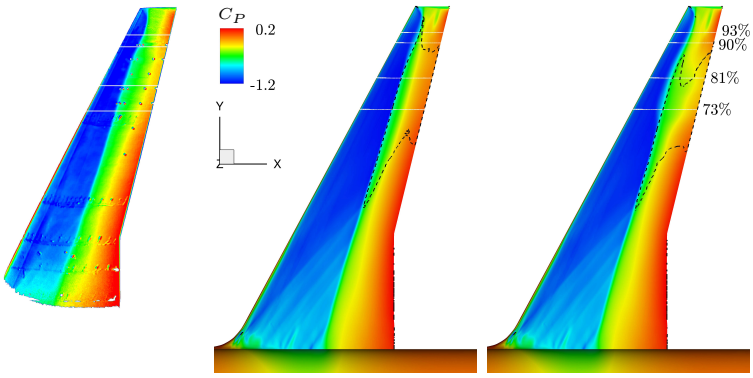

(a) DPSP ($\alpha = 3.3°$) **(b)** DDES I ($0.0305\,\text{s} \leq t \leq 0.121\,\text{s}$) **(c)** DDES II ($0.05\,\text{s} \leq t \leq 0.1\,\text{s}$)

Figure 5.5: Time-averaged surface pressure coefficient, evaluated within given time intervals, comparing experimental DPSP ($\alpha = 3.3°$) and model-scale DDES ($\alpha = 3.1°$). Boundaries of time-averaged reverse-flow regions are denoted by the dashed lines. Slices between 73% and 93% semi-span are further discussed in Fig. 5.7.

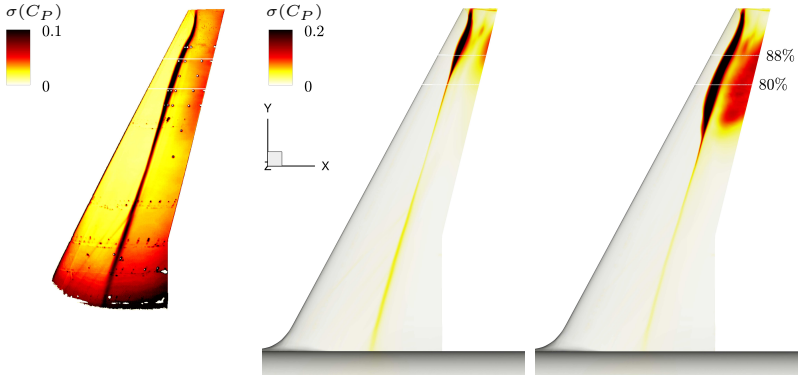

(a) DPSP ($\alpha = 3.3°$) **(b)** DDES I ($0.0305\,\text{s} \leq t \leq 0.121\,\text{s}$) **(c)** DDES II ($0.05\,\text{s} \leq t \leq 0.1\,\text{s}$)

Figure 5.6: Standard deviation of surface C_P, evaluated within given time intervals, corresponding to Fig. 5.5. Slices at 80% and 88% semi-span are further discussed in Fig. 5.8.

shock foot and the localised region of separated flow on the outboard wing. Higher levels of unsteadiness occur where resolved eddies repeatedly impinge on the wing surface along with instantaneous flow separation and reattachment. Albeit overpredicting the level of unsteadiness compared with the experimental data at $\alpha = 3.3°$, the results are promising in that the experimental angle of attack needs further increasing according to the flow angle estimate, which would result in higher values of standard deviation, cf. the experimental data in Sartor & Timme (2017). Furthermore, the experimental values are influenced by camera noise and non-physical artefacts, the variance of which attenuates that from the flow physics, whereas any numerical unsteadiness is originating from the underlying flow features.

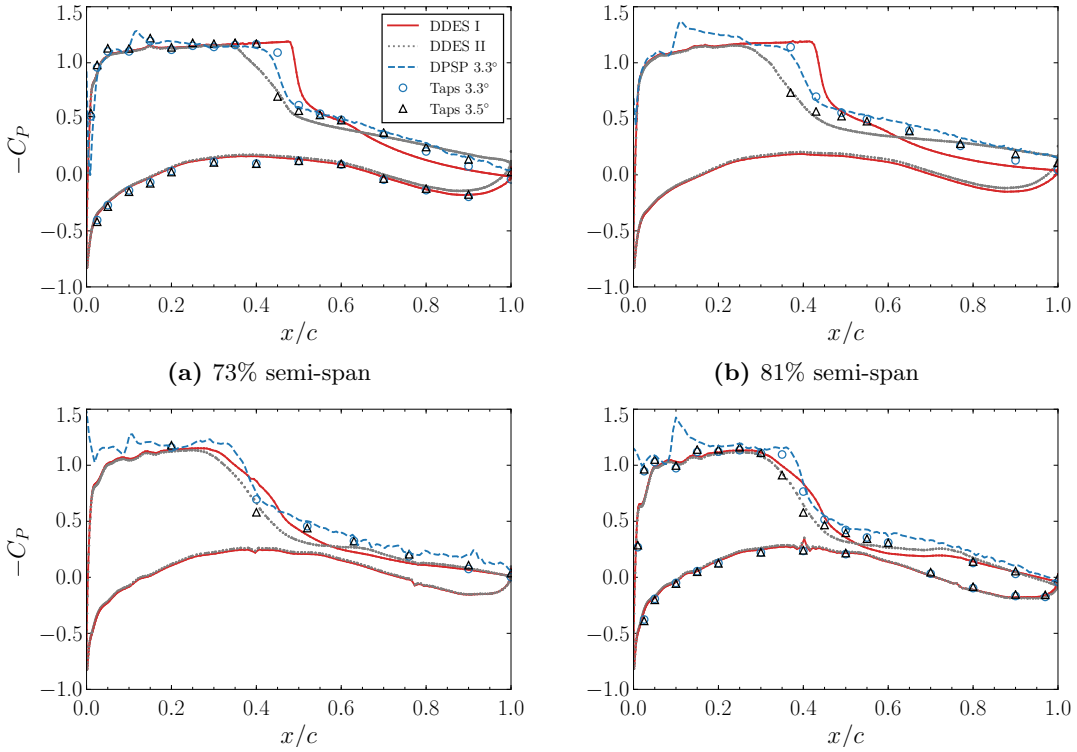

(a) 73% semi-span **(b)** 81% semi-span

(c) 90% semi-span **(d)** 93% semi-span

Figure 5.7: Time-averaged chordwise pressure distributions from DDES ($\alpha = 3.1°$), experimental DPSP ($\alpha = 3.3°$) and static pressure taps at four outboard spanwise stations.

Indeed, while the work in Sartor & Timme (2017) has shown that DDES (using $\Delta_{\max}$) improves upon unsteady RANS simulation well beyond shock-buffet onset at $\alpha = 3.8°$, it is clarified herein that the shock-induced separation near onset requires enhanced treatment for the subgrid length-scale definition, as provided by the $\tilde{\Delta}_\omega$ variant. The closer agreement between DDES II and the experimental DPSP data demonstrates how the vorticity-based subgrid length scale helps better predicting the transition from modelled to resolved turbulence in shallow shear layers. Finally, the experimental data reveal both strong unsteadiness along the shock foot extending along the whole span and highest unsteadiness inboard of the crank. While the latter is the result of measurement noise, specifically those zones are outside of the DPSP focus region, the shock unsteadiness has previously been scrutinised extensively in Chapter 4 and is further discussed in Section 5.4.

A more quantitative discussion on the time-averaged surface pressures is provided in Fig. 5.7 presenting equivalent data at four selected outboard spanwise locations between 73% and 93% semi-span, labelled in Fig. 5.5c. The stations at 81% and 90% semi-span are equipped with a coarser array of pressure taps and limited to the upper surface only, cf. the instrumentation in Fig. 4.1. The figure compares the data from numerical DDES, experimental DPSP and static pressure taps. The impact of the flow

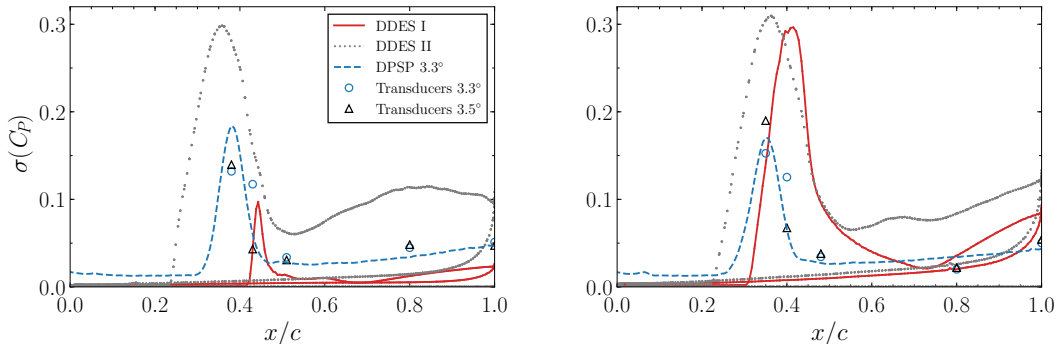

(a) 80% semi-span **(b)** 88% semi-span

Figure 5.8: Chordwise distributions of the standard deviations of surface pressure coefficient from DDES, experimental DPSP and unsteady pressure transducers at two outboard stations.

angle correction, as explained in Section 4.1.4 and mentioned before, is significant. In fact, the best agreement throughout is observed between DDES II at $\alpha = 3.1°$ and the experimental data at $\alpha = 3.5°$, which is indeed very close to the corrected angle of attack due to the flow angle estimate. Two points should be noted. First, the spike in the time-averaged DPSP data at $x/c \approx 0.1$ is an artefact of the transition strip, which is also noticeable in Fig. 5.5a. Second, the DPSP measurement uncertainty relative to static pressure taps translates to a mean of $C_P \pm 0.06$.

These observations are corroborated by the comparison of the standard deviations of surface pressure coefficient at the locations highlighted in Fig. 5.6 and presented in Fig. 5.8. Multiple data sources are combined, including numerical DDES, experimental DPSP and unsteady pressure transducers at two outboard spanwise stations equipped with five discrete sensors each. Numerical data are from the upper and lower surfaces while experimental data have been limited to the former. Considering the complexity of the experimental and numerical setups, together with the required processing of data from disparate sources, there is remarkable agreement between experimental DPSP and DDES II, especially for the shock position, albeit a general trend in overpredicting levels of unsteadiness compared with the DPSP data, previously observed in Sartor & Timme (2017). Such processing includes the alignment and calibration of camera images against pressure taps (Lawson *et al.*, 2016), coordinate-measuring-machine readings of experimental instrumentation and the translation to extract numerical data at the corresponding locations, and the conversion of image pixel indexes to spanwise and chordwise coordinates, using the crank and wing tip, and the leading and trailing edge as reference locations, respectively. The comparisons between the two DDES distributions of both the time averages and standard deviations of surface pressure coefficient clearly show that the shock is consistently located farther upstream in DDES II, with differences particularly distinct at the two inboard stations in Fig. 5.7. This consequently results in a lower lift coefficient, as discussed next.

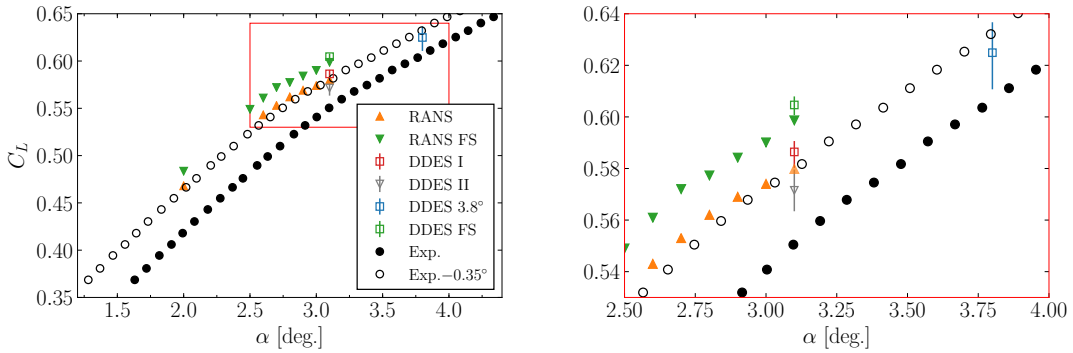

Figure 5.9: Lift coefficient with angle of attack comparing experiment (including the flow angle estimate (○) and excluding it (●)) and CFD (vertical line denotes minimum and maximum of temporal fluctuations). All data at model scale except where indicated by the acronym FS, denoting full scale. Results at $\alpha = 3.8°$ are taken from Sartor & Timme (2017).

Numerical and experimental data of the lift-coefficient variation with angle of attack is provided in Fig. 5.9. Experimental data were measured with a five-component strain-gauge balance and two sets of data are shown in the figure. All data points have been corrected for the interference effects described in Section 4.1.4. Open circles also include an estimated flow angle correction of $-0.35°$. Numerical data from both steady-state and scale-resolving simulations are presented, and, for the latter, the time-averaged value is depicted by the symbols together with minimum and maximum fluctuations in time, denoted by the vertical lines. At model scale, there is good correlation between the numerical and experimental data when the flow angle correction is included, giving confidence in the numerical simulations overall. Data from DDES I and II together with a previous simulation at $\alpha = 3.8°$, reproduced from Sartor & Timme (2017), are included. Focusing on the model-scale simulations at $\alpha = 3.1°$, DDES I undergoes lift fluctuations of approximately ± 0.005 around the mean value, while DDES II has bigger fluctuations of approximately ± 0.008, in agreement with the level of unsteadiness as presented in Fig. 5.6. Numerical simulation at full scale results in higher lift coefficient values in accordance with the pressure distributions presented in Figs. 5.2i through 5.2l and 5.4. Corresponding fluctuations of approximately ± 0.003 around the time-averaged value are smaller, owing to smaller shock excursions when compared to the model-scale simulations. The unsteady flow physics pertaining to these fluctuations are described in more detail in Section 5.4.

Time-resolved histories of integrated values such as the lift coefficient were monitored for two main reasons. First, a transient phase, when high eddy-viscosity regions arising from the steady RANS formulation are destroyed by the less dissipative DDES method, can be identified until the flow develops self-sustained unsteadiness. Second, the frequency content of the fluctuations can be studied, which is useful considering that one of the main differences between aerofoil and swept-wing shock buffet is the spectral signature of the aerodynamic loads. Power spectral density data were estimated using

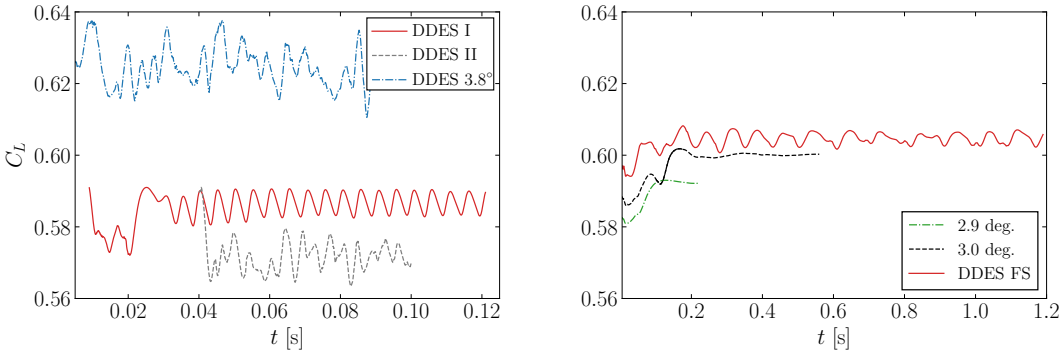

(a) Model scale ($Re_{\mathrm{MAC}} = 3.75 \times 10^6$) **(b)** Full scale ($Re_{\mathrm{MAC}} = 27 \times 10^6$)

Figure 5.10: Time history of the lift coefficient from DDES (note different time axes).

Burg's method (Burg, 1967) to assess the frequency content of the lift fluctuations. This autoregressive model was selected since it provides high frequency resolution even for short signals, typical for such time-accurate simulations. The autoregressive PSD estimation was computed with a single window and an order of 4000 at model scale and 2000 at full scale (having a shorter signal) after conducting a parametric study.

Lift-coefficient time histories from scale-resolving simulations at both model and full scale are shown in Fig. 5.10. At model scale, these include the two current simulations in the vicinity of buffet onset together with a previous DDES at a higher angle of attack $\alpha = 3.8°$, well beyond buffet-onset conditions. Those latter results, which used the $\Delta_{\max}$ subgrid length scale, were reproduced from Sartor & Timme (2017). Previous numerical studies at model scale identified the critical angle of attack to be just above 3.0°, as explained in Section 5.2.1. Short, exploratory time-marching simulations were conducted starting at $\alpha = 2.9°$ in increments of $\Delta\alpha = 0.1°$, based on the indication of physically unsteady flow from the stagnating steady-state convergence. Self-sustained lift fluctuations due to the shock-buffet phenomenon were only observed at $\alpha = 3.1°$ and it was hence decided to pursue the production runs at this angle of attack. An initial transient phase can be observed in the time histories in Fig. 5.10, upon starting the simulations. The complete signal following this start-up (specifically, $t \geq 0.0305\,\mathrm{s}$ for DDES I, $t \geq 0.05\,\mathrm{s}$ for DDES II, and $t \geq 0.18\,\mathrm{s}$ for DDES FS) has been considered as developed shock buffet and is used for the signal processing and subsequent analysis, unless otherwise stated. DDES I results are characterised by fairly regular periodic lift fluctuations caused by an oscillating shock perturbed by a pulsating separation bubble, and vice versa, as discussed in detail later. DDES II, using a more recent, vorticity-sensitive subgrid length scale, yields more intense and less regular lift fluctuations, possibly owing to a wider spanwise separation region and the action of resolved turbulence. Moreover, the average lift coefficient is lower as the mean shock position shifts farther upstream compared to DDES I, as discussed earlier. The scale-resolving simulation at $\alpha = 3.8°$ has a more irregular time-history yet together with larger-amplitude

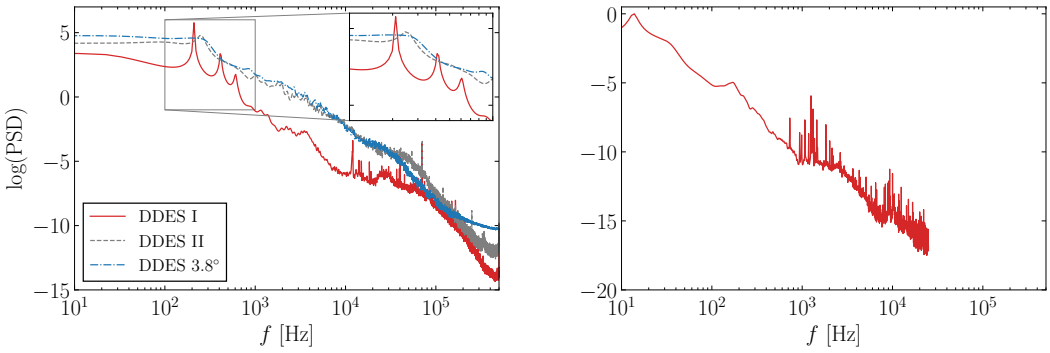

(a) Model scale ($Re_{\mathrm{MAC}} = 3.75 \times 10^6$) **(b)** Full scale ($Re_{\mathrm{MAC}} = 27 \times 10^6$)

Figure 5.11: Power spectral density data of lift fluctuations from DDES.

fluctuations around a higher average value. The full-scale simulation uses the same subgrid length scale as DDES I but results in relatively smaller lift fluctuations having a less periodic nature. The corresponding PSD data for these simulations are depicted in Fig. 5.11. A clear peak at approximately 200 Hz (corresponding to $St = 0.22$) together with its harmonics characterise the spectrum from DDES I, as expected from the underlying time history. The dominant peaks are less well defined in DDES II and the simulation at $\alpha = 3.8°$ due to the irregular nature of the fluctuations. A bump centred at approximately $f = 245$ Hz ($St = 0.27$) is evident from DDES II results. At full scale, peaks are less well defined due to the lower number of simulated buffet cycles that have been simulated. However, a bump is clearly visible between 10 and 14 Hz ($St = 0.21$ to 0.29) in Fig. 5.11b. These frequencies are compatible with typical values reported for swept-wing shock buffet (Benoit & Legrain, 1987; Hwang & Pi, 1975; Dandois, 2016).

In order to judge the resolved turbulent content from the scale-resolving simulations, Figs. 5.12 and 5.13 present instantaneous surface pressure distributions together with slices of eddy-viscosity ratio, μ_t/μ_l, (i.e. the ratio of turbulent-to-laminar viscosity) for DDES I and DDES II, respectively. The snapshots correspond to instances during both a high-lift and a low-lift phase, as seen in Fig. 5.10. The slices are between 50% and 90% semi-span in 10% increments. The highly-refined region encapsulating the outboard wing allows for LES treatment and resolved turbulent content is depicted in the outboard slices. During a shock-buffet cycle, intermittent pockets of shock-induced separation appear predominantly during a local upstream position in the shock oscillation (corresponding to a low-lift phase and hence troughs in the lift history), which is benevolent to the generation of resolved content downstream of the shock. Comparing the results from DDES I and DDES II allows two conclusions. First, the slices from DDES II indicate lower levels of the eddy-viscosity ratio implying more resolved content. Second, an accelerated transition from RANS to LES is visible when applying the vorticity-sensitive formulation in DDES II, resulting in more resolved turbulent content starting in the shear layer above the wing and consequently more

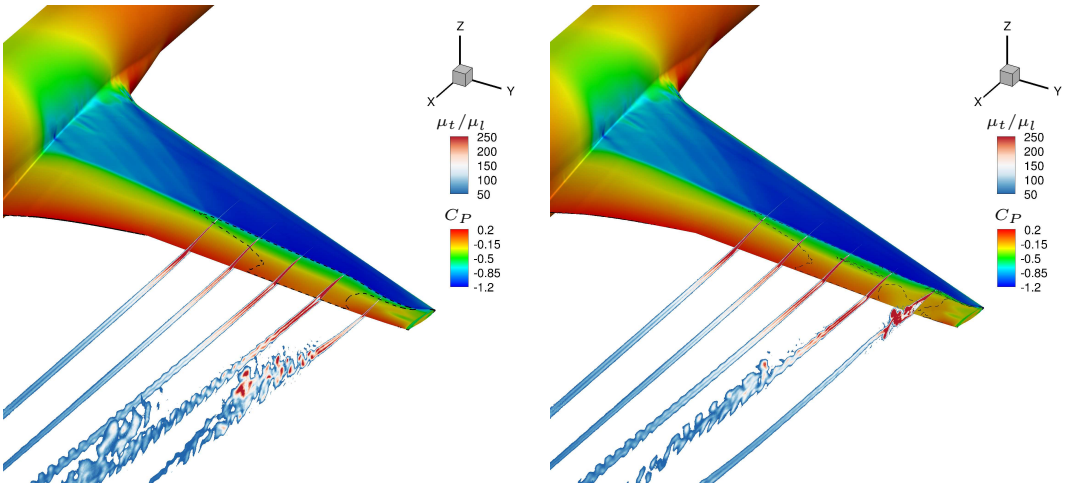

(a) $t = 0.04025\,\mathrm{s}$ **(b)** $t = 0.04325\,\mathrm{s}$

Figure 5.12: Instantaneous surface pressure coefficient and reverse-flow region (denoted by dashed lines) together with slices of eddy-viscosity ratio (μ_t/μ_l) both during a high-lift and low-lift phase at $\alpha = 3.1°$ from DDES I.

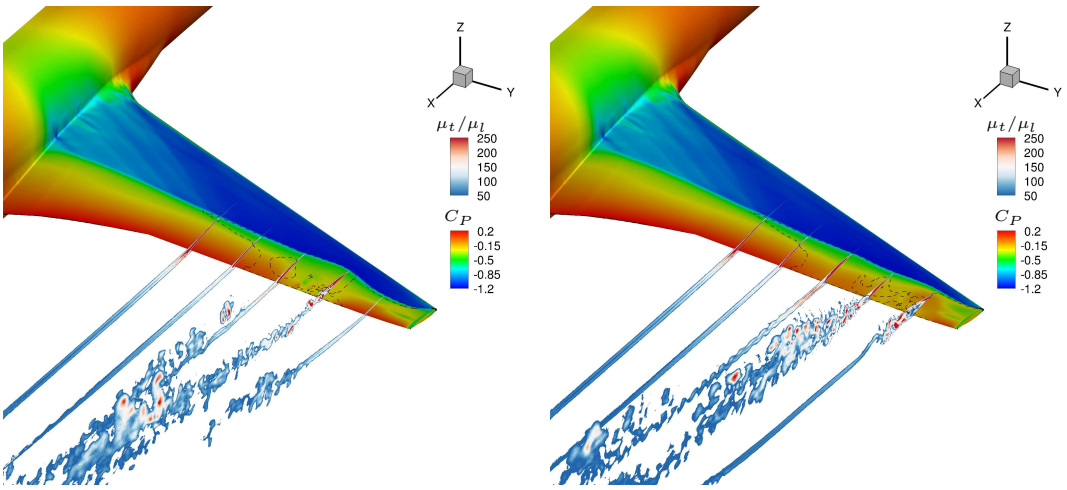

(a) $t = 0.0645\,\mathrm{s}$ **(b)** $t = 0.06725\,\mathrm{s}$

Figure 5.13: Instantaneous surface pressure coefficient and reverse-flow region (denoted by dashed lines) together with slices of eddy-viscosity ratio (μ_t/μ_l) both during a high-lift and low-lift phase at $\alpha = 3.1°$ from DDES II.

content in the wake closer to the wing. This is also evident from Fig. 5.14 which depicts the Q-criterion at a representative outboard slice at 86% semi-span during a low-lift phase. The observation of larger turbulent eddies aft of the trailing edge in DDES I is linked to the more regular lift oscillations as seen in Fig. 5.10. In contrast, the transition to resolved content is moved upstream for DDES II, which yields smaller turbulent eddies and a more broadband spectral signature centred at higher frequency.

In the case of the longer and more complete DDES I simulation, data were also sampled at every physical time step (sampling frequency of 1 MHz) at chosen points on

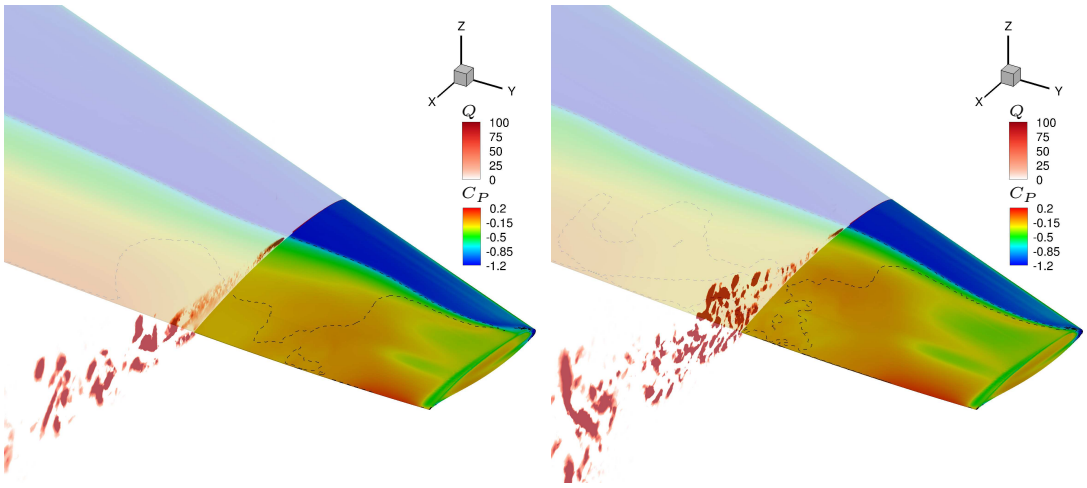

(a) DDES I at $t = 0.04325\,\mathrm{s}$ **(b)** DDES II at $t = 0.06725\,s$

Figure 5.14: Instantaneous surface pressure coefficient and a representative slice at 86% semi-span showing dimensionless Q-criterion during a low-lift phase. Dashed lines denote the reverse-flow region.

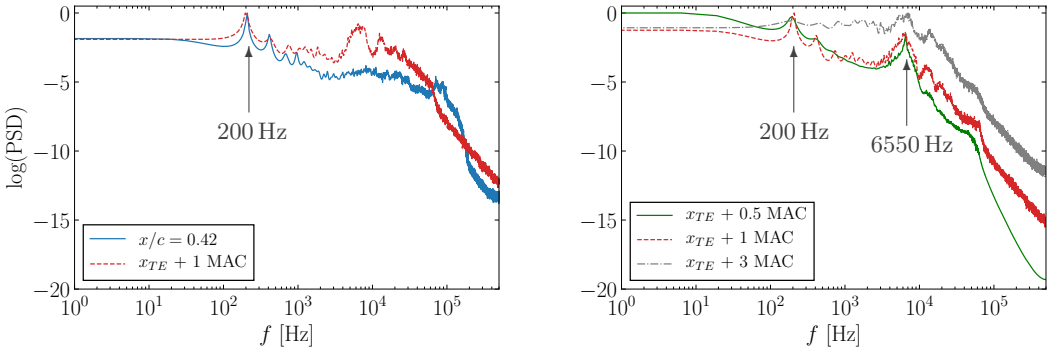

(a) Static pressure **(b)** Streamwise velocity

Figure 5.15: Normalised power spectral density data of pressure and velocity fluctuations at chosen points (specifically at 77% semi-span and chordwise positions as indicated in legend) from DDES I at $\alpha = 3.1°$.

the wing surface and in the wake to scrutinise resolved turbulent content. Normalised PSD data of pressure and streamwise velocity fluctuations are presented in Fig. 5.15 showing two main features. First, all spectra both on the surface and in the wake are characterised by the dominant 200 Hz shock-oscillation frequency. Second, spectra in the wake have the highest energy content within the medium-frequency unsteadiness bump centred at 6550 Hz due to smaller-scale turbulent fluctuations, better resolved from the streamwise velocity data. It should be noted that although these spectra show higher PSD levels farther downstream, this is an effect of normalising the PSD graphs. Indeed, the highest levels of unsteadiness can be found farther upstream near the shock oscillation. This phenomenon is studied from a modal analysis of the field data and is linked to a Kelvin–Helmholtz-type (K–H) instability, as discussed in Section 5.4.3.

This conventional analysis has shown that the DDES approach is capable in resolving the shock-buffet dynamics near onset with very good agreement at model scale between DDES II and the experimental data. There is no considerable difference in the buffet-onset angle of attack between the model-scale and full-scale simulations. These observations motivate the use of modal analysis techniques on the numerical datasets to enable deeper analysis and comparison with the DPSP data.

5.4 Data-Based Modal Analysis

The experimental analysis in Chapter 4 has identified two coexisting phenomena—a low-frequency shock unsteadiness along the whole span centred at approximately 70 Hz (corresponding to $St \approx 0.07$), which propagates pressure in the inboard direction towards the root, together with higher frequency outboard-running perturbations at > 200 Hz (corresponding to $St > 0.22$) confined to the outer wing region. Previous work employing numerical linearised-aerodynamics analysis by Timme & Thormann (2016) similarly pointed out distinct flow phenomena. Specifically, forced wing vibration excited a low-frequency response, dominated by shock unsteadiness but with low sensitivity to angle-of-attack increments in the vicinity where self-sustained flow unsteadiness is first observed, and higher-frequency peaks typical for swept-wing shock buffet that are greatly amplified around critical conditions. The latter has been linked to globally unstable and weakly damped eigenmodes (Timme, 2020), whereas the former bears similarity to a long-wavelength inboard-running eigenmode identified for a simplified infinite-wing geometry (Crouch *et al.*, 2019). Nevertheless, while some consensus has emerged in recent years concerning the swept-wing shock-buffet modes and associated buffet cells (for instance Iovnovich & Raveh (2012), Dandois (2016) and Ohmichi *et al.* (2018)) questions remain in relation to the lower-frequency behaviour.

In this spirit, the time-accurate simulations are further analysed using data-based modal analysis techniques including POD and DMD. The aim is to provide a spatio-temporal representation of the dominant coherent flow features allowing quantitative comparison between CFD and experiment. The discussion starts with an analysis of surface pressure data both from experimental DPSP and numerical DDES. This is followed by an analysis over the whole computational domain. Modes related to shock buffet together with coherent medium-frequency shear-layer structures are identified from the numerical data whereas modes pertaining to the lower-frequency behaviour are exclusive to the experimental data.

5.4.1 Proper Orthogonal Decomposition Surface Analysis

A POD analysis of surface pressure data is conducted on four datasets: (i) experimental DPSP data, (ii) DDES I ($0.0305 \leq t \leq 0.121$ s), (iii) DDES II ($0.05 \leq t \leq 0.1$ s) and (iv) DDES FS ($0.18 \leq t \leq 1.19$ s).

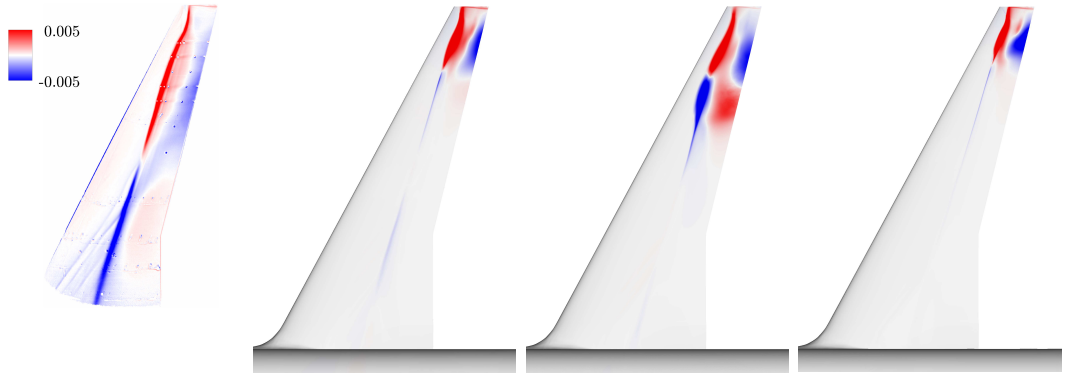

(a) DPSP at $\alpha = 3.3°$ **(b)** DDES I ($0.0305 \leq t \leq 0.121\,\mathrm{s}$) **(c)** DDES II ($0.05 \leq t \leq 0.1\,\mathrm{s}$) **(d)** DDES FS ($0.18 \leq t \leq 1.19\,\mathrm{s}$)

Figure 5.16: Spatial component of dominant POD mode 1 from DPSP and DDES surface pressure coefficient data, coloured by spatial amplitudes. Numerical results at $\alpha = 3.1°$.

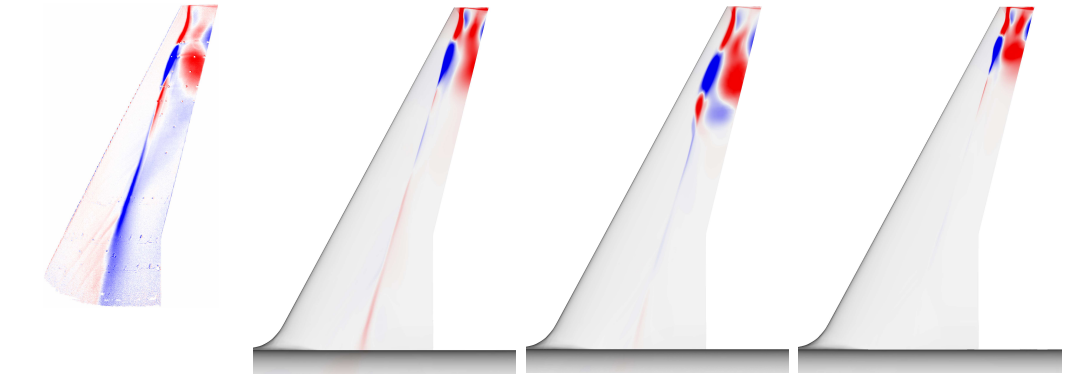

(a) DPSP at $\alpha = 3.3°$ **(b)** DDES I ($0.0305 \leq t \leq 0.121\,\mathrm{s}$) **(c)** DDES II ($0.05 \leq t \leq 0.1\,\mathrm{s}$) **(d)** DDES FS ($0.18 \leq t \leq 1.19\,\mathrm{s}$)

Figure 5.17: Spatial component of a less dominant POD mode from DPSP (mode 8) and DDES (mode 2) surface pressure coefficient data. Contour levels correspond to Fig. 5.16.

The spatial component of dominant POD modes both from experimental and numerical surface pressure coefficient data is depicted in Fig. 5.16, highlighting the dominant flow features responsible for the largest fluctuations. Each POD mode has unit norm and the highest spatial amplitudes occur along the unsteady shock together with the region farther downstream. The spatial amplitudes represent positive or negative perturbations around the mean pressure value, depending on their sign and the corresponding temporal coefficient (there are as many temporal coefficients as snapshots denoting the time evolution of each POD mode at every spatial point). To illustrate, at a positive temporal coefficient, regions of higher and lower pressure are depicted by positive (red) and negative (blue) spatial amplitudes, respectively. Focussing on the experimental data, the shock sits upstream of its mean position on the outboard wing inducing flow separation. Farther inboard, the shock is downstream and the flow

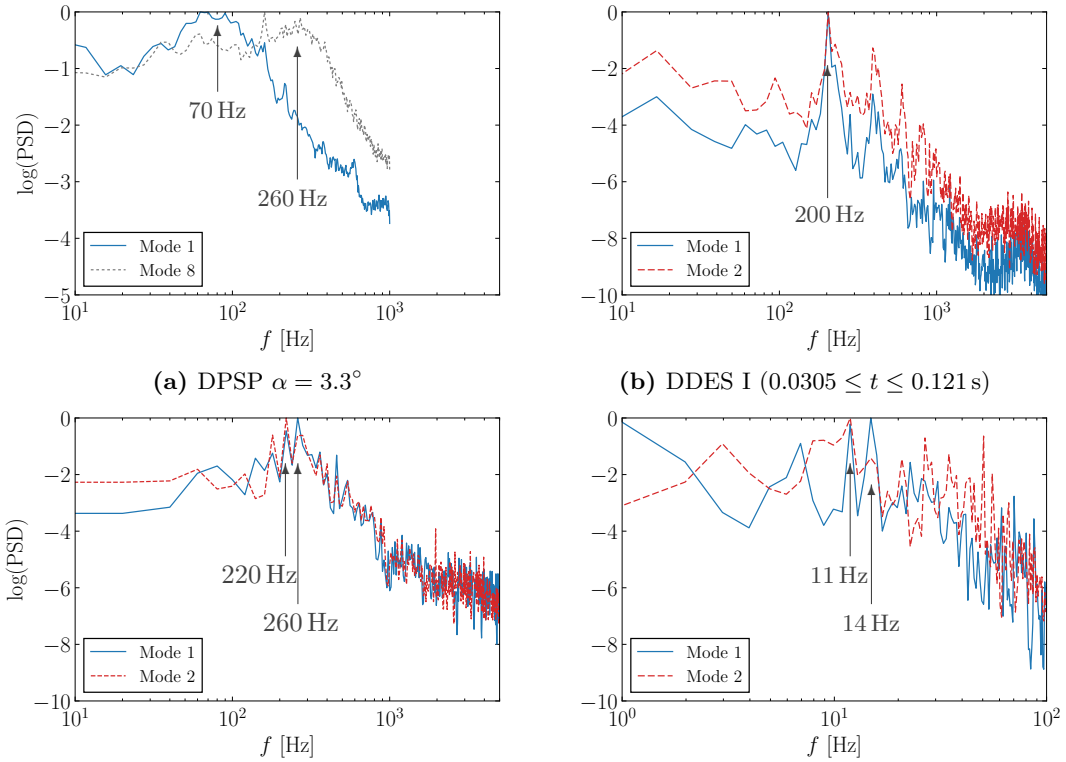

(a) DPSP $\alpha = 3.3°$ **(b)** DDES I ($0.0305 \leq t \leq 0.121\,\mathrm{s}$)

(c) DDES II ($0.05 \leq t \leq 0.1\,\mathrm{s}$) **(d)** Full-scale DDES ($0.18 \leq t \leq 1.19\,\mathrm{s}$)

Figure 5.18: Power spectral density data of POD temporal coefficients for modes shown in Figs. 5.16 and 5.17. Note different frequency axis for full-scale simulation.

remains attached. The dominant mode from DPSP corresponds to a low-frequency inboard-running behaviour. The unsteadiness obtained numerically is confined to the outboard region, with that from DDES II covering a wider spanwise region, in good agreement with the standard deviation in Fig. 5.6. In contrast to the experimental mode, the numerical modes have an outboard-running behaviour as shown later from the supporting DMD phase analysis. In the case of the full-scale simulation, the shock oscillates over smaller chordwise distances and emanates from slightly farther outboard than at model scale. This corroborates the smaller fluctuations in lift coefficient previously shown in Fig. 5.9. Another example of a resulting POD mode is depicted in Fig. 5.17 from which similar observations can be made. Experimentally, since several intermediate modes are related to the wing structural response, as explained in Section 4.4.1, mode 8 is shown instead in Fig. 5.17a—the first one, ranked by POD energy, to capture the shock rippling on outboard sections and causing pockets of shock-induced separation that follow the upstream shock excursions. In the case of numerical data, the spatial components of mode 2 are shown, with DDES II resulting in remarkable agreement with the experimental data.

To obtain the temporal behaviour of these modes, PSD data based on the temporal coefficients corresponding to the modes presented in Figs. 5.16 and 5.17 are

shown in Fig. 5.18. The PSD data for the numerical signal were computed using Burg's method (Burg, 1967) whilst Welch's method (Welch, 1967) was used for the longer DPSP signal. In all cases, the spectra were normalised by their respective maximum value. Considering the DPSP dataset, mode 1 is centred at lower frequencies around 70 Hz, typical of the inboard-running low-frequency shock unsteadiness, whereas mode 8 shifts to a higher frequency above 200 Hz that is characteristic of the outboard-propagating shock-buffet unsteadiness. Temporal fluctuations of modes 1 and 2 from DDES I show a clear peak at 200 Hz, matching the primary peak obtained from the lift fluctuations in Fig. 5.11a, while lacking the broadband content and the 70 Hz observed experimentally. The broadband content appears in the PSD data from DDES II, peaking at 220 Hz ($St = 0.23$) and 260 Hz ($St = 0.28$) and lying within the range of the spectral bump from the lift fluctuations. Together with the observed spatial variations in Figs. 5.16c and 5.17c, the broadbandedness can be explained. Similar to the spatial amplitudes, the agreement with the experimental mode 8 is striking. Focusing on the full-scale simulation, the frequency spectrum is less defined due to a shorter time signal (smaller number of buffet cycles) and irregular nature. However, peaks are visible at 11 Hz ($St = 0.23$) and 14 Hz ($St = 0.29$), within the range of the spectral bump of the PSD of lift coefficient fluctuations in Fig. 5.11b.

5.4.2 Dynamic Mode Decomposition Surface Analysis

DMD was applied to the surface pressure snapshots to extract dynamic information and to isolate the flow phenomena based on frequency. Whilst in POD the modes are naturally ranked by the fluctuation energy, DMD mode sorting is less obvious. Scaled spectral coefficients are computed as in Section 4.4.2, such that the time evolution of each DMD mode is taken into account, promoting growing and slowly-decaying modes, whilst reducing peaks of spurious quickly-decaying modes (Tu *et al.*, 2014). The resulting DMD spectra from the experimental DPSP and DDES are shown in Fig. 5.19 whereby the spectral coefficients are normalised by the maximum value, excluding that of the mean-flow mode. The dominant DMD mode from DDES I has a frequency of 197 Hz ($St = 0.22$) whereas that from DDES II is 278 Hz ($St = 0.30$). In the latter case, the spectrum is more broadband and DMD modes at 199 Hz ($St = 0.22$) and 237 Hz ($St = 0.25$) also have relatively high contributions. These three modes look very similar when visualised. The dominant DMD mode from DDES FS has a frequency of 11 Hz ($St = 0.23$). In the case of the experimental DPSP data, the spectrum is broadband with a large number of modes since the number of input snapshots is higher. The dominant modes lie within the low-frequency shock unsteadiness range which is not captured by the DDES. However, visualisation of the modes within the higher-frequency range ($0.2 \leq St < 0.5$) reveals the highest contribution along the outboard shock with propagation towards the tip, similar to the simulations, as shown next.

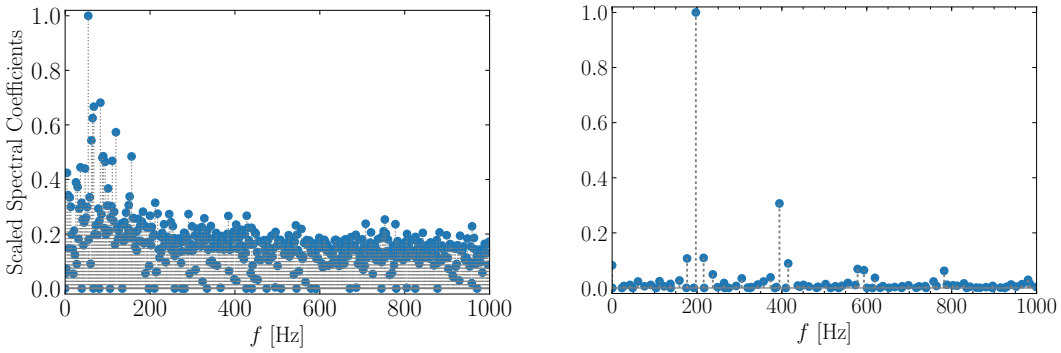

(a) DPSP at $\alpha = 3.3^\circ$

(b) DDES I ($0.0305 \leq t \leq 0.121\,\mathrm{s}$)

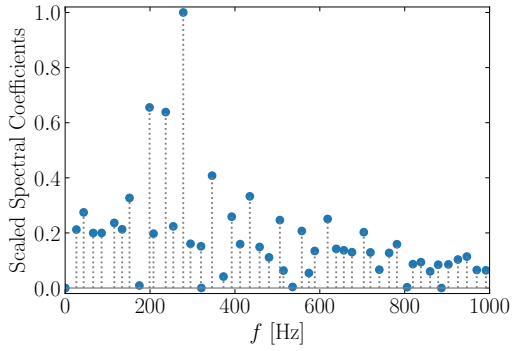

(c) DDES II ($0.05 \leq t \leq 0.1\,\mathrm{s}$)

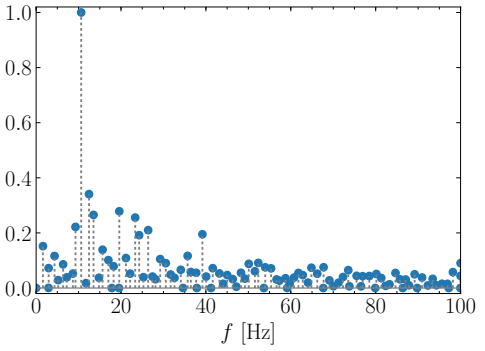

(d) Full-scale ($0.18 \leq t \leq 1.19\,\mathrm{s}$)

Figure 5.19: DMD spectrum for surface pressure snapshots from DPSP and DDES.

Each projected DMD mode is a complex-valued spatial field scaled to unit norm and the spatial amplitudes of both real and imaginary parts are depicted in Figs. 5.20 through 5.23. The corresponding magnitude and phase angle at each spatial point are also included. It is evident that the DMD modes with the highest spectral coefficient are very similar to POD modes 1 and 2, presented previously in Figs. 5.16 and 5.17. Variations between the real and imaginary parts provide information regarding the pressure propagations and clarify the dynamics at a single frequency of interest. This is the added insight that DMD provides to the analysis. The magnitude of the complex number highlights the intensity of pressure perturbations while the phase variation indicates the direction of propagation. A comparison of the magnitude of the dominant DMD modes in Figs. 5.20c through 5.23c immediately elucidates pressure perturbations that are confined closer to the wing tip together with a smaller shock oscillation at full scale. The shock dynamics are similar in both simulations and the experiment, with the phase angle gradually decreasing in the spanwise direction along the shock (outboard of 75% semi-span in DDES I and 66% semi-span in DDES II), corresponding to pressure propagation towards the wing tip. Apparent discontinuities in the phase angle are due to phase wrapping and have no physical meaning. A phase difference of approximately π between the shock foot and the trailing edge corroborates the flow physics implied by the opposite signs of the POD spatial amplitudes in these regions, i.e., trailing-edge separation occurs when the shock is upstream of its mean position.

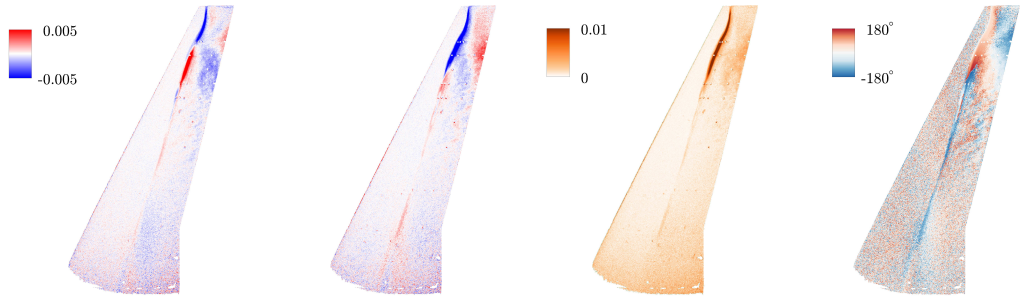

(a) Real part **(b)** Imaginary part **(c)** Magnitude **(d)** Phase angle

Figure 5.20: Dominant DMD mode from experimental DPSP ($\alpha = 3.3°$) with $f = 245\,\mathrm{Hz}$.

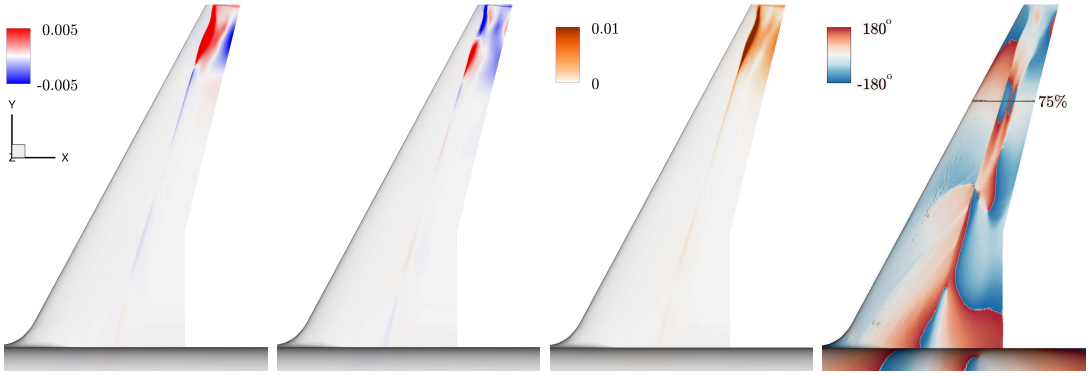

(a) Real part **(b)** Imaginary part **(c)** Magnitude **(d)** Phase angle

Figure 5.21: Dominant DMD mode from DDES I ($0.0305 \leq t \leq 0.121\,\mathrm{s}$) with $f = 197\,\mathrm{Hz}$.

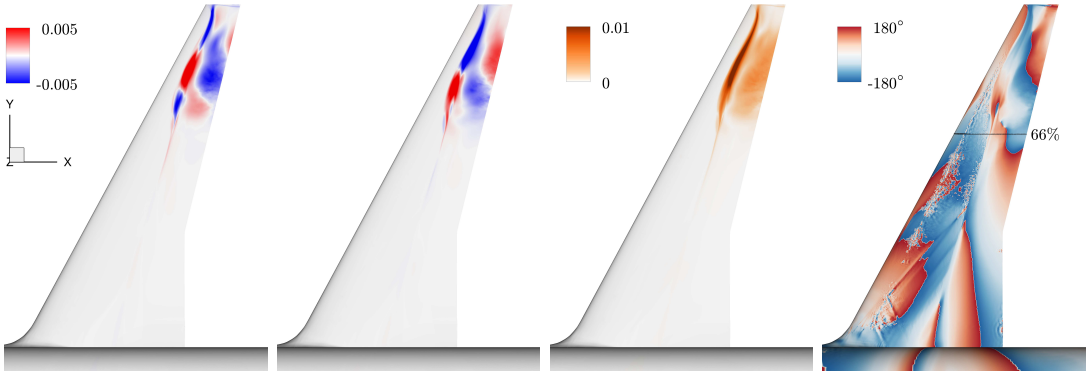

(a) Real part **(b)** Imaginary part **(c)** Magnitude **(d)** Phase angle

Figure 5.22: Dominant DMD mode from DDES II ($0.05\,\mathrm{s} \leq t \leq 0.1\,\mathrm{s}$) with $f = 278\,\mathrm{Hz}$.

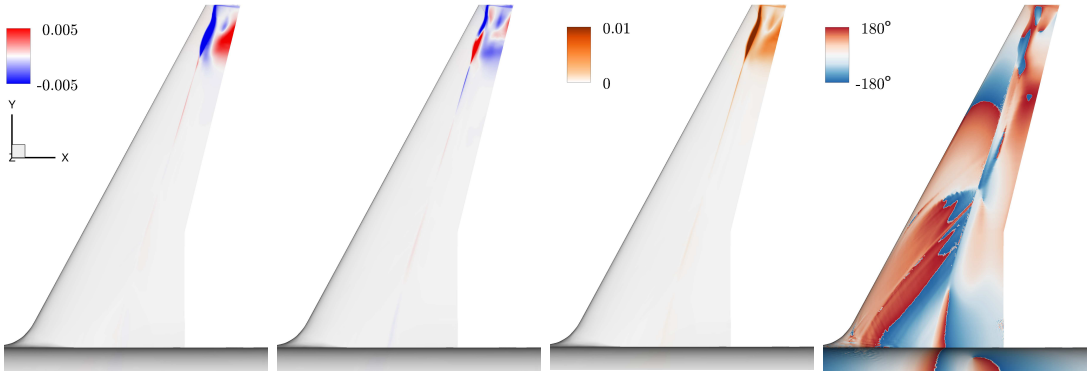

(a) Real part **(b)** Imaginary part **(c)** Magnitude **(d)** Phase angle

Figure 5.23: Dominant DMD mode from DDES FS ($0.18 \leq t \leq 1.19\,\mathrm{s}$) with $f = 11\,\mathrm{Hz}$.

5.4.3 Flow-Field Analysis

Complete field data from the longer DDES I simulation was decomposed using both POD and DMD. Figure 5.24 depicts the spatial structures of dominant modes from pressure coefficient data, corresponding to the surface pressures shown in Figs. 5.16b and 5.21. Very similar spatial structures were obtained from the POD mode and the real part of the DMD mode with the highest spectral coefficient of 197 Hz. These depict the radiation of pressure from the trailing-edge separation with opposite-signed spatial amplitude relative to the shock foot. Variations between the real and imaginary parts of the DMD mode highlight the propagation of buffet cells towards the wing tip and into the wake. Equivalent modes from streamwise velocity and momentum data were also analysed highlighting flow separation as a result of an upstream shock movement and pressure perturbations that extend into the wake. PSD data of the temporal coefficients of the dominant POD modes are presented in Fig. 5.26a showing a peak at 210 Hz, approximately the same as that obtained from surface data. Slight differences are due to varying sampling rates. Modal analyses of the field data sampled at 20 kHz give the same dominant modes as those shown with a lower sampling rate.

However, the highly-sampled segment, cf. Table 5.3, reveals additional modes constituting coherent structures in the shear layer as visualised in Fig. 5.25. These were captured by POD modes 39 and 40 which have a similar spatial component but are temporally shifted (90° out-of-phase), together describing a downstream convection. This propagation is represented by the real and imaginary parts of a particular DMD mode with a frequency of 6549 Hz. The temporal components of POD modes 39 and 40 highlight a higher-frequency bump peaking at 6460 Hz, as shown in Fig. 5.26b. This frequency peak from the modal analysis is in agreement with the point-data analysis previously presented in Fig. 5.15. Although several modes capture eddies that span the whole frequency range up to the Nyquist frequency, their spatial structures are incoherent. In contrast, modes with coherent structures have a common peak within

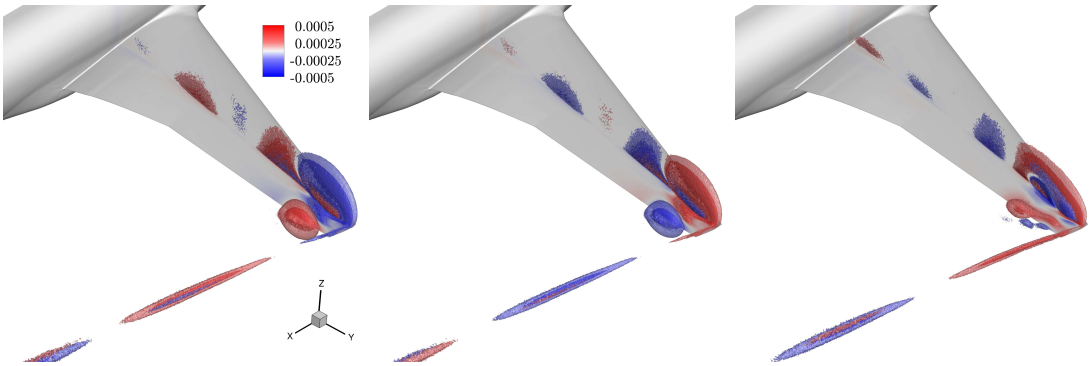

(a) POD mode 1 **(b)** DMD mode ($\Re$) 197 Hz **(c)** DMD mode ($\Im$) 197 Hz

Figure 5.24: Dominant modes from DDES I ($0.0305 \leq t \leq 0.121$ s) field pressure coefficient data visualised by iso-surfaces of the spatial amplitudes.

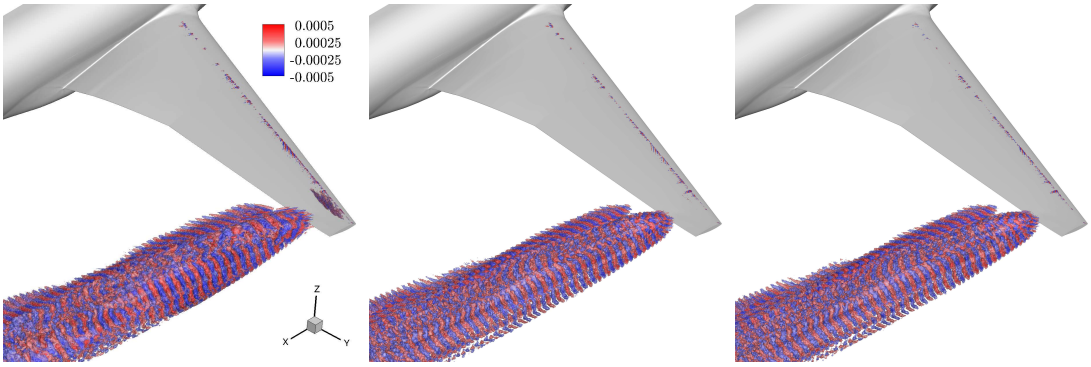

(a) POD mode 39 **(b)** DMD mode ($\Re$) 6549 Hz **(c)** DMD mode ($\Im$) 6549 Hz

Figure 5.25: Coherent mode identified from streamwise velocity data u of DDES I ($0.0305 \leq t \leq 0.121$ s) visualised by iso-surfaces of the spatial amplitudes.

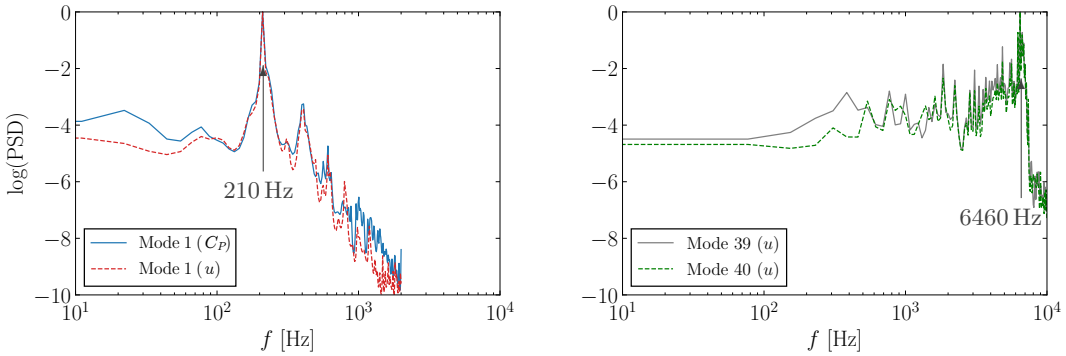

(a) $f_s = 4$ kHz ($0.0305 \leq t \leq 0.121$ s) **(b)** $f_s = 20$ kHz ($0.081 \leq t \leq 0.94$ s)

Figure 5.26: Normalised PSD data of POD temporal coefficients of the shock-buffet and wake modes from field pressure coefficient and streamwise velocity data of DDES I.

this frequency bump. Slices through the iso-surfaces at 77% semi-span of the modes presented in Fig. 5.25 are shown in Fig. 5.27. Both their spatial structures and fre-

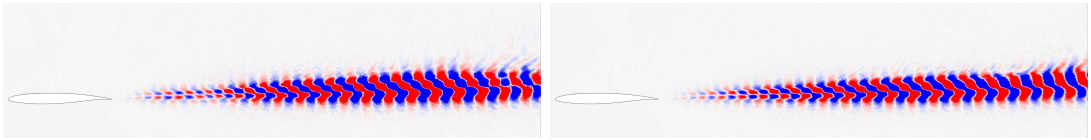

(a) POD mode 39 **(b)** DMD mode ($\Re$) at 6549 Hz

Figure 5.27: Slice at 77% semi-span through iso-surfaces of shear-layer instability modes.

quency content bear similarity with a Kelvin–Helmholtz-type instability in the shear layer. Similar observations were reported on aerofoils and wings in buffet flow conditions (Sartor *et al.*, 2014; Dandois, 2016; Zauner *et al.*, 2019).

5.5 Summary of Numerical Analysis

Scale-resolving delayed detached-eddy simulations have been conducted and directly compared with the unique experimental dynamic pressure-sensitive paint dataset to gain more insight into the flow physics governing shock buffet onset. Efforts have been focused in the vicinity where flow unsteadiness is first observed, filling a gap in the literature and helping to clarify this unsteady edge-of-the-envelope flow phenomenon. Such flow conditions pose a challenge to simulate numerically due to separating and reattaching shallow shear layers and therefore two different subgrid length-scale definitions were scrutinised. In this respect, it has been shown how a vorticity-informed definition yields an earlier transition from modelled to resolved turbulence, when compared to standard delayed detached-eddy simulation, and is essential for more truthfully reproducing the experimental data. Furthermore, data-based modal identification techniques were successful in the analysis of these massive datasets and enabled direct quantitative comparison between experimental and numerical data based on salient modal features. At model scale, even though the vorticity-sensitive simulation results in remarkable agreement with the experimental dataset overall, the lower-frequency shock unsteadiness behaviour is unique to the wind-tunnel test and does not feature in the fully developed shock-buffet phase of the fluid-only numerical analyses. Having analysed both the experimental and numerical datasets, this discrepancy is discussed in Chapter 6. Shock-buffet onset is only slightly delayed at flight conditions and its inherent dynamics were found to be similar to sub-scale experimental data when employing delayed detached-eddy simulation with the classical subgrid length scale.

Chapter 6

Discussion

The key finding from the experimental analysis in Chapter 4 is the identification of two coexisting, but distinct, phenomena on the clean wing upper surface in shock-buffet conditions. The first is low-frequency shock unsteadiness in a Strouhal number range between 0.05 and 0.15, centred at $St = 0.07$. This unsteadiness is observed both well below structural buffeting onset, as identified from a root strain gauge, in attached flow conditions, and beyond onset, with pressure propagating predominantly in the inboard direction along a large spanwise region occupied by the unsteady shock wave. The same observation holds true for the configurations with vane vortex generators which do not suppress this unsteadiness. The second phenomenon is the presence of higher-frequency outboard-running waves confined to the outboard wing that are exclusive to post-onset conditions. These have a broader spectral signature, between Strouhal numbers of 0.2 and 0.5, closely resembling the buffet-cell behaviour reported for swept-wing shock buffet for the past few years. The numerical analysis in Chapter 5 has focused on this higher-frequency cellular pattern having a more localised spanwise extent, as the low-frequency shock unsteadiness behaviour does not feature in the fully developed buffet phase of the fluid-only numerical simulations. These important observations are the subject of the following discussion which provides further context based on the literature and compares and contrasts the two phenomena as characterised herein.

6.1 Shock Motion Analysis

The complex shock motion taking place around shock-buffet onset conditions motivated a detailed quantitative assessment to establish the pertinent propagation speeds. Pressure propagation along the shock was characterised from the experimental DPSP data by means of a cross-spectrum analysis. This approach has previously been used in the shock-buffet context to compute propagation speeds from unsteady transducer signals (see for example Dandois (2016) and Koike *et al.* (2016)). Herein, the cross-spectral analysis is performed for several flow conditions critically exploiting the much

wider coverage of the DPSP dataset when compared to discrete transducers in previous studies. A semi-automated process was devised to acquire pressure signals along the shock at several representative locations. Dominant POD modes related to the aerodynamics (rather than the structural vibration of the wind-tunnel model) were used to reconstruct pressure snapshots with reduced measurement noise, facilitating extraction of the shock position. The shock position was taken as the chordwise pixel having the highest pressure deviation from the time-averaged value over the longest period of time, at 14 spanwise stations between $\eta = 0.43$ and $\eta = 0.99$ with intervals of $\Delta\eta \approx 0.04$. Cross-spectra were computed between each pressure time series and a reference signal, taken at $\eta \approx 0.59$, from which the magnitude-squared coherence, $C_{xy}(f)$, and the phase angle, $\phi_{xy}(f)$, were determined.

Figure 6.1 illustrates the coherence levels of the signals along the shock at two focus angles of attack in this study, $\alpha = 2.9°$ and $3.3°$. High levels of coherence are obtained within the low-frequency spectral bump, corresponding to the shock unsteadiness. Such cross-correlation between the signals indicates that pressure is propagating along the shock in the spanwise direction. This is evident from the linear phase variation along the shock, depicted in Fig. 6.2 at four angles of attack, including a low angle of attack below structural buffeting onset, $\alpha = 1.6°$, and three angles of attack around onset. From Eq. (2.11), a positive linear slope indicates a negative propagation speed, that is, pressure propagates inboard towards the root (Dandois, 2016). This inboard-running wave is present even in attached flow conditions at $\alpha = 1.6°$, before the model starts buffeting due to unsteady flow. The slope is linear between $\eta = 0.55$ and 0.90, the same spanwise extent with high unsteadiness along the shock in Fig. 4.7a. This inboard propagation continues to occur with increasing angle of attack and reaches farther inboard as the whole shock trace becomes unsteady. However, the slope of the phase variation reverses around structural buffeting onset, beyond $\alpha_b = 2.7°$, between $\eta = 0.87$ and the wing tip, implying outboard propagation. This simultaneous inboard and outboard pressure propagation along the shock becomes clear at $\alpha = 2.9°$, supporting the observations from instantaneous pressure snapshots in Fig. 4.14. The angles of attack at which the slope reverses coincide with increased buffeting levels measured by the strain gauge. Moreover, the spanwise location where the outboard propagation emanates, $\eta = 0.87$, corresponds to the outboard region of the localised separation, highlighted in Fig. 4.7h. The two selected frequencies in Fig. 6.2 were chosen due to high coherence levels in Fig. 6.1. However, it should be noted that similar phase plots are obtained at the frequencies within the low-frequency shock-unsteadiness bump, between 50 and 140 Hz, suggesting the same pertinent flow physics.

This spanwise shock motion analysis was extended to all Mach numbers between $M = 0.70$ and 0.84, focusing on the angles of attack around structural buffeting onset. Analysis employing the DPSP data was critical since transducer data along the shock at onset conditions was only possible between $M = 0.78$ and 0.82, with the mean

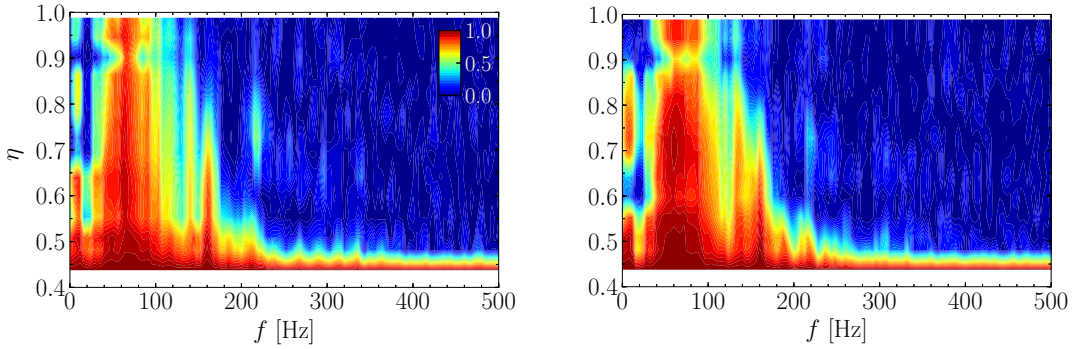

(a) $\alpha = 2.9°$ **(b)** $\alpha = 3.3°$

Figure 6.1: Magnitude-squared coherence levels of pressure signals along shock for two angles of attack beyond structural buffeting onset at $M = 0.80$.

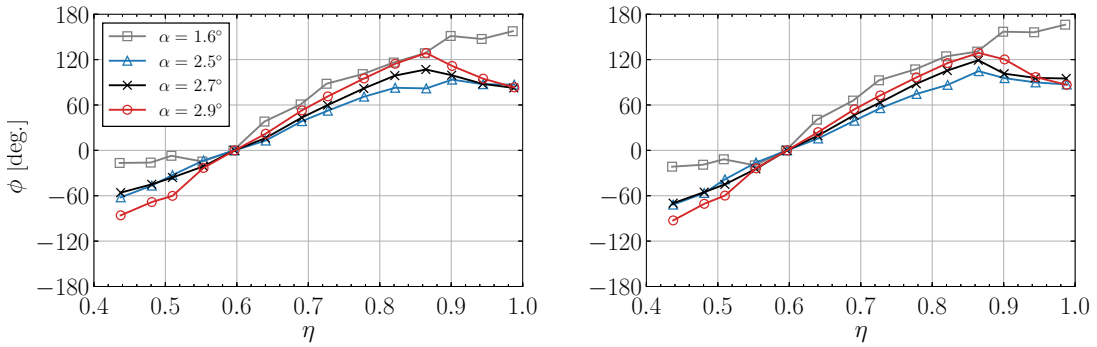

(a) $f = 72\,\text{Hz}$ **(b)** $f = 80\,\text{Hz}$

Figure 6.2: Phase angle variation along shock at selected frequencies of low-frequency shock unsteadiness at pre- and post-onset conditions at $M = 0.80$.

shock position being upstream of the most upstream transducers at $M = 0.76$, and too far aft at $M = 0.84$. The key flow phenomena described at $M = 0.80$ were observed throughout the Mach number range. Essentially, inboard-running pressure propagation along the shock occurs below onset conditions. As the angle of attack is increased, reaching structural buffeting onset, the direction of propagation is reversed near the outboard position of localised flow separation close to the wing tip. Figure 6.3 shows the relative standard deviation of surface pressure computed between two angles of attack, at structural buffeting onset and just above, together with the phase angle variation with span at 80 Hz for a number of angles of attack around buffeting onset, throughout the range of Mach numbers from $M = 0.74$ to 0.82. The common attribute is the formation of localised flow separation on the outboard wing at each respective buffet onset angle of attack, α_b, which pushes the shock upstream, as depicted by elevated unsteadiness levels in red. This region becomes wider at higher Mach number, since the shock-induced separation bubble merges with the trailing-edge separation over a larger spanwise extent, where the local Mach number is highest. This influence of

Mach number on the reversed-flow region was also observed previously for the same wing (Sartor & Timme, 2016). Furthermore, the phase plots reveal that outboard propagation emanates from the outer part of the separated region (denoted by the dashed vertical lines) towards the wing tip, both at onset (black crosses) and post-onset (red circles). The reversal in propagation direction occurs farther inboard as the Mach number increases.

Similar plots are presented in Fig. 6.4 at $M = 0.70$ and 0.84, the lowest and highest Mach numbers, respectively, which are characterised by distinct flow topologies. At $M = 0.70$, a very steep rise in buffeting levels takes place between $\alpha = 5.8°$ and 5.9°, as the shock moves upstream towards the region of forced boundary layer transition. The shock is well forward, even within the laminar region at times, with the strong adverse pressure gradient causing a separation bubble, exacerbated by the shock. Visualisation of pressure snapshots reveals large-scale separated flow structures convecting downstream and outboard. The long bubble-type separation, from almost the leading edge up to around mid-chord, is manifested as a region of high unsteadiness in Fig. 6.4a. The pressure distributions presented in Fig. 6.5 at two spanwise stations for three angles of attack around buffeting onset corroborate this observation. Considering the pressure distribution at $\alpha_b = 5.8°$ and $\eta = 0.73$, a shock-induced separation bubble forms behind the shock between $x/c = 0.32$ and 0.60, indicated by diverging pressure with angle of attack in Fig. 6.5a. Slightly incrementing the angle of attack to $\alpha = 5.9°$, this flow feature becomes more pronounced, while farther outboard at $\eta = 0.93$, the shock shifts forward and a long bubble-type separation forms from the laminar region, as depicted in Fig. 6.5b. This flow topology is reminiscent of low-speed stall cells, whereby a negative lift-curve slope is required to amplify the spanwise variation of lift (see for example Rodríguez & Theofilis (2011) and Spalart (2014)). In this case, although the overall lift coefficient is still increasing between these two angles of attack, a negative sectional lift-curve slope is expected at the outboard sections where the massive separation occurs. A link between buffet cells and stall cells has been reported by Plante *et al.* (2020). In contrast at $M = 0.84$, separation can be observed over a wider spanwise area, with the S-shaped shock curvature occurring farther inboard at around $\eta = 0.50$. Even though the surface flow topologies at $M = 0.70$ and 0.84 have contrasting characteristics, the phase angle variation along the shock still reveals an inboard-running shock unsteadiness which reverses direction and propagates outboard from the outer edge of the separated region, as observed at the other Mach numbers between $M = 0.74$ and 0.82.

The propagation speed along the shock was computed from a linear fit of the phase angle variation with span, using Eq. (2.11). The results at various Mach numbers are summarised in Table 6.1, whereby U_∞ denotes the freestream velocity whilst the propagation speed U_p is computed at $f = 80\,\mathrm{Hz}$ ($St \approx 0.09$), between $\eta = 0.51$ and just inboard of the location where the slope reverses. This frequency was selected due to

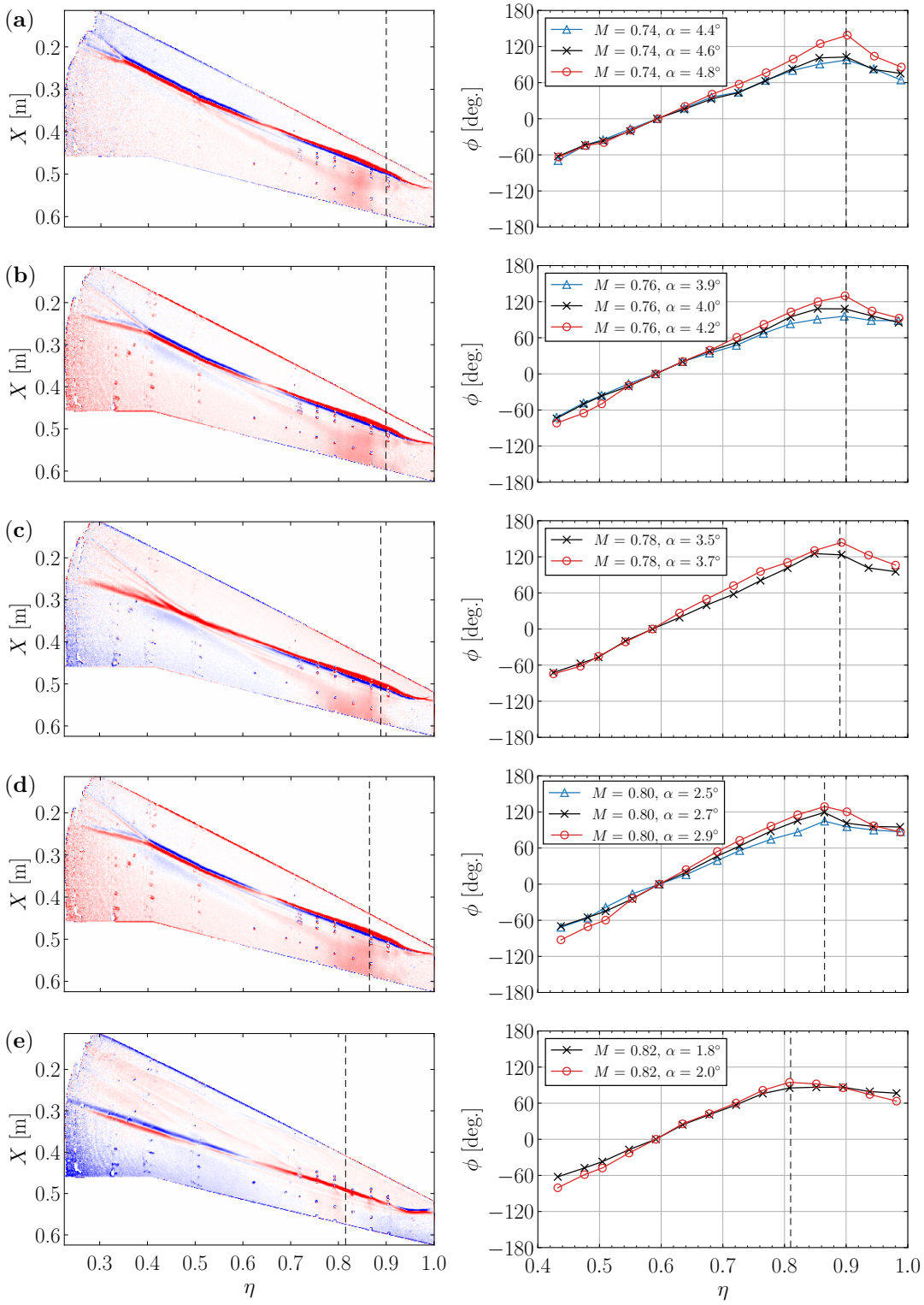

Figure 6.3: Relative standard deviation around structural buffeting onset (left column) and phase angle variation with span along shock (right column). The images are coloured from −500 Pa (blue) to +500 Pa (red). The phase plots are computed at 80 Hz and denoted by blue triangles (△) pre-onset, black crosses (×) at onset and red circles (○) post-onset. The dashed lines represents the location at which the reversal in propagation direction takes place. (**a**) $M = 0.74$, $\sigma_{\alpha=4.8^\circ} - \sigma_{\alpha_b=4.6^\circ}$ (**b**) $M = 0.76$, $\sigma_{\alpha=4.2^\circ} - \sigma_{\alpha_b=4.0^\circ}$ (**c**) $M = 0.78$, $\sigma_{\alpha=3.7^\circ} - \sigma_{\alpha_b=3.5^\circ}$ (**d**) $M = 0.80$, $\sigma_{\alpha=2.9^\circ} - \sigma_{\alpha_b=2.7^\circ}$ and (**e**) $M = 0.82$, $\sigma_{\alpha=2.0^\circ} - \sigma_{\alpha_b=1.8^\circ}$.

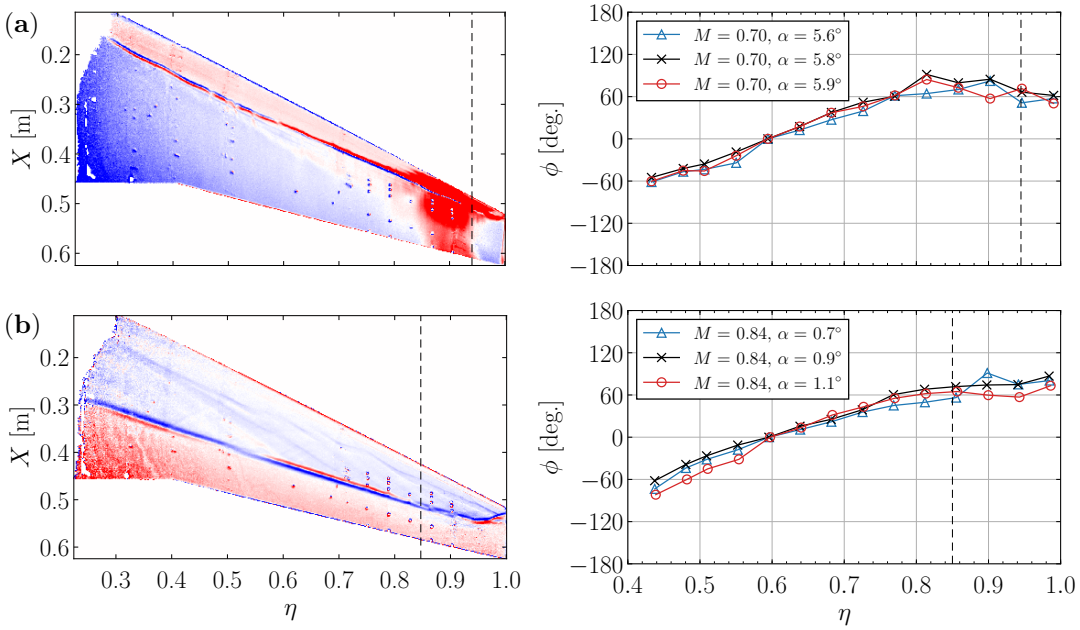

Figure 6.4: Relative standard deviation around structural buffeting onset and phase angle variation computed at 80 Hz along shock at $M = 0.70$ and 0.84. The same symbol key of Fig. 6.3 is used. (**a**) $M = 0.70$, $\sigma_{\alpha=5.9^\circ} - \sigma_{\alpha_b=5.8^\circ}$ and (**b**) $M = 0.84$, $\sigma_{\alpha=1.1^\circ} - \sigma_{\alpha=0.7^\circ}$.

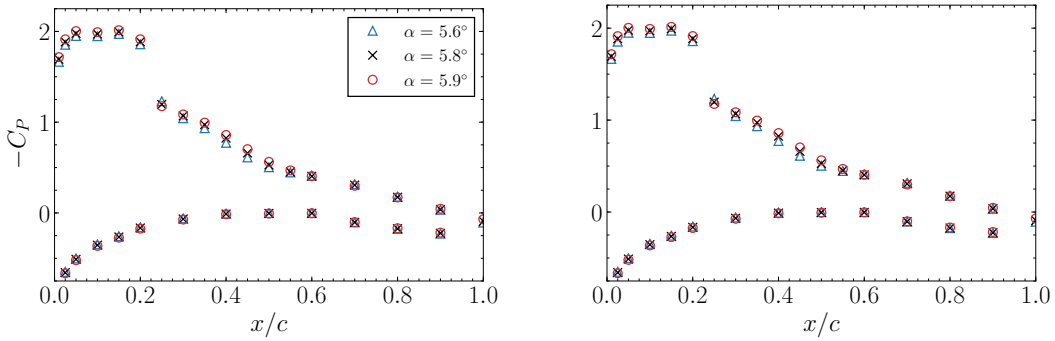

(a) $\eta = 0.73$ **(b)** $\eta = 0.93$

Figure 6.5: Pressure coefficient distributions at two outboard spanwise stations around structural buffeting onset at $M = 0.70$.

high coherence along the span. However, it should be noted that similar phase plots with a linear variation along the swept shock were obtained at all frequencies within the low-frequency shock-unsteadiness bump between 50 and 140 Hz. This implies that these frequencies are related to the same propagative phenomenon, having a similar wavelength, since the propagation speed increases linearly with frequency. The wavelength was computed as $l = U_p/f$, and, in order to reduce the variance in the value given in Table 6.1, the average wavelength value was computed for each resulting U_p at each frequency within the low-frequency unsteadiness range between 50 and 140 Hz, at intervals of $\Delta f = 4$ Hz. The latter is the frequency resolution of the signal processing

M	α (deg.)	U_p (m/s)	U_p/U_∞	l (m)	l/b
0.74	4.8	−68	−0.28	0.87	0.80
0.76	4.2	−68	−0.27	0.81	0.75
0.78	3.9	−65	−0.26	0.80	0.73
0.80	2.9	−68	−0.26	0.84	0.77
0.82	2.0	−66	−0.25	0.86	0.79

Table 6.1: Low-frequency shock unsteadiness characterisation for a range of Mach numbers. The propagation speed U_p is calculated at $f = 80\,\text{Hz}$ whilst the wavelength value l is averaged over the frequency range between 50 and 140 Hz.

described in Section 2.1.2. The summarised results in Table 6.1 show that the propagation speed at $St \approx 0.09$ is similar between $M = 0.74$ and 0.82, at around $-0.26\,U_\infty$, where the negative sign implies an inboard-running propagation. This corresponds to a wavelength of $l \approx 0.8\,b \approx 3\,\text{MAC}$, where b denotes the semi-span.

This low-frequency inboard-running propagation of pressure along the shock occurs even at low incidence, as previously highlighted in Fig. 6.2. With an increase in angle of attack and the formation of a localised separated flow region, this unsteadiness reverses direction and propagates outboard between the separated region and the wing tip. Employing Eq. (2.11) to compute the propagation speed gives similar values of around $0.26\,U_\infty$ for the range of Mach numbers studied, now having a positive sign, implying outboard propagation. Additionally, higher-frequency outboard-running waves, confined to the tip region, coexist with the lower-frequency shock unsteadiness highlighting distinct flow phenomena beyond buffeting onset, as outlined from the instantaneous snapshots at $M = 0.80$ and $\alpha = 3.3°$ in Fig. 4.17. Figure 6.6a shows the phase angle variation along the shock at 216 Hz for three angles of attack beyond buffeting onset at $M = 0.80$. The linear phase variation outboard of $\eta = 0.78$, having a negative slope, implies outboard-running propagations at this frequency. This corroborates the POD analysis at $\alpha = 3.3°$, whereby modes with high spatial amplitudes in the outboard region are characterised by broadband, higher-frequency behaviour, above 200 Hz, as explained in Section 4.4.1. Assessing the propagation speed of these higher-frequency and smaller-scale perturbations is more difficult, due to the broadband frequency content and intermittent dynamics. Therefore, this speed was computed between two spanwise locations for a range of frequencies related to the phenomenon. Specifically, Fig. 6.6b depicts the phase angle variation with frequency and the coherence levels of pressure signals along the shock, between $\eta = 0.87$ and 0.99, at $\alpha = 3.3°$. Relatively high coherence levels and a linear phase variation between $f = 200$ and 400 Hz ($St = 0.22$ and 0.44) imply pressure propagation, while a linear fit between these frequencies, denoted by the dashed line, gives $U_p = 0.26\,U_\infty$ from Eq. (2.12). It should be noted that this value is highly sensitive to the spanwise position of the points along

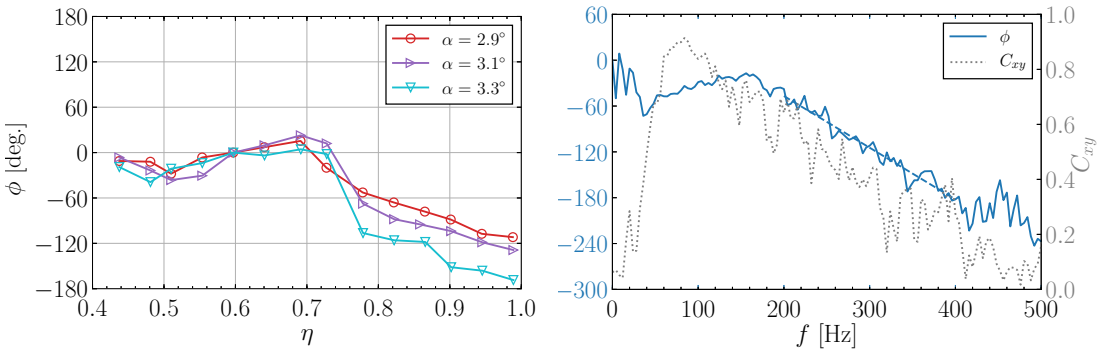

(a) Phase angle with span at 216 Hz

(b) Phase angle and coherence with frequency

Figure 6.6: Phase angle variation along shock representing higher-frequency outboard-running oscillations at $M = 0.80$; (**a**) shows the phase angle along span and (**b**) shows the phase angle (——) together with coherence levels (·····) at $\alpha = 3.3°$, computed between two points along the shock at $\eta = 0.87$ and $\eta = 0.99$, whilst (- - -) indicates a linear fit between 200 and 400 Hz.

the shock and the frequency range at which the linear fit is calculated. This results in a range of speeds between 0.21 and $0.31\,U_\infty$. Nevertheless, these propagations have a shorter wavelength, relative to the low-frequency shock unsteadiness. Taking the propagation speed as $0.26\,U_\infty$ and computing the wavelength at 200 and 400 Hz, then the wavelength decreases with frequency from $l \approx 0.3\,b \approx 1.2$ MAC to $l \approx 0.2\,b \approx 0.6$ MAC.

There is reasonable agreement when evaluating these results alongside the published shock-buffet literature. An experiment employing the AVERT half-model, based on the OAT15A aerofoil with $\Lambda_{LE} = 30°$, also reports inboard-running and outboard-running pressure propagation along the shock foot, depending on the frequency band (Dandois, 2016). To the author's knowledge, Dandois (2016) is the only experimental shock-buffet study mentioning an inboard propagation, although not studied in detail therein. Their spectral analysis at $M = 0.82$ and $\alpha = 3.5°$, which is about 0.5° above buffet onset, gives an inboard propagation at a speed of $-0.21\,U_\infty$ at $St = 0.04$. This corresponds to a wavelength of $l \approx 1.6\,b \approx 5.8$ MAC, larger than the value obtained for the RBC12 model herein and even larger than the model's semi-span. Additionally, for the same flow condition, outboard-running perturbations propagate at $0.25\,U_\infty$ at $St = 0.26$, reported to be the centre of a broadband shock-buffet bump. It is interesting to note that high coherence levels are only maintained over the whole span for the low-frequency peak. Paladini *et al.* (2018) extended this analysis to a number of different models and found a spanwise propagation speed of $0.245 \pm 0.015\,U_\infty$, across a Strouhal number range between 0.2 and 0.3. The spanwise wavelength varied between 0.55 and 1.6 MAC. Sugioka *et al.* (2018) performed a spectral analysis using unsteady PSP data on an 80%-scaled NASA Common Research Model (CRM). A propagation speed of $0.53\,U_\infty$ at $St = 0.31$ was reported at $M = 0.85$ and $\alpha = 4.68°$, which is 1.0° above buffet onset. In this case, the spanwise wavelength varies between 1.3 and 1.7 MAC. This considerable spread between different experiments highlights the difficulty to attribute

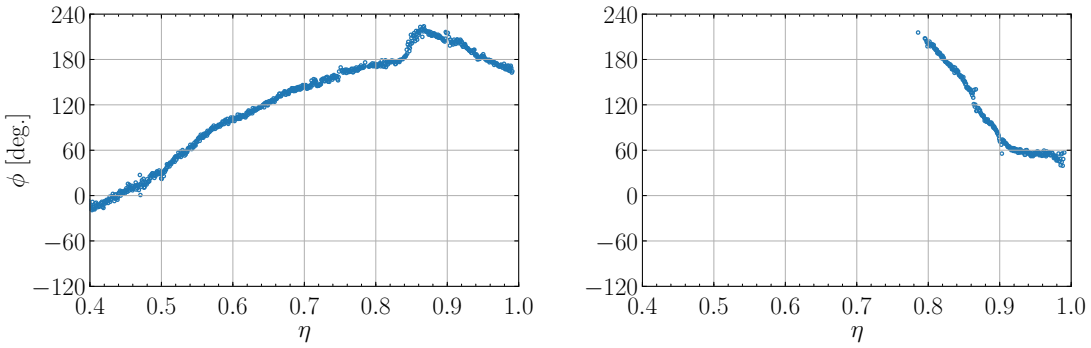

(a) DMD mode at 83 Hz

(b) DMD mode at 245 Hz

Figure 6.7: Phase angle variation along path of maximum magnitude for selected DMD modes at $M = 0.80$ and $\alpha = 3.3°$.

the spanwise propagation in swept-wing buffet to a single geometrical feature or flow parameter. Recent numerical studies have tried to link the sweep angle to the frequency and wavelength of the outboard-running cellular patterns (Crouch *et al.*, 2019; Paladini *et al.*, 2019; Plante *et al.*, 2020; He & Timme, 2020*b*).

These observations regarding the spanwise propagation of pressure along the shock are immediately apparent from the phase information encoded by the DMD modes presented in Section 4.4.2. The phase angle was computed from the real and imaginary parts of the modes at each spanwise pixel, with the chordwise pixel corresponding to the location of maximum magnitude. The phase angle variation with span for the two DMD modes depicted in Figs. 4.19 and 4.20 is shown in Fig. 6.7. In order to reduce noise and obtain insightful trends, the phase angle is only computed at locations which have at least 20% of the maximum magnitude value for the same mode. The phase angle variation of the low-frequency shock unsteadiness mode in Fig. 6.7a corresponds to an inboard-running propagation inboard of $\eta = 0.87$ and outboard-running propagation between this spanwise location and the wing tip, supporting the cross-spectral analysis presented previously in Fig. 6.2. At the higher frequency of 245 Hz, the phase angle variation in Fig. 6.7b indicates outboard-running propagation, emanating from $\eta = 0.78$ and confined to the wing tip, corroborating the spectral analysis at 216 Hz in Fig. 6.6a

The process devised in Section 6.1 employing a cross-spectrum analysis to quantify the pressure propagation along the shock was extended to the VG configurations. Figure 6.8 depicts the phase variation along the shock at $f = 80$ Hz for flow conditions corresponding to both buffet onset and 0.4° beyond onset for the three configurations. The linear phase variation indicates pressure propagation which is predominantly inboard running (positive slope) but reverses direction close to the wing tip, with the inflection point depending on configuration. It is evident that the characteristic inboard-running behaviour at frequencies corresponding to low-frequency shock unsteadiness is not being suppressed by the VGs. The change in slope downstream of the VGs, located

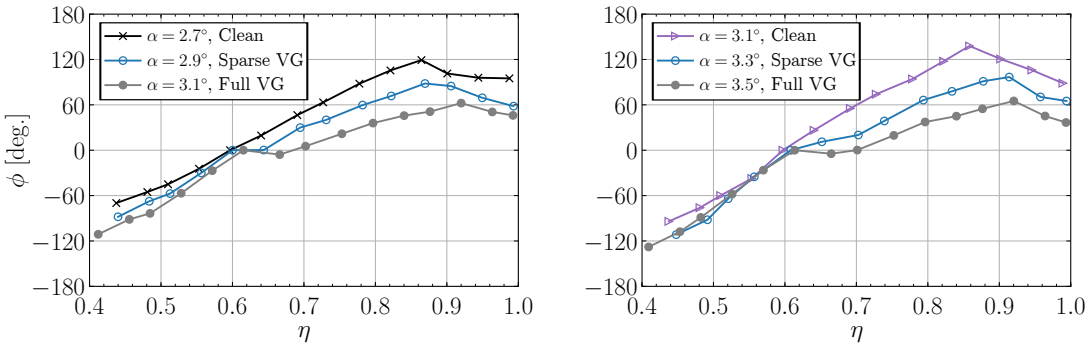

(a) Buffet onset

(b) 0.4° post onset

Figure 6.8: Phase angle variation along shock at 80 Hz for the three configurations at buffet onset and beyond onset at $M = 0.80$; clean wing (× and ▷), sparse VG (○) and full VG (●).

between 63% and 91% semi-span, implies a different propagation speed which changes with configuration. The clean wing propagation speed is 68 m/s ($0.26\,U_\infty$) which increases to 83 m/s ($0.31\,U_\infty$) for the sparse VG configurations and 117 m/s ($0.45\,U_\infty$) for the full VG configuration. In the case of the VG configurations, the propagation speed reduces to 57 m/s ($0.22\,U_\infty$) farther inboard of approximately $\eta = 0.6$, slightly lower than that on the clean wing. Moreover, the reversal in propagation direction occurs closer to the wing tip with the addition of VGs, farther outboard of the VG locations. The discontinuity in slope between $\eta = 0.60$ and 0.65 corresponds to the spanwise region whereby the shock unsweeps between the controlled and uncontrolled flow farther inboard, as highlighted by the DPSP standard deviation in Fig 4.21.

6.2 Low-Frequency Shock Unsteadiness and Shock Buffet

This synergistic study comprising a detailed analysis from experimental DPSP and numerical DDES has shown that the low-frequency shock unsteadiness behaviour is exclusive to the wind-tunnel data. Its manifestation, even in attached flow conditions at pre-onset incidences, and its possible connection to the shock-buffet instability are intriguing indeed. Since the publication by Dolling (2001), some studies discussing the fundamental flow physics of SWBLI have concentrated on the topic of unsteadiness. The exact mechanisms responsible for these large-scale, low-frequency motions remain debated, as introduced in Chapter 1. These are typically classified into two main groups—upstream disturbances within the incoming boundary layer and a downstream mechanism dominated by a large scale instability intrinsic to the separated flow (Clemens & Narayanaswamy, 2014). Complex flow phenomena characterise SWBLI across a range of flow regimes, from transonic to supersonic and even hypersonic. Owing to the lack of a reconciled viewpoint on the fundamental physics, numerous experimental and computational efforts have been focused on canonical geometries, mostly

at supersonic conditions (Gaitonde, 2015). Moreover, transonic interactions can differ in many ways, as upstream acoustic-wave propagation within the surrounding subsonic region is able to influence the interaction (Babinsky & Harvey, 2011).

A careful review of the shock-buffet literature reveals earlier evidence of low-frequency shock motion on swept-wing half models in transonic wind-tunnel environments. Riddle (1975) notes small, random shock oscillations and a low-frequency peak in the pressure spectra at zero incidence, with no corresponding structural frequencies or known wind-tunnel effects. A similar observation by Roos (1985) concerns a low-frequency meandering of the shock at cruise conditions, which being uncorrelated with root strain-gauge measurements was attributed to disturbances in the wind-tunnel flow. It should be noted that shock excursions of over 15% local chord length were reported at the cruise condition therein, whereas the low-frequency shock unsteadiness analysed herein is characterised by smaller oscillations, of about 4% local chord length at $M = 0.80$ and $\alpha = 1.6°$. This is possibly directly related to the relatively low freestream turbulence levels in the transonic wind tunnel where the RBC12 was tested, outlined in Section 4.1.1. Whilst identifying a unique source for this manifestation in the experiment is challenging, four possible causes are highlighted: (i) external forcing from an inevitable variation in freestream turbulence levels in the wind tunnel (as mentioned, too, by Roos (1985)), (ii) the model's structural dynamics considering the inherent flexibility of large aircraft wings, (iii) forcing from upstream or downstream of the shock wave resulting either from coherent structures within the upstream boundary layer or the dynamics between the shock wave and the separated region (Clemens & Narayanaswamy, 2014), and (iv) an intrinsic property of the SWBLI (Touber & Sandham, 2011). The following part of the discussion gives further evidence of these lower-frequency shock dynamics which are evidently present in wind tunnels but not thoroughly discussed in existing experimental shock-buffet studies.

The frequency spectra around buffet onset are dominated by this low-frequency shock unsteadiness owing to intense pressure fluctuations as the shock oscillates around its mean position. Slightly incrementing the angle of attack around structural buffeting onset at the design Mach number of 0.80, Figs. 4.9b and 4.10b highlight how pressure transducers downstream of the shock location measure increased fluctuations, centred at $St = 0.07$, as the shock-induced separation extends to the trailing edge. This coincides with the increased strain-gauge response as the low-frequency shock unsteadiness and the shock-induced separated region excite the structural modes of the model. The formation of this localised separated region is visualised clearly by the DPSP standard deviation in Fig. 4.7h. Furthermore, the cross-spectral analysis reveals a well-defined change regarding the pressure propagation along the shock. Whilst pre-buffet conditions are dominated by an inboard propagation at low frequencies, the formation of a localised separated region causes a reversal in propagation direction at the outboard location of the separation. This has consistently been characterised around structural

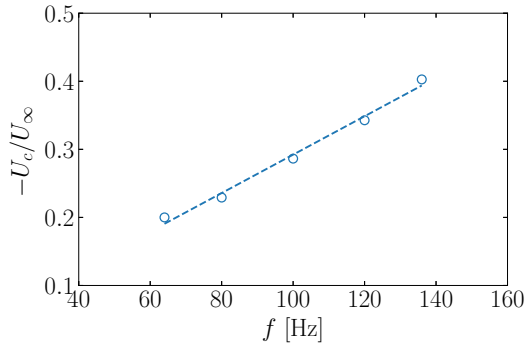

Figure 6.9: Linear variation of propagation speed with frequency at $M = 0.80$ and $\alpha = 3.3°$.

buffeting onset in the Mach number range between 0.70 and 0.84, as highlighted in Figs. 6.3 and 6.4. Although the frequencies at the centre of the spectral bump for this low-frequency unsteadiness lie within the values typically reported for aerofoil buffet (Feldhusen-Hoffmann *et al.*, 2018), different mechanisms are responsible. The frequency range is consistent for the Mach numbers assessed, with high coherence levels along the span, whereby the chordwise distance between the shock location and the trailing edge changes. For instance, the mean shock location at $\eta = 0.73$ differs by over $0.35\,c$ between $M = 0.70$ and $M = 0.84$ at the corresponding buffet onset angle of attack. This would significantly alter the two-dimensional, narrow-peak buffet frequency governed by an aeroacoustic coupling between the shock wave and the trailing edge. Furthermore, it has been shown in Table 6.1 that similar propagation speeds characterise the low-frequency shock unsteadiness at different Mach numbers.

The computation of propagation speeds at several frequencies using Eq. (2.11) and the method described in Section 6.1 yields a linear variation of propagation speed with frequency, at each Mach number, such that a single wavelength (approximately 3 MAC) characterises this unsteadiness. An example at the design Mach number is shown in Fig. 6.9. The second phenomenon, observed only beyond onset conditions, shows a broadband, higher-frequency behaviour in a Strouhal number range between 0.2 and 0.5. This unsteadiness is well defined by PSD data from unsteady transducers on the outboard wing beyond buffet onset in Fig. 4.9b. The shock motion analysis in Section 6.1 showed that this unsteadiness constitutes a range of wavelengths (approximately between 0.6 to 1.2 MAC) in contrast to the single wavelength attributed to the low-frequency shock unsteadiness. These characteristic features of the higher-frequency behaviour identified herein are similar to the medium-wavelength (around one chord on infinite span wings) band of modes linked to swept-wing shock buffet and first presented by Crouch *et al.* (2019). Figure 6.10 depicts the experimental results obtained herein alongside recent numerical studies. The studies by Crouch *et al.* (2019) and Paladini *et al.* (2019) are based on biglobal stability analyses on infinite-span geometries whilst Timme (2020) employs triglobal stability analysis on the NASA CRM, a

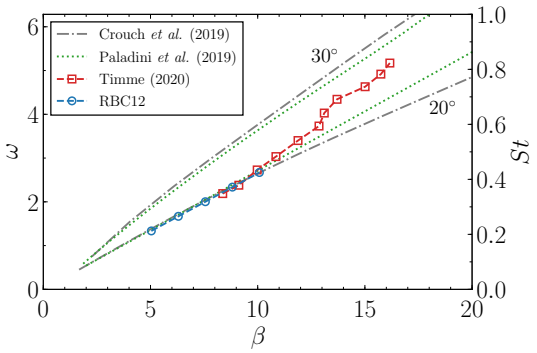

Figure 6.10: Angular frequency ω (and Strouhal number) as a function of spanwise wavenumber β for the shock-buffet mode. The data are made dimensionless using the reference freestream velocity U_∞ and the mean aerodynamic chord (which is chord length for the infinite span geometries). The annotations indicate the sweep angle whilst the data at $\Lambda = 20°$ from Paladini *et al.* (2019) is computed using the empirical relation $\omega = 0.70\tan(20°)\beta$ and rescaled by $\cos(20°)$. The study by Timme (2020) is conducted on the NASA Common Research Model.

practical non-canonical test case. The angular frequency, $\omega = 2\pi St$, and the spanwise wavenumber, $\beta = 2\pi/l$, are made dimensionless using the MAC for finite wings and the chord length for infinite wings together with the freestream velocity U_∞. Nominal data are taken from Crouch *et al.* (2019) and Timme (2020) whilst those from Paladini *et al.* (2019) have been rescaled with the reference freestream velocity U_∞ and multiplied by $\cos(\Lambda)$. It should be noted that the data from finite wings cannot be directly compared with those from infinite-span geometries due to the influence of secondary geometric features such as twist and taper, as contemplated by Plante *et al.* (2020) and Timme (2020). However, in all cases, outboard-propagating cellular patterns spanning this particular range of medium wavelengths and propagation speed occur. Another common trend is the decreasing wavelength with frequency of these cellular patterns. Furthermore, the specific comparison of the two practical geometries, namely, the data herein from an older-generation wing with lower sweep angle ($\Lambda_{c/4} = 25°$) compared to the CRM studied in Timme (2020) ($\Lambda_{c/4} = 35°$) follows the general observation of increased propagation speed ($U_p = \omega/\beta$) with sweep angle.

This discussion of the experimental analysis makes it evident that the interpretation of the flow physics governing buffet onset on swept wings is quite ambiguous, with co-existing phenomena and several possible drivers thereof. Although the numerical study was planned from the outset of this investigation, the experimental findings provided further motivation to perform the numerical simulations in order to concentrate on the fluid-only instability and narrow down the sources of the flow unsteadiness. This approach together with direct comparisons using modal analyses of vast volumes of data have elucidated how the manifestation of the low-frequency shock unsteadiness is exclusive to the experimental data, possibly induced by one or more of multiple sources, whilst the higher-frequency outboard running phenomenon is purely aerody-

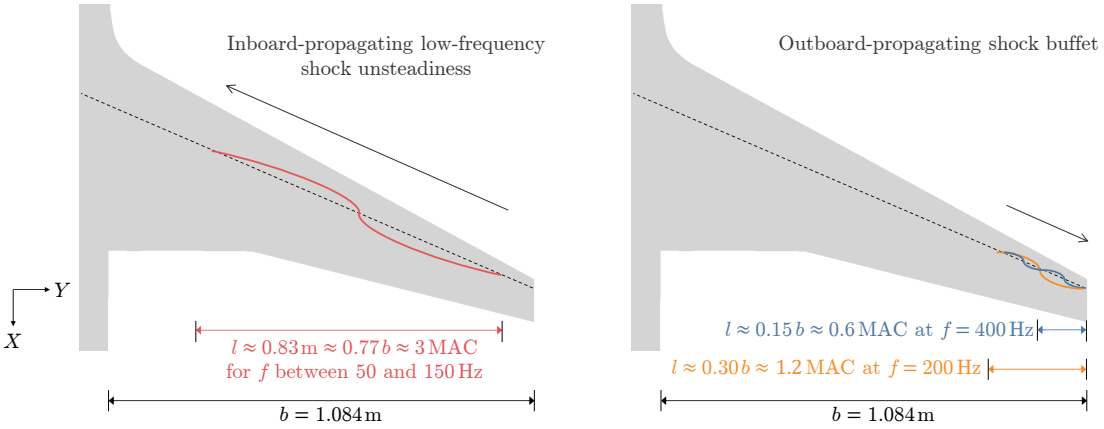

(a) Low-frequency shock unsteadiness **(b)** Swept-wing shock buffet

Figure 6.11: Schematic of the two coexisting phenomena identified herein.

namic and renders swept-wing shock buffet self-sustaining. The schematic presented in Fig. 6.11 aids the visualisation of the two phenomena that have been discussed herein. The DPSP snapshots beyond structural buffeting onset have revealed longer-wavelength (approximately 3 MAC) perturbations running predominantly inboard at low-frequency, in addition to higher-frequency, shorter-wavelength (approximately between 0.6 to 1.2 MAC) propagations moving outboard, confined to the tip region. It is emphasised that the first phenomenon referred to as low-frequency shock unsteadiness is characterised by a single wavelength whereas the second phenomenon constitutes cellular patterns over a range of wavelengths related to swept-wing shock buffet.

Passive flow control by means of vane vortex generators is effective in delaying the buffet-onset incidence based on the strain-gauge response by up to 0.4°, depending on the density of the VG array. The frequency spectra along the shock, which for the controlled cases is positioned farther downstream relative to the clean wing, show a similar behaviour to the uncontrolled case being dominated by the low-frequency shock unsteadiness. However, it is important to note that even at 0.6° post onset, the higher-frequency cellular pattern on the wing tip is not observed and seems to be suppressed by the full VG array. With regards to the flow topology around buffet onset, this is similar between the clean wing and the sparse VG array, whereby the onset of the structural response coincides with the formation of a shock-induced separated region on the outboard wing between $\eta = 0.65$ and 0.90. In contrast, the full VG array shows a different pattern whereby an intense flow separation occurs downstream of the most inboard VG, between the controlled and uncontrolled flows. Furthermore, the cross-spectral analysis along the shock for the VG cases in Fig. 6.8 reveals additional insight on the low-frequency shock unsteadiness. First, it supports the observation that pressure propagation at low frequency is predominantly inboard running, only reversing

spanwise direction outboard of the localised separation region, and in the case of the controlled cases, this coincides with the outermost VG. Second, the increased number of vortex generators, and hence greater addition of induced streamwise vorticity in the near-wall region, corresponds to faster propagation of pressure along the shock. This is an interesting observation which requires further work in order to understand the effect of the upstream boundary layer on the SWBLI.

Chapter 7

Conclusions and Outlook

A study based on complementing high-quality experimental and numerical data has been presented with the primary aim of describing the flow physics governing shock-buffet onset on swept wings. Swept-wing shock buffet is normally characterised by unsteady shock dynamics with a broadband frequency signature mutually interacting with an intermittently separated boundary layer which results in the formation of three-dimensional cellular patterns and spanwise propagation of disturbances. However, literature on swept-wing shock buffet is quite limited, especially when it comes to practical finite-wing geometries, in contrast to the widely studied shock buffet on aerofoils. In addition, the literature tends to focus on flow conditions well beyond onset. Whilst recent numerical studies have been directed towards the onset of the instability, these mostly employ infinite-wing canonical geometries. This thesis has aimed to fill this gap in the literature by exploring a half wing-body configuration representing a civil aircraft using an extensive experimental dataset from an industrial transonic wind tunnel together with scale-resolving numerical simulations. One of the main objectives was to employ suitable data processing techniques to analyse the vast volumes of data. The use of data-based modal identification techniques, namely proper orthogonal decomposition and dynamic mode decomposition, was motivated by the spatial and temporal resolution of the datasets together with the advantage of enabling direct quantitative comparison based on the pertinent flow features. Both the experimental and numerical contributions to this study have been crucial in identifying two distinct phenomena dominating the flow physics around the onset of the shock-buffet instability.

The experimental study provides a richer analysis of the experiment first presented by Lawson *et al.* (2016). Numerous wind-tunnel corrections need to be understood, together with an unambiguous definition of onset indicators, to explain the experimental observations clearly. Herein, the so-called structural buffeting (the wing vibration response) measured by the strain gauge is chosen. The application of modal analysis techniques to dynamic pressure-sensitive paint data in addition to conventional methods enables deeper analysis. The key insight is the identification of two distinct phenomena

at shock-buffet onset conditions after analysing data at seven Mach numbers between 0.70 and 0.84 mostly around the onset of structural buffeting. The first phenomenon, herein referred to as low-frequency shock unsteadiness, is characterised by shock motion for Strouhal numbers between 0.05 and 0.15 (where Strouhal number is based on mean aerodynamic chord and reference freestream velocity) and predominantly propagates pressure disturbances inboard. Details on this low-frequency shock unsteadiness have not been analysed thoroughly in the literature previously. The second phenomenon is more broadband and spans higher frequencies, specifically, Strouhal numbers between 0.2 and 0.5. It is characterised by three-dimensional cellular patterns that propagate pressure outboard and agrees with the widely accepted definition of swept-wing shock buffet. An important finding is that the first phenomenon, in contrast to the second phenomenon, is pertinent at all flow conditions, even before the onset of structural buffeting. The spatial coverage of the dynamic pressure-sensitive paint data is instrumental for detailed shock-motion analysis considering the significant chordwise shock displacement through the Mach number range where discrete transducers would fail. In the case of passive flow control with vane vortex generators, the increase of structural buffeting with angle of attack is more gradual, when compared to the clean wing. Buffet onset is delayed by up to 0.4° whilst the higher-frequency content near the wing tip is suppressed by the full array. The flow topology beyond shock-buffet onset in the case of the full vortex-generator array is different with a distinct flow separation occurring between the controlled and uncontrolled region of the flow, just downstream of the most inboard vortex generator.

This unique experimental dataset is contrasted with scale-resolving detached-eddy simulations, attaining the objective of numerical simulation in the vicinity of buffet onset. The simulations have shown that, at critical conditions, trailing-edge and shock-induced separations merge and cells of localised separated flow repeatedly perturb the shock wave, and vice versa, via a self-sustaining mechanism. Whilst standard delayed detached-eddy simulation improves upon unsteady Reynolds-averaged Navier–Stokes simulations well beyond shock buffet onset conditions, as previously demonstrated, a more recent vorticity-sensitive variant better matches the experimental data and is more suited for problems involving separating and reattaching shallow shear layers. Although such simulation of a practical geometry remains challenging, the latter unlocks, through its formulation, turbulent content earlier and better resolves the unsteadiness constituting shock buffet at onset conditions. The classical subgrid length scale based on maximum-edge length predicts nearly periodic oscillations at a Strouhal number of approximately 0.22, whereas the incorporation of the solution-dependent vorticity vector gives a more irregular signal with broadband content centred at a Strouhal number of approximately 0.27. Modal analysis reveals striking similarity between equivalent modes from the experimental and numerical datasets dominated by outboard pressure propagation along and downstream of the shock confined to the wing tip region, in

the typical swept-wing shock-buffet frequency range. A shear-layer mode in the wake resembling a Kelvin–Helmholtz-type instability is also identified from the simulations. Standard delayed detached-eddy simulation studying the influence of flight Reynolds number shows that buffet onset is only slightly delayed and has similar inherent dynamics. The outboard-running propagations emanate from farther outboard, compared to the equivalent model-scale simulation at the same angle of attack, and have a more irregular time history with peaks at Strouhal numbers of 0.23 and 0.29.

The two key flow phenomena identified herein have been compared by a detailed shock motion analysis from the dynamic pressure-sensitive paint data, with distinct characteristics as the angle of attack is incremented. At pre-onset conditions, whereby the flow remains attached downstream of the shock, pressure propagates in the inboard direction as a result of the low-frequency shock unsteadiness. Increasing the angle of attack to and beyond structural buffeting onset, the stronger shock causes a shock-induced separation bubble to merge with trailing-edge separation. Whilst disturbances continue to propagate inboard, a reversal in propagation direction is observed such that pressure now propagates towards the wing tip from the outermost location of the localised flow separation. This is observed consistently at all assessed Mach numbers. Reaching structural buffeting onset, the formation of a localised separation in the outer wing region leads to the second higher-frequency phenomenon, exclusive to post-onset conditions and simultaneously observed with the low-frequency shock unsteadiness. The inboard propagation of the latter takes place at a speed of approximately 0.26 (made dimensionless by the reference freestream velocity) for a Strouhal number of approximately 0.09, irrespective of Mach number and hence the buffet-onset angle of attack. A characteristic wavelength of approximately 0.8 semi-span lengths (equivalent to approximately three mean aerodynamic chords) is found from a linear variation of propagation speed with frequency. In the case of the second phenomenon, this constitutes a range of wavelengths of 0.2 to 0.3 semi-span lengths (approximately between 0.6 to 1.2 mean aerodynamic chords), computed for Strouhal numbers between 0.22 and 0.44. The propagation speed is found to have a range between 0.21 and 0.31 of reference freestream velocity. It can be concluded that these characteristic features of the higher-frequency behaviour identified herein are similar to the medium-wavelength (around one chord on infinite span wings) band of modes identified in recent numerical studies and linked to swept-wing shock buffet. With the addition of vortex generators, the inboard propagation speed of the low-frequency shock unsteadiness was found to increase, reaching approximately 0.31 for the sparse configuration with 8 vortex generators and approximately 0.45 reference freestream velocity for the full array with 30 vortex generators, at the characteristic Strouhal number of 0.09. Moreover, the reversal in propagation direction occurs closer to the wing tip.

It has been stressed that even though a remarkable agreement between the simulations and the experiment was achieved overall, the lower-frequency shock unsteadiness

behaviour is unique to the wind-tunnel test and does not feature in the fully developed buffet phase of the fluid-only numerical analyses. Possible sources for this discrepancy have been contemplated as identifying a unique source is challenging. This motivates several research avenues that can be pursued, categorised into two main groups; (i) understanding the source of the lower-frequency shock unsteadiness and (ii) more advanced data analysis using emerging methods.

Considering the first group which aims to understand the physics comprehensively, a possible driver of the lower-frequency shock unsteadiness is an external forcing from an inevitable variation in freestream turbulence levels and possibly additional disturbances in the wind-tunnel environment. Several sensors were available in the wind-tunnel test to identify the flow unsteadiness, including a hot wire anenometer, a microphone and a wall-mounted unsteady pressure transducer. These are useful in computing the buffeting levels of the model due to background unsteadiness whilst exploring possible correlation between the freestream turbulence levels and the shock unsteadiness.

Second, large aircraft wind-tunnel models are inherently flexible. In the numerical study herein, the geometry is considered rigid excluding any static or dynamic deformation in order to focus exclusively on the inherent fluid dynamics. Although the static deformation is believed to have negligible influence, this assertion requires further scrutiny. In addition, low-frequency peaks at 10 and 20 Hz identified from dominant modes in the experimental data are not completely understood and might be linked to the wind-tunnel dynamics. To this end, a finite-element study of the model mounted to the wind tunnel test section would help clarify these observations. A fully-coupled aeroelastic simulation is suggested to study both the static deformation and the dynamic fluid-structure interaction.

The third possible source of the lower-frequency shock unsteadiness emanates from other physical mechanisms which are typically grouped in two (Clemens & Narayanaswamy, 2014). The first are specific events or coherent structures in the upstream boundary layer whilst the second relate to causal mechanisms downstream of the shock. Lastly, Touber & Sandham (2011) discuss a fourth source and explain their low-frequency shock motions as a forced dynamical system which is intrinsic to the shock-wave/boundary-layer interaction and not necessarily a property of a forcing coming from downstream or upstream. In the specific case of transonic shock buffet on swept wings, whilst an absolute instability has been recently linked to its onset (Timme, 2020), the role of convective mechanisms and any connection with the observed low-frequency shock unsteadiness remain to be scrutinised. These potential sources would benefit from the highest-fidelity of simulations, specifically direct numerical simulation, in order to study the intricate boundary layer flow physics and possible correlation with the shock unsteadiness. However, such simulation is currently limited to canonical geometries at medium Reynolds number and will probably remain unrealistic for a practical wing at high Reynolds number in the foreseeable future (Zauner *et al.*, 2019).

Whilst this thesis has focused primarily on the clean wing configuration in the vicinity of buffet onset, the wind-tunnel testing was extensive and comprises other data points at higher angle of attack and also other configurations, specifically those with passive flow control and the alternative transition location. A study on how vane vortex generators and a longer laminar region impact the flow physics governing buffet onset would be beneficial to inform buffet control strategies and future wing design.

To help understand the contribution of those four possible sources for the lower-frequency shock unsteadiness whilst providing validation data for numerical simulation, a new wind-tunnel test is suggested. A fully equipped test campaign could make use of dynamic model deformation measurement using stereo particle tracking, dynamic pressure-sensitive paint and temperature-sensitive paints, providing a time-synchronised database of distributed aerodynamic load and deformation measurements at high spatial and temporal resolution. Additionally, time-resolved tomographic particle image velocimetry is recommended for off-body flow field data for wake measurement and the validation of numerical data. A sting-mounted model would permit accurate measurement of the flow angle correction, aiding the direct comparison of the experimental data with numerical simulation.

Such an experiment equipped with what is possible in conjunction with scale-resolving simulation would inevitably yield massive volumes of data for which the second group of research avenues emerging from this study is required. Considering the success of data-based modal identification techniques herein, this analysis framework can be further developed to incorporate faster algorithms, in turn enabling real-time analysis and fusion with simulation to inform the efficient acquisition of data points in the experiment. The ever increasing volumes of data from the symbiotic relation between experiment and numerical simulation are driving the rapid development and application of machine learning within the research community for the analysis of fluid flows. The advent of data fusion and assimilation techniques can provide an aerodynamic dataset with invaluable insight for high-value product design that is independent of the origin of the data. Such advanced methods and the potential to uncover previously unattainable information from state-of-the-art datasets are intriguing indeed.

References

AGARD 1975 The effects of buffeting and other transonic phenomena of maneuvering combat aicraft. *Tech. Rep.* AGARD-AR-82. North Atlantic Treaty Organisation.

Allmaras, S. R., Johnson, F. T. & Spalart, P. R. 2012 Modifications and clarifications of the Spalart–Allmaras turbulence model. In *7th International Conference on Computational Fluid Mechanics*. ICCFD7-1902.

Babinsky, H. & Harvey, J. K. 2011 *Shock wave-boundary-layer interactions*. Cambridge University Press.

Balakrishna, S. & Acheson, M. 2011 Analysis of NASA common research model dynamic data. AIAA 2011-1127.

Bartlett, M. S. 1948 Smoothing periodograms from time-series with continuous spectra. *Nature* **161** (4096), 686–687.

Bekemeyer, P. & Timme, S. 2019 Flexible aircraft gust encounter simulation using subspace projection model reduction. *Aerospace Science and Technology* **86**, 805 – 817.

Belesiotis-Kataras, P. & Timme, S. 2018 Numerical study of incipient transonic shock buffet on large civil aircraft wings. In *Royal Aeronautical Society 2018 Applied Aerodynamics Conference*.

Belson, B. A., Tu, J. H. & Rowley, C. W. 2014 Algorithm 945: Modred—a Parallelized Model Reduction Library. *ACM Transactions on Mathematical Software* **40** (4), 1–23.

Benoit, B. & Legrain, I. 1987 Buffeting prediction for transport aircraft applications based on unsteady pressure measurements. AIAA 1987-2356.

Berkooz, G., Holmes, P. & Lumley, J. L. 1993 The proper orthogonal decomposition in the analysis of turbulent flows. *Annual Review of Fluid Mechanics* **25** (1), 539–575.

Blazek, J. 2015 *Computational fluid dynamics: Principles and applications*. Butterworth-Heinemann.

Boussinesq, J. 1877 Essai sur la théorie des eaux courantes. *Mémoires présentés par divers savants à l'Académie des Sciences de l'Institut National de France* **23**.

Breuer, M. 1998 Large eddy simulation of the subcritical flow past a circular cylinder: Numerical and modeling aspects. *International Journal for Numerical Methods in Fluids* **28** (9), 1281–1302.

Brion, V., Dandois, J., Abart, J.-C. & Paillart, P. 2017 Experimental analysis of the shock dynamics on a transonic laminar airfoil. *Progress in Flight Physics* **9**, 365–386.

Brunet, V. 2003 Computational study of buffet phenomenon with unsteady RANS equations. AIAA 2003-2679.

Brunet, V. & Deck, S. 2008 Zonal-detached eddy simulation of transonic buffet on a civil aircraft type configuration. AIAA 2008-4152.

Burg, J. P. 1967 Maximum entropy spectral analysis. In *37th Annual International Meeting of the Society of Exploration Geophysicists*.

Chauvet, N., Deck, S. & Jacquin, L. 2007 Zonal detached eddy simulation of a controlled propulsive jet. *AIAA Journal* **45** (10), 2458–2473.

Chen, K. K., Tu, J. H. & Rowley, C. W. 2012 Variants of Dynamic Mode Decomposition: Boundary Condition, Koopman, and Fourier Analyses. *Journal of Nonlinear Science* **22** (6), 887–915.

Clemens, N. T & Narayanaswamy, V. 2014 Low-frequency unsteadiness of shock wave/turbulent boundary layer interactions. *Annual Review of Fluid Mechanics* **46**, 469–492.

Crafton, J., Forlines, A., Palluconi, S., Hsu, K.-Y., Carter, C. & Gruber, M. 2015 Investigation of transverse jet injections in a supersonic crossflow using fast-responding pressure-sensitive paint. *Experiments in Fluids* **56** (27), 1–15.

Crafton, J., Gregory, J., Sellers, M. & Ruyten, W. 2017 Data processing tools for dynamic pressure-sensitive paint. AIAA 2017-0701.

Crouch, J. D., Garbaruk, A. & Magidov, D. 2007 Predicting the onset of flow unsteadiness based on global instability. *Journal of Computational Physics* **224** (2), 924–940.

Crouch, J. D., Garbaruk, A., Magidov, D. & Travin, A. 2009 Origin of transonic buffet on aerofoils. *Journal of Fluid Mechanics* **628**, 357–369.

Crouch, J. D., Garbaruk, A. & Strelets, M. 2019 Global instability in the onset of transonic-wing buffet. *Journal of Fluid Mechanics* **881**, 3–22.

Dandois, J. 2016 Experimental study of transonic buffet phenomenon on a 3D swept wing. *Physics of Fluids* **28** (016101), 1–17.

Dandois, J., Mary, I. & Brion, V. 2018 Large-eddy simulation of laminar transonic buffet. *Journal of Fluid Mechanics* **850**, 156–178.

Deck, S. 2005 Numerical simulation of transonic buffet over a supercritical airfoil. *AIAA Journal* **43** (7), 1556–1566.

Deck, S. 2012 Recent improvements in the zonal detached eddy simulation ZDES formulation. *Theoretical and Computational Fluid Dynamics* **26**, 523–550.

Dolling, D. S. 2001 Fifty years of shock-wave/boundary-layer interaction research: What next? *AIAA Journal* **39** (8), 1517–1531.

ESDU 1987 An introduction to aircraft buffet and buffeting. ESDU 87012. Engineering Sciences Data Unit.

ESDU 1995 Vortex generators for control of shock-induced separation. ESDU 93024-93026. Engineering Sciences Data Unit.

Favre, A. 1965*a* Equations des gaz turbulents compressibles, part 1: Formes générales. *Journal de mécanique* **8**, 361–390.

Favre, A. 1965*b* Equations des gaz turbulents compressibles, part 2: Méthode des vitesses moyennes; méthode des vitesses moyennes pondérées par la masse volumique. *Journal de mécanique* **8**, 391–421.

Feldhusen-Hoffmann, A., Statnikov, V., Klaas, M. & Schröder, W. 2018 Investigation of shock–acoustic-wave interaction in transonic flow. *Experiments in Fluids* **59** (15), 1–13.

Fukushima, Y. & Kawai, S. 2017 Wall-modeled Large-Eddy Simulation of transonic buffet over a supercritical airfoil at high Reynolds number. AIAA 2017-0495.

Gaitonde, D. V. 2015 Progress in shock wave/boundary layer interactions. *Progress in Aerospace Sciences* **72**, 80–99.

Garner, H. C., Rogers, E. W., Acum, W. E. A. & C., Maskell E. 1966 Subsonic wind tunnel wall corrections. *Tech. Rep.* AGARDograph 109. North Atlantic Treaty Organisation.

Garnier, E. & Deck, S. 2010 Large-Eddy Simulation of transonic buffet over a supercritical airfoil. In *Turbulence and Interactions: Proceedings the TI 2009 Conference* (ed. M. Deville, T.-H. Lê & P. Sagaut), pp. 135–141. Berlin, Heidelberg: Springer Berlin Heidelberg.

Giannelis, N., Vio, G. & Levinski, O. 2017 A review of recent developments in the understanding of transonic shock buffet. *Progress in Aerospace Sciences* **92**, 39–84.

Green, J. E., McHugh, C. A., Baxendale, A. J. & Stanniland, D. R. 1992 The use of a deep honeycomb to achieve high flow quality in the ARA 9' x 8' Transonic Wind Tunnel. In *18th Congress of the International Council of the Aeronautical Sciences*. ICAS-92-3.5.3.

Gregory, J. W., Sakaue, H., Liu, T. & Sullivan, J. P. 2014 Fast pressure-sensitive paint for flow and acoustic diagnostics. *Annual Review of Fluid Mechanics* **46** (1), 303–330.

Grossi, F., Braza, M. & Hoarau, Y. 2014 Prediction of transonic buffet by delayed detached-eddy simulation. *AIAA Journal* **52** (10), 2300–2312.

Hartmann, A., Feldhusen, A. & Schröder, W. 2013*a* On the interaction of shock waves and sound waves in transonic buffet flow. *Physics of Fluids* **25** (026101), 1–17.

Hartmann, A., Klaas, M. & Schröder, W. 2012 Time-resolved stereo PIV measurements of shock–boundary layer interaction on a supercritical airfoil. *Experiments in Fluids* **52** (3), 591–604.

Hartmann, A., Klaas, M. & Schröder, W. 2013*b* Coupled Airfoil Heave/Pitch Oscillations at Buffet Flow. *AIAA Journal* **51** (7), 1542–1552.

Haxter, S., Brouwer, J., Sesterhenn, J. & Spehr, C. 2017 Obtaining phase velocity of turbulent boundary layer pressure fluctuations at high subsonic Mach number from wind tunnel data affected by strong background noise. *Journal of Sound and Vibration* **402**, 85–103.

He, W. & Timme, S. 2020*a* Resolvent analysis of shock buffet on infinite wings. AIAA 2020–2727.

He, W. & Timme, S. 2020*b* Triglobal shock buffet instability study on infinite wings. AIAA 2020–1986.

Hilton, W. F. & Fowler, R. G. 1947 Photographs of shock wave movement. *Tech. Rep.* ARC R&M-2692. Aeronautical Research Council.

Holmes, P., Lumley, J. L., Berkooz, G. & Rowley, C. W. 2012 *Turbulence, Coherent Structures, Dynamical Systems and Symmetry*, 2nd edn. Cambridge University Press.

Hwang, C. & Pi, W. S. 1975 Northrop F-5 A aircraft transonic buffet pressure data acquisition and response analysis. *Journal of Aircraft* **12** (9), 714–720.

Illi, S., Fingskes, C., Lutz, T. & Krämer, E. 2013 Transonic tail buffet simulations for the common research model. AIAA 2013-2510.

Iovnovich, M. & Raveh, D. E. 2012 Reynolds-Averaged Navier-Stokes study of the shock-buffet instability mechanism. *AIAA Journal* **50** (4), 880–890.

Iovnovich, M. & Raveh, D. E. 2015 Numerical study of shock buffet on three-dimensional wings. *AIAA Journal* **53** (2), 449–463.

Ishida, T., Hashimoto, A., Ohmichi, Y., Aoyama, T. & Takekawa, K. 2017 Transonic buffet simulation over NASA-CRM by Unsteady-FaSTAR code. AIAA 2017-0494.

Jacquin, L., Molton, P., Deck, S., Maury, B. & Soulevant, D. 2009 Experimental study of shock oscillation over a transonic supercritical profile. *AIAA Journal* **47** (9), 1985–1994.

Jameson, A. 1991 Time dependent calculations using multigrid, with applications to unsteady flows past airfoils and wings. AIAA 1991–1596.

Jones, J. G. 1971 A survey of the dynamic analysis of buffeting and related phenomena. *Tech. Rep.* RAE 72197. Royal Aeronautical Establishment.

Koike, S., Nakakita, K., Nakajima, T., Koga, S., Sato, M., Kanda, H., Murayama, M., Ito, Y. & Yamamoto, K. 2015 Experimental investigation of vortex generator effect on two- and three-dimensional NASA common research models. AIAA 2015-1237.

Koike, S., Ueno, M., Nakakita, K. & Hashimoto, A. 2016 Unsteady pressure measurement of transonic buffet on NASA common research model. AIAA 2016-4044.

Kok, J.C. 2009 A high-order low-dispersion symmetry-preserving finite-volume method for compressible flow on curvilinear grids. *Journal of Computational Physics* **228** (18), 6811–6832.

Kravchenko, A.G. & Moin, P. 1997 On the effect of numerical errors in large eddy simulations of turbulent flows. *Journal of Computational Physics* **131** (2), 310–322.

Lawson, S. 2015 Buffet control of transonic wings in the ARA Transonic Wind Tunnel. *Tech. Rep.* ARA CR RBC01202. Aircraft Research Association Limited.

Lawson, S. & Greenwell, D. 2015 Buffet control of transonic wings final report. *Tech. Rep.* ARA CR RBC01203. Aircraft Research Association Limited.

Lawson, S., Greenwell, D. & Quinn, M. K. 2016 Characterisation of buffet on a civil aircraft wing. AIAA 2016-1309.

Lee, B. H. K. 1990 Oscillatory shock motion caused by transonic shock boundary-layer interaction. *AIAA Journal* **28** (5), 942–944.

Lee, B. H. K. 2001 Self-sustained shock oscillations on airfoils at transonic speeds. *Progress in Aerospace Sciences* **37** (2), 147–196.

Löwe, J., Probst, A., Knopp, T. & Kessler, R. 2016 Low-dissipation low-dispersion second-order scheme for unstructured finite volume flow solvers. *AIAA Journal* **54** (10), 2961–2971.

Lumley, J. L. 1967 The structure of inhomogeneous turbulent flows. In *Atmospheric Turbulence and Radio Wave Propagation* (ed. A. M. Yaglom & V. I. Tatarsky). Publishing House Nauka, Moscow, USSR.

Mabey, D. G. 1971 An hypothesis for the prediction of flight penetration of wing buffeting from dynamic tests on wind tunnel models. *Tech. Rep.* ARC CP 1151. Aeronautical Research Council.

Mabey, D. G. 1981 Oscillatory flows from shock induced separations on biconvex aerofoils of varying thickness in ventilated wind tunnels. In *AGARD-CP-296*.

Mabey, D. G., Welsh, B. L. & Cripps, B. E. 1981 Periodic flows on a rigid 14% thick biconvex wing at transonic speeds. *Tech. Rep.* RAE-TR-81059. Royal Aeronautical Establishment.

Masini, L., Timme, S. & Peace, A. J. 2020 Analysis of a civil aircraft wing transonic shock buffet experiment. *Journal of Fluid Mechanics* **884** (A1), 1–42.

McDevitt, J. B. & Okuno, A. F. 1985 Static and dynamic pressure measurements on a NACA 0012 airfoil in the Ames high Reynolds number facility. *Tech. Rep.* NASA TP 2485. National Aeronautics and Space Administration.

Menter, F. R. & Kuntz, M. 2004 Adaptation of eddy-viscosity turbulence models to unsteady separated flow behind vehicles. In *The Aerodynamics of Heavy Vehicles: Trucks, Buses, and Trains* (ed. R. McCallen, F. Browand & J. Ross), pp. 339–352. Springer Berlin Heidelberg.

Merienne, M.-C., Le Sant, Y., Lebrun, F., Deleglise, B. & Sonnet, D. 2013 Transonic buffeting investigation using unsteady pressure-sensitive paint in a large wind tunnel. AIAA 2013-1136.

Mockett, C., Fuchs, M., Garbaruk, A., Shur, M., Spalart, P., Strelets, M., Thiele, F. & Travin, A. 2015 Two non-zonal approaches to accelerate RANS to LES transition of free shear layers in DES. In *Progress in Hybrid RANS-LES Modelling* (ed. S. Girimaji, W. Haase, S.-H. Peng & D. Schwamborn), , vol. 130, pp. 187–201. Springer International Publishing.

Moin, P. 2002 Advances in large eddy simulation methodology for complex flows. *International Journal of Heat and Fluid Flow* **23** (5), 710–720.

NASA 1976 U.S. Standard Atmosphere, 1976. *Tech. Rep.* NASA-TM-X-74335. National Aeronautics and Space Administration.

Ohmichi, Y., Ishida, T. & Hashimoto, A. 2018 Modal decomposition analysis of three-dimensional transonic buffet phenomenon on a swept wing. *AIAA Journal* **56** (10), 3938–3950.

Paladini, E., Beneddine, S., Dandois, J., Sipp, D. & Robinet, J.-C. 2019 Transonic buffet instability: From two-dimensional airfoils to three-dimensional swept wings. *Physical Review Fluids* **4** (10), 103906.

Paladini, E., Dandois, J., Sipp, D. & Robinet, J.-C. 2018 Analysis and comparison of transonic buffet phenomenon over several three-dimensional wings. *AIAA Journal* **57** (1), 379–396.

Pearcey, H. H. 1955 Some effects of shock-induced separation of turbulent boundary layers in transonic flow past aerofoils. *Tech. Rep.* ARC R&M-3108. Aeronautical Research Council.

Pearcey, H. H. 1961 Introduction to shock-induced separation and its prevention by design and boundary layer control. In *Boundary Layer and Flow Control* (ed. G. V. Lachmann), pp. 1166–1344. Pergamon.

Pearcey, H. H. & Holder, D. W. 1962 Simple methods for the prediction of wing buffeting resulting from bubble type separation. *Tech. Rep.* NPL AERO-REP-1024. National Physics Laboratory.

Pearcey, H. H., Osborne, J. & B., Haines A. 1968 The interaction between local effects at the shock and rear separation—a source of significant scale effects in wind-tunnel tests on aerofoils and wings. In *AGARD Conference Proceedings No. 35*.

Plante, F., Dandois, J., Beneddine, S., Sipp, D. & Laurendeau, E. 2019 Numerical simulations and global stability analyses of transonic buffet and subsonic stall. In *54th 3AF International Conference on Applied Aerodynamics*. FP63-AERO2019-plante.

Plante, F., Dandois, J. & Laurendeau, É. 2019 Simulation of transonic buffet using a time-spectral method. *AIAA Journal* **57** (3), 1275–1287.

Plante, F., Dandois, J. & Laurendeau, É. 2020 Similarities between cellular patterns occurring in transonic buffet and subsonic stall. *AIAA Journal* **58** (1), 71–84.

Priebe, S., Tu, J. H., Rowley, C. W. & Martín, M. P. 2016 Low-frequency dynamics in a shock-induced separated flow. *Journal of Fluid Mechanics* **807**, 441–477.

Probst, A., Löwe, J., Reuss, S., Knopp, T. & Kessler, R. 2016 Scale-resolving simulations with a low-dissipation low-dispersion second-order scheme for unstructured flow solvers. *AIAA Journal* **54** (10), 2972–2987.

Probst, A. & Reuss, S. 2015 Scale-resolving simulations of wall-bounded flows with an unstructured compressible flow solver. In *Progress in Hybrid RANS-LES modelling*, *Notes on Numerical Fluid Mechanics and Multidisciplinary Design*, vol. 130, pp. 481–491. Springer.

Reynolds, O. 1895 On the dynamical theory of incompressible viscous fluids and the determination of the criterion. *Philosophical Transactions of the Royal Society of London* **186**.

Riddle, D. 1975 Wind-tunnel investigation of surface-pressure fluctuations associated with aircraft buffet. AIAA 1975-0067.

Rodríguez, D. & Theofilis, V. 2011 On the birth of stall cells on airfoils. *Theoretical and Computational Fluid Dynamics* **25** (1-4), 105–117.

Roos, F. 1985 The buffeting pressure field of a high-aspect-ratio swept wing. AIAA 1985-1609.

Rudnik, R., Melber-Wilkending, S. & Risley-Settle, P. 2018 Tau-solar contributions to the 3rd high lift prediction workshop. AIAA 2018-1035.

Sartor, F., Mettot, C., Bur, R. & Sipp, D. 2015 Unsteadiness in transonic shock-wave/boundary-layer interactions: Experimental investigation and global stability analysis. *Journal of Fluid Mechanics* **781**, 550–577.

Sartor, F., Mettot, C. & Sipp, D. 2014 Stability, receptivity, and sensitivity analyses of buffeting transonic flow over a profile. *AIAA Journal* **53** (7), 1980–1993.

Sartor, F. & Timme, S. 2015 Reynolds-Averaged Navier-Stokes simulations of shock buffet on half wing-body configuration. AIAA 2015-1939.

Sartor, F. & Timme, S. 2016 Mach number effects on buffeting flow on a half wing-body configuration. *International Journal of Heat and Fluid Flow* **26** (7), 2066–2080.

Sartor, F. & Timme, S. 2017 Delayed detached–eddy simulation of shock buffet on half wing–body configuration. *AIAA Journal* **55** (4), 1230–1240.

Schmid, P. J. 2010 Dynamic mode decomposition of numerical and experimental data. *Journal of Fluid Mechanics* **656**, 5–28.

Schwamborn, D., Gerhold, T. & Hannemann, V. 1999 On the validation of the DLR-TAU code. In *New Results in Numerical and Experimental Fluid Mechanics II* (ed. W. Nitsche, H.-J. Heinemann & R. Hilbig), *Notes on Numerical Fluid Mechanics*, vol. 72, pp. 426–433. Vieweg Teubner Verlag.

Schwamborn, D., Gerhold, T. & Heinrich, R. 2006 The DLR TAU-code: Recent applications in research and industry. In *ECCOMAS CFD 2006: Proceedings of the European Conference on Computational Fluid Dynamics*.

Shaw, J. A., Stokes, S & Lucking, M. A. 2003 The rapid and robust generation of efficient hybrid grids for RANS simulations over complete aircraft. *International Journal for Numerical Methods in Fluids* **43** (6-7), 785–821.

Shur, M. L., Spalart, P. R., Strelets, M. & Travin, A. K. 2015 An enhanced version of DES with rapid transition from RANS to LES in separated flows. *Flow, Turbulence and Combustion* **95** (4), 709–737.

Sirovich, L. 1987 Turbulence and the dynamics of coherent structures. I. Coherent structures. *Quarterly of Applied Mathematics* **45** (3), 561–571.

Slotnick, J., Khodadoust, A., Alonso, J., Darmofal, D., Gropp, W., Lurie, E. & Mavriplis, D. 2014 CFD vision 2030 study: A path to revolutionary computational aerosciences. *Tech. Rep.* NASA-CR–2014-218178. National Aeronautics and Space Administration.

Spalart, P. 2000 Trends in turbulence treatments. AIAA 2000–2306.

Spalart, P.R. 2014 Prediction of lift cells for stalling wings by lifting-line theory. *AIAA Journal* **52** (8), 1817–1821.

Spalart, P. R. 2001 Young-person's guide to detached-eddy simulation grids. *Tech. Rep.* CR-2001-211032. National Aeronautics and Space Administration.

Spalart, P. R 2009 Detached-eddy simulation. *Annual Review of Fluid Mechanics* **41**, 181–202.

Spalart, P. R. & Allmaras, S. R. 1992 A one-equation turbulence model for aerodynamic flows. AIAA 1992-0439.

Spalart, P. R., Deck, S., Shur, M. L., Squires, K. D., Strelets, M. & Travin, A. 2006 A new version of detached-eddy simulation, resistant to ambiguous grid densities. *Theoretical and Computational Fluid Dynamics* **20** (3), 181–195.

Spalart, P. R, Strelets, M. & Allmaras, S. R. 1997 Comments on the feasibility of LES for wings, and on a hybrid RANS/LES approach. In *Proceedings of first AFOSR international conference on DNS/LES*.

Steimle, P. C., Karhoff, D.-C. & Schröder, W. 2012 Unsteady transonic flow over a transport-type swept wing. *AIAA Journal* **50** (2), 399–415.

Stoica, P. & Moses, R. L. 2005 *Spectral Analysis of Signals*. Pearson Prentice Hall.

Stokes, G. G. 1845 On the theories of internal friction of fluids in motion. *Transactions of the Cambridge Philosophical Society* **8**, 287–305.

Strelets, M. 2001 Detached eddy simulation of massively separated flows. AIAA 2001-0879.

Sugioka, Y., Koike, S., Nakakita, K., Numata, D., Nonomura, T. & Asai, K. 2018 Experimental analysis of transonic buffet on a 3D swept wing using fast-response pressure-sensitive paint. *Experiments in Fluids* **59** (108), 1–20.

Taira, K., Brunton, S. L., Dawson, S. T. M., Rowley, C. W., Colonius, T., McKeon, B. J., Schmidt, O. T., Stanislav, S., Theofilis, V. & Ukeiley, L. S. 2017 Modal analysis of fluid flows: An overview. *AIAA Journal* **55** (12), 4013–4041.

Theofilis, V. 2011 Global linear instability. *Annual Review of Fluid Mechanics* **43** (1), 319–352.

Tijdeman, H. 1977 Investigations of the transonic flow around oscillating airfoils. PhD thesis, Faculty of Aerospace Engineering, Delft University of Technology.

Timme, S. 2020 Global instability of wing shock-buffet onset. *Journal of Fluid Mechanics* **885** (A37), 1–32.

Timme, S. & Thormann, R. 2016 Towards three-dimensional global stability analysis of transonic shock buffet. AIAA 2016-3848.

Touber, E. & Sandham, N. D. 2011 Low-order stochastic modelling of low-frequency motions in reflected shock-wave/boundary-layer interactions. *Journal of Fluid Mechanics* **671**, 417–465.

Travin, A., Shur, M., Strelets, M. & Spalart, P. R. 2000 Detached-eddy simulations past a circular cylinder. *Flow, Turbulence and Combustion* **63** (1), 293–313.

Travin, A., Shur, M., Strelets, M. & Spalart, P. R. 2002 Physical and numerical upgrades in the detached-eddy simulation of complex turbulent flows. In *Advances in LES of complex flows* (ed. R. Friedrich & W. Rodi), *Fluid mechanics and its applications*, vol. 65, pp. 239–254. Springer, Dordrecht.

Tu, J. H. & Rowley, C. W. 2012 An improved algorithm for balanced POD through an analytic treatment of impulse response tails. *Journal of Computational Physics* **231** (16), 5317–5333.

Tu, J. H., Rowley, C. W., Luchtenburg, D. M., Brunton, S. L. & Kutz, J. N. 2014 On dynamic mode decomposition: Theory and applications. *Journal of Computational Dynamics* **1** (2), 391–421.

Welch, P. 1967 The use of fast Fourier transform for the estimation of power spectra: A method based on time averaging over short, modified periodograms. *IEEE Transactions on Audio and Electroacoustics* **15** (2), 70–73.

Wilcox, D. C. 1993 *Turbulence modeling for CFD*. DCW Industries, Inc.

Xiao, Q., Tsai, H. & Liu, F. 2006 Numerical study of transonic buffet on a supercritical airfoil. *AIAA Journal* **44** (3), 620–628.

Zauner, M., De Tullio, N. & Sandham, N. D. 2019 Direct numerical simulations of transonic flow around an airfoil at moderate Reynolds numbers. *AIAA Journal* **57** (2), 597–607.

Appendix A

Modred Library

The modal decomposition performed herein uses the parallelised `modred` library developed by Belson *et al.* (2014). This `Python` library includes algorithms to perform proper orthogonal decomposition (POD) and dynamic mode decomposition (DMD), amongst others. Furthermore, there are two methods available for POD and DMD—the first is the so-called matrix approach and the second is the vector-space approach. The advantage of the first method is its relatively fast implementation and high computational efficiency owing to optimised matrix multiplication libraries. However, larger datasets may give rise to impractical matrix eigenvalue problems and become restrictive. This is where the second method becomes useful, since it is based solely on vector operations eliminating the need to store large matrices in memory. Instead, only two vectors are stored in memory simultaneously, while vector addition, scalar multiplication and inner products are parallelised. This vector-space approach is used consistently herein given the size of the datasets analysed. The following sections outline the implementation of POD and DMD using the vector-space approach as explained by Belson *et al.* (2014).

A.1 Proper Orthogonal Decomposition

The input dataset is a set of vectors $\{\mathbf{x}_i \in V\}$, where V is the vector space and $\mathbf{x}_i$ represents an input vector of dimension n at each instance in time (for $i = 1, \ldots, m$). For this dataset consisting of m snapshots each having n spatial points, where $m \ll n$, the POD procedure minimises the error of a projection $\mathbf{P}_r$ of rank r

$$\text{error} = \sum_{i=1}^{m} \|\mathbf{x}_i - \mathbf{P}_r \mathbf{x}_i\|^2 \tag{A.1}$$

where the operator $\|\cdot\|$ denotes the induced norm from the inner product $\langle \cdot, \cdot \rangle$ on V (linear in the second argument, conjugate linear in the first). This projection can now

be formulated as

$$\mathbf{P}_r \mathbf{x}_i = \sum_{j=1}^{r} \langle \boldsymbol{\varphi}_j, \mathbf{x}_i \rangle \boldsymbol{\varphi}_j \tag{A.2}$$

where the projection onto $\boldsymbol{\varphi}_j \in V$, which is the orthonormal basis of rank r (for $j = 1, \ldots, r$), minimises the error defined by Eq. (A.1). Each vector in this basis is a POD mode which is computed using the method of snapshots (Sirovich, 1987) as implemented in the following vector-space approach (Belson *et al.*, 2014).

First, the data snapshots are collected and stored as vectors, $\mathbf{x}_i \in V$ for $i = 1, \ldots, m$. The correlation matrix $\mathbf{H}$ of size $m \times m$ is formed by computing each inner product individually, using $[\mathbf{H}]_{i,j} = \langle \mathbf{x}_i, \mathbf{x}_j \rangle$. The following eigenvalue problem is then solved

$$\mathbf{H}\boldsymbol{\Psi} = \boldsymbol{\Psi}\boldsymbol{\Lambda} \tag{A.3}$$

where the eigenvectors contained in the orthogonal matrix $\boldsymbol{\Psi}$ are sorted in descending order, based on the corresponding eigenvalues λ_j stored in the diagonal matrix $\boldsymbol{\Lambda}$. In order to reduce computational effort, a particular number of modes to keep, r, can be selected, instead of computing all the modes, the number of which is equal to m. A truncated matrix $\mathbf{T}$ is computed based on this desired number of modes r using

$$\mathbf{T} = \boldsymbol{\Psi}_r \boldsymbol{\Lambda}_r^{-1/2} \tag{A.4}$$

where $\boldsymbol{\Psi}_r$ and $\boldsymbol{\Lambda}_r$ are submatrices of $\boldsymbol{\Psi}$ and $\boldsymbol{\Lambda}$, respectively. The modes $\boldsymbol{\varphi}_j$ are constructed individually, eliminating the need to store a large matrix containing all the modes, reducing computational effort, as follows

$$\boldsymbol{\varphi}_j = \sum_{i=1}^{m} \mathbf{x}_i [\mathbf{T}]_{i,j}. \tag{A.5}$$

A.2 Dynamic Mode Decomposition

The algorithm implemented in the `modred` library is based on a low-memory variant of the exact DMD algorithm (Tu & Rowley, 2012). The exact DMD variant is defined as the eigendecomposition of an approximating linear operator (Tu *et al.*, 2014) and generalises the standard method by Schmid (2010) to both sequential and non-sequential datasets. The vector-space approach developed in `modred` further reduces computational effort by removing redundant operations and is described next.

The data snapshots are collected and stored as vectors, $\mathbf{x}_i \in V$ for $i = 1, \ldots, m$. Each inner product of the correlation matrix $\mathbf{H}$ is computed individually, $[\mathbf{H}]_{i,j} = \langle \mathbf{x}_i, \mathbf{x}_j \rangle$, using all snapshots except the last one (i and j have a range of $1, \ldots, m-1$). The eigenvalues and eigenvectors of $\mathbf{H}$, $\boldsymbol{\Lambda}$ and $\boldsymbol{\Psi}$, respectively, are computed from Eq. (A.3) and sorted in descending order, as in the POD method. A sub-matrix $\mathbf{H}'$ is

defined as the previously computed correlation matrix with the first column removed

$$\mathbf{H}' = [\mathbf{H}]_{1:m-1,\ 2:m-1} \tag{A.6}$$

where $[\mathbf{H}]_{1:m-1,\ 2:m-1}$ denotes the elements in rows 1 to $m-1$ (both included) and columns 2 to $m-1$ of matrix $\mathbf{H}$. A column matrix $\mathbf{H}''$ is computed using $[\mathbf{H}]''_j = \langle \mathbf{x}_m, \mathbf{x}_j \rangle$ for $j = 1, \ldots, m-1$. A matrix $\mathbf{N}$ is now defined as

$$\mathbf{N} = \mathbf{\Lambda}^{-1/2} \mathbf{\Psi}^T \left[\mathbf{H}' \mathbf{H}'' \right] \mathbf{\Psi} \mathbf{\Lambda}^{-1/2}. \tag{A.7}$$

The following eigenvalue problem is solved

$$\mathbf{N}\mathbf{V} = \mathbf{V}\boldsymbol{M} \tag{A.8}$$

where $\mathbf{V}$ and $\boldsymbol{M}$ are the eigenvectors and eigenvalues of $\widetilde{\mathbf{A}}$, $\widetilde{\boldsymbol{A}} = \mathbf{\Psi}_r^T \mathbf{A} \mathbf{\Psi}_r$ and $\mathbf{A}$ is defined in Eq. (2.18). The diagonal entries of $\boldsymbol{M}$ are the DMD eigenvalues μ_j. A coefficients matrix $\mathbf{T}$ is then defined as

$$\mathbf{T} = \mathbf{\Psi} \mathbf{\Lambda}^{-1/2} \mathbf{V} \mathbf{D} \tag{A.9}$$

where $\mathbf{D}$ is a diagonal matrix with diagonal $\mathbf{d}$

$$\mathbf{d} = \left(\mathbf{V}^T \mathbf{V} \right)^{-1} \mathbf{V}^T \mathbf{\Lambda}^{-1/2} \mathbf{\Psi}^T \left[\mathbf{H} \right]_{1:m-1,\ 1}. \tag{A.10}$$

The DMD modes are constructed individually as

$$\boldsymbol{\varphi}_j = \sum_{i=1}^{m} \mathbf{x}_i [\mathbf{T}]_{i,j}. \tag{A.11}$$

Appendix B

Tensor Notation

Tensor notation (also called index, indicial or Einstein notation) is often used in the field of turbulence modelling as it allows compact and clear notation when the governing equation are written in differential form (Blazek, 2015). First-order tensors have three components and thus correspond to vectors. For instance, Cartesian coordinates in three-dimensional space can be represented by x_i, where

$$x_i = [x_1, x_2, x_3] = [x, y, z] = \mathbf{r}. \tag{B.1}$$

Second-order tensors have nine components and represent 3×3 matrices, for example

$$v_i v_j = \begin{bmatrix} v_1 v_1 & v_1 v_2 & v_1 v_3 \\ v_2 v_1 & v_2 v_2 & v_2 v_3 \\ v_3 v_1 & v_3 v_2 & v_3 v_3 \end{bmatrix}. \tag{B.2}$$

The Kronecker delta δ_{ij} is a function of two variables and constitutes a special second-order tensor corresponding to a 3×3 identity matrix. The function is one in the case of equal variables and zero otherwise

$$\delta_{ij} = \begin{cases} 1 & \text{if } i = j, \\ 0 & \text{if } i \neq j. \end{cases} \tag{B.3}$$

Tensor notation uses the Einstein summation convention which implies a summation over all three coordinate directions when two identical indices occur in an expression. For example, the dot product between two vectors $\boldsymbol{u}$ and $\boldsymbol{v}$ is written as

$$u_i v_i = u_1 v_1 + u_2 v_2 + u_3 v_3 = \boldsymbol{u} \cdot \boldsymbol{v}. \tag{B.4}$$

In a similar manner, the divergence of a vector $\boldsymbol{v}$ is

$$\frac{\partial v_i}{\partial x_i} = \frac{\partial v_1}{\partial x_1} + \frac{\partial v_2}{\partial x_2} + \frac{\partial v_3}{\partial x_3} = \nabla \boldsymbol{v}. \tag{B.5}$$

Appendix C

DLR-TAU Low-Dissipation and Low-Dispersion Schemes

This appendix describes the development of the recent second-order low-dissipation low-dispersion scheme in DLR-TAU. First, a low-dissipation (LD) scheme was developed for scale-resolving simulations using TAU (Probst & Reuß, 2015). Second, the LD scheme was enhanced by the low-dispersion scheme described by Löwe *et al.* (2016) to develop a low-dissipation low-dispersion (LD2) scheme. Third, attaching and reattaching flows on complex geometries motivated a hybrid scheme which blends between LD2 parameters and those from a standard central scheme (the reference scheme), denoted as the hybrid LD2 scheme (Probst *et al.*, 2016).

The low-dissipation (LD) scheme in TAU uses the central discretisation of the skew-symmetric compressible convection operator by Kok (2009). This is considered as nondissipative since it preserves kinetic energy both locally and globally. Considering a general convected variable φ, this operator is defined in differential form as

$$K_\varphi = \frac{1}{2}\frac{\partial \rho\varphi}{\partial t} + \frac{1}{2}\rho\frac{\partial \varphi}{\partial t} + \frac{1}{2}\nabla\cdot(\rho\boldsymbol{u}\varphi) + \frac{1}{2}\rho\boldsymbol{u}\cdot\nabla\varphi \tag{C.1}$$

where $\boldsymbol{u}$ represents the velocity vector. The operator in Eq. (C.1) can be discretised with a particular compressible flux formulation ensuring local and global conservation of both φ and φ^2 (Kok, 2009; Probst *et al.*, 2016). Details on the fluxes are provided later together with the outline of the LD2 scheme. Furthermore, a fourth-order artificial dissipation can be added to the five mean-flow equations (mass, momentum and total energy) to ensure numerical stability on hybrid grids. Considering two adjoining control volumes i and j, the dissipative flux at the face ij between the cells is given by

$$\boldsymbol{D}_{ij}^{(4)} = \kappa^{(4)}\cdot|\boldsymbol{A}|_{ij}\cdot\Phi_{ij}\cdot\{\nabla^2\boldsymbol{w}_i - \nabla^2\boldsymbol{w}_j\}. \tag{C.2}$$

The term $\kappa^{(4)}$ is a global scaling factor that controls the amount of artificial dissipation and is typically referred to as the inverse fourth-order coefficient in TAU. The term $|\boldsymbol{A}|_{ij}$ is the matrix-dissipation operator where $\boldsymbol{A}$ is the inviscid flux Jacobian ($\boldsymbol{A} = \partial \boldsymbol{f}/\partial \boldsymbol{w}$), $\boldsymbol{f}$ represents the flux vector whilst $\boldsymbol{w}$ is the vector of conservative mean flow variables. The term Φ_{ij} is a cell-stretching coefficient that increases dissipation in the direction of local cell stretching to stabilise computation on high-aspect ratio cells. Although the skew-symmetric discretisation theoretically allows simulations without any artificial dissipation, $\boldsymbol{D}_{ij}^{(4)} = 0$, numerical stability can only be proven for incompressible flow (Kok, 2009) and some amount of dissipation is typically added in the general application of DLR-TAU. Various values for the terms in Eq. (C.2) were studied by Probst & Reuß (2015) who obtained virtually the same mean-flow accuracy from LES when comparing nondissipative schemes with low-dissipation schemes having very low levels of artificial dissipation. Probst *et al.* (2016) note that the LD scheme with $\boldsymbol{D}_{ij}^{(4)} \neq 0$ presents a shift from strict energy conservation.

This low-dissipation scheme was enhanced by Löwe *et al.* (2016) who modified the computation of the skew-symmetric compressible fluxes at each cell face ij. The face-based method based on Gauss's theorem of divergence and gradient operators in the LD scheme is limited to a three-point stencil. This is extended to a five-point stencil by also using gradients when computing face values. The following family of gradient operators for a cell i with parameter α is obtained

$$\nabla_\alpha \varphi_i = \frac{1}{V_i} \sum_j \varphi_{ij,\alpha} \boldsymbol{n}_{ij} \tag{C.3}$$

where V_i is a control volume, $\boldsymbol{n}_{ij}$ represents the area-weighted face normal between cells i and j whilst $\varphi_{ij,\alpha}$ are the face values. Rather than taking the left L and right R values for the adjacent cells i and j, an extrapolation rule is added,

$$\varphi_{L,ij} = \varphi_i + \alpha \cdot \nabla_0 \varphi_i \cdot \boldsymbol{d}_{ij} \quad \text{and} \quad \varphi_{R,ij} = \varphi_j - \alpha \cdot \nabla_0 \varphi_j \cdot \boldsymbol{d}_{ij} \tag{C.4}$$

where $\boldsymbol{d}_{ij} = x_j - x_i$ is the distance between the centres of the two control volumes whilst $\nabla_0 \varphi_i$ and $\nabla_0 \varphi_j$ are the Green-Gauss gradients of φ in the control volumes i and j, respectively. The centrally reconstructed value of the general variable φ is now defined as,

$$\varphi_{ij,\alpha} = \frac{1}{2}(\varphi_i + \varphi_j) + \frac{1}{2}\alpha (\nabla_0 \varphi_i - \nabla_0 \varphi_j) \cdot \boldsymbol{d}_{ij} \tag{C.5}$$

The standard gradients with central averages often found in finite volume codes are obtained when $\alpha = 0$ in Eq. (C.5). As an illustration for the implementation of this scheme in an unstructured finite volume context, consider the Euler equations for a

control volume V_i as discretised by Kok (2009)

$$\frac{\mathrm{d}\rho_i}{\mathrm{d}t} + \nabla_i \cdot (\overline{\rho \boldsymbol{u}}) = 0 \qquad \text{(continuity equation)} \tag{C.6}$$

$$\frac{\mathrm{d}\rho_i \boldsymbol{u}_i}{\mathrm{d}t} + \nabla_i \cdot \left(\overline{\rho \boldsymbol{u}} * \bar{\boldsymbol{u}} + \nabla_i \bar{P} I\right) = 0 \qquad \text{(momentum equation)} \tag{C.7}$$

$$\frac{\mathrm{d}\rho_i E_i}{\mathrm{d}t} + \nabla_i \cdot \left(\overline{\rho \boldsymbol{u}} \cdot \tilde{E} + \widetilde{\boldsymbol{u} P}\right) = 0 \qquad \text{(total energy equation)} \tag{C.8}$$

where P is the static pressure and the operators $\bar{}$ and $\tilde{}$ define specific averages in the discrete gradient operator ∇_i as defined by Kok (2009). The convective fluxes for an energy-preserving second-order central scheme devised by Löwe *et al.* (2016) and obtained using the formulations and averaging rules defined in Kok (2009) are

$$(\overline{\rho \boldsymbol{u}})_{ij} = \frac{1}{2}\left(\rho_L \cdot \boldsymbol{u}_L + \rho_R \cdot \boldsymbol{u}_R\right) \tag{C.9}$$

$$\left(\overline{\rho \boldsymbol{u}} * \bar{\boldsymbol{u}} + \bar{P} I\right)_{ij} = \frac{1}{2}\left(\boldsymbol{u}_L + \boldsymbol{u}_R\right) * \frac{1}{2}\left(\rho_L \cdot \boldsymbol{u}_L + \rho_R \cdot \boldsymbol{u}_R\right) + \frac{1}{2}\left(P_L + P_R\right) I \tag{C.10}$$

$$\begin{aligned}\left(\overline{\rho \boldsymbol{u}} \cdot \tilde{E} + \widetilde{\boldsymbol{u} P}\right)_{ij} = {} & \frac{1}{2}\left(\rho_L \cdot \boldsymbol{u}_L + \rho_R \cdot \boldsymbol{u}_R\right) \cdot \left[\frac{1}{2}\left(\boldsymbol{u}_L + \boldsymbol{u}_R\right) + \frac{c_L \cdot c_R}{\gamma(\gamma - 1)}\right] \\ & + \frac{1}{2}\left(\boldsymbol{u}_L \cdot P_L + \boldsymbol{u}_R \cdot P_R\right)\end{aligned} \tag{C.11}$$

where c is the speed of sound, γ is the ratio of specific heats, and the subscripts L and R denote the left (cell neighbour i) and right (cell neighbour j) values at the face ij. The values of the velocity vector $\boldsymbol{u}$ and the pressure P are extrapolated in the low-dispersion scheme by following Eq. (C.4)

$$\boldsymbol{u}_L = \boldsymbol{u}_i + \alpha_u \cdot \nabla_0 \boldsymbol{u}_i \cdot \boldsymbol{d}_{ij} \quad \text{and} \quad P_L = P_i + \alpha_p \cdot \nabla_0 P_i \cdot \boldsymbol{d}_{ij} \tag{C.12}$$

$$\boldsymbol{u}_R = \boldsymbol{u}_j - \alpha_u \cdot \nabla_0 \boldsymbol{u}_j \cdot \boldsymbol{d}_{ij} \quad \text{and} \quad P_R = P_j - \alpha_P \cdot \nabla_0 P_j \cdot \boldsymbol{d}_{ij}. \tag{C.13}$$

In the standard LD2 scheme in DLR-TAU, only values for the velocities and pressure are extrapolated, after the error analysis conducted by Löwe *et al.* (2016) on a vortex-convection problem. The face values for density and speed of sound are computed using the standard formulation, $\alpha_\rho = \alpha_c = 0$.

Numerical stability when using the LD2 scheme might not be guaranteed on grids of more complex geometries that follow industrial best practice. Therefore, Probst *et al.* (2016) introduced a hybrid LD2 scheme that employs a numerical blending scheme between the numerical parameters of the LD2 scheme, Ψ_{LD2}, and those from a more conservative (more dissipative and dispersive) reference scheme, Ψ_{ref}. All numerical parameters are locally weighted via an empirical blending function σ following the work of Travin *et al.* (2002)

$$\Psi = (1 - \sigma) \cdot \Psi_{\mathrm{LD2}} + \sigma \cdot \Psi_{\mathrm{ref}}. \tag{C.14}$$

$$\sigma = \tanh\left(\max\left\{\left[\frac{C_{\mathrm{DES}}\Delta}{l_{\mathrm{turb}} \cdot g} - 0.5\right], 0\right\}^3\right) \tag{C.15}$$

where C_{DES} and Δ are taken directly from the DES model from Eq. (5.21), l_{turb} is a modified turbulence length scale and g is an empirical parameter defined as

$$l_{\mathrm{turb}} = \frac{\nu_t + \nu_l}{\sqrt{C_\mu^{3/2} K}} \tag{C.16}$$

$$g = \tanh\left(\frac{0.5\Omega \max(S, \Omega)}{\max\left[0.5(S^2 + \Omega^2), 10^{-20}\right]}\right) \tag{C.17}$$

where C_μ is a model constant, S denotes the magnitude of mean strain, Ω represents vorticity, and $K = \max\left\{\left[0.5(S^2 + \Omega^2)\right]^{1/2}, 0.1\tau^{-1}\right\}$, where τ is the characteristic convective time. The aim of the blending function defined in Eq. (C.15) is to detect LES regions where σ is close to zero, and coarser grid regions treated with the more standard numerics defined in the reference scheme. The empirical parameter g in Eq. (C.17) is introduced to ascertain that σ is close to one in the coarser and less disturbed grid regions, ensuring numerical stability (Travin *et al.*, 2002).